Ulrike Festel, BSc.

The electronic structure of picene on single crystal silver and copper surfaces

Master's Thesis

to achieve the university degree of

Dipl.-Ing.

Master's degree programme: Technical Physics

submitted to

Graz University of Technology

Supervisor

Assoz. Prof. Mag. Dr.rer.nat. Georg Koller

Surface Science Group, Institute of Physics
Head: Univ.-Prof. Dipl.-Ing. Dr.techn Martin Sterrer

Graz, April 2020

This document is set in Palatino, compiled with pdfLaTeX2e and Biber.

The LaTeX template from Karl Voit is based on KOMA script and can be found online: https://github.com/novoid/LaTeX-KOMA-template

Affidavit

I declare that I have authored this thesis independently, that I have not used other than the declared sources/resources, and that I have explicitly indicated all material which has been quoted either literally or by content from the sources used. The text document uploaded to TUGRAZonline is identical to the present master‘s thesis.

06.04.2020

Date

Signature

Acknowledgement

I would first like to thank my thesis advisor Assoz. Prof. Georg Koller of the Surface Science Group at the Institute of Physics at the University of Graz. The door of Prof. Koller was always open whenever I ran into a trouble shot or had a question about my research or writing. In my impatient times he reminded me that science is not about rushing to a solution, but more an ongoing process needing time for rethinking. He allowed this paper to be my own work, but steered me in the right direction whenever I needed it.

A big thank to MSc. Larissa Egger, who gave me the skills to be able to perform my experiments on the Scienta and had the faith in me to let me doing it. She was always there when I need help or encouragement.

I also want to mention Ms. Gaar from the secretariat of the KF University's Physics Institute and Ms. Pichler of the deanery of Physics at the TU, who had always an open ear and patiently helped me whenever I had requests.

Finally I have to express my deep thanks to my parents and my partner, who never let me down in the times of my studies and stood beside me in the process of writing this thesis.

Ulrike Festel

Abstract

Picene as a promising isomer of pentacene due to its outstanding features like high electronic mobility and if doped with alkali metals it even exhibits superconductivity. Here, it is investigated on the four different fcc metal single crystals Ag(100), Ag(110), Cu(110), Cu-p(2x1)O with UPS and XPS under UHV conditions to get information about the electronic as well as geometric structure. For a multilayer on Ag(110) as well as a mono on Ag(100) the position of the molecular orbitals could be determined and a Stranski-Krastanov growth was established. Comparing picene on the clean and oxygen modified Cu(110) surfaces, not only differences in the electronic level alignment but also in the growth geometry were observed, with the Cu-(2x1)O reconstructed surface suggesting a tilted alignment in the monolayer, compared to the planar adsorption geometry assumed for the metal surfaces.
To unambiguously compare the photoelectron emission intensities for the various take-off angles, a calibration of the Sienta SES 200 analyzer system was attempted with a graphite paste as sample. This revealed not only the peculiar situation of the angel dependent intensity distribution, but also localized non dispersive electronic states in graphite.

Contents

1. Introduction

The aim of this thesis is the investigation of the electronic beside the geometric structure of the organic molecule Picene on the four metal substrates Ag(110), Ag(100), Cu(110) and Cu-p(2x1)O. A second goal is to find an angular calibration routine for the Scienta SES 200 analyser, by using a completely disordered, and thus homogeneous graphite powder thin film sample. In the course of the working process also a manual for the "every day use" of the electron energy analyser and its UHV-chamber evolved.

Plastic is cheap, durable, lightweight versatile and since the 1970s we know it offers electronic conductivity as additional feature (Kaner and MacDiarmid, 1988). Therefore, organic electronics and optoelectronic devices compete with the classic inorganic semiconductor technology.

Angle resolved photoemission spectroscopy (ARPES) is a mature surface science method that yields the valence band electronic structure of surfaces and adsorbates. The angular distribution pattern of the photoemitted electrons obtained from ARPES of oriented multilayer films and chemisorbed monolayers of conjugated molecules can be simply related to their molecular orbital structure.
In addition to measuring the electronic structure, this allows a determination whether a molecule is oriented or not. An oriented monolayer and thick film is an important requirement for charge transfer as well as light emission/absorption properties.
Furthermore the band alignment in general concerning the molecular orbital position and the Fermi-level of the metal substrate can be revealed. A charge transfer through the heterogenic metal-molecular-interface is visualised by a filling of the LUMO.

1. Introduction

Picene is the organic molecule chosen for this work. Picene has a high electronic mobility, and it even becomes superconductive if doped with potassium (Liu et al., 2014). Furthermore it is quite stable against oxidation. Chemically picene is an isomer of pentacene, a common organic semiconductor. However, electronically it is quite different similar to previously studied rod-like molecules such as n-phenyls and acenes, but different in its overall shape, which is more plate-like. Moreover it can be seen as a graphene flake.

The selected substrates for growing Picene are the single crystal surfaces of Ag(110), Ag(100), Cu(110) and p(2x1) oxygen reconstructed Cu(110).
These surfaces are all strongly anisotropic, which often makes a preferred molecular alignment more likely.
Cu(110) belongs to the same main group as Ag(110), but has a significantly different lattice-constant. The p(2x1) oxygen-reconstruction of Cu(110) tunes the interaction strength and the work-function. Literatur exists for Picene on Ag(110) as well as Ag(100), which makes our results comparable.

In a second task angular calibration measurements of the Scienta SES 200 electron energy analyser have been performed. The aim is here to derive the angular dependency of the photoelectron intensity variation due to due to the change of light incidence during the movement of the crystal in the polar plane. As a sample a homogeneous graphite powder paste has been used, which is emitting photoelectrons isotropically in all directions, carried out for HeI, HeII, XPS. The measurements are carried out in angular as well as spatial mode for the Sienta SES 200 analyser

2. Methods - Photoelectron spectroscopy (PES)

data Photoemission spectroscopy (PES) roots on Einstein's photoelectric effect (Fig. 2.1) and the relation for the energy conservation (eq. 2.1). It allows a direct probing of the density of states of the surface. Therefore it is an accepted method to study the band structure of solids by detecting the photoemitted electron's kinetic energy with respect to its angular distribution (Puschnig et al., 2013).

$$h\nu = E_b + \phi + E_{kin} \tag{2.1}$$

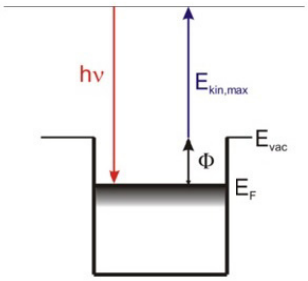

Figure 2.1.: Visualization of the photo effect in terms of energy conservation.

The incident photon excites a so called photo electron which passes into the vacuum. An electrostatic analyser records its kinetic energy together with its emission angle. The work function appearing in fig. 2.1 is the work function of the detector. Independent of the investigated sample, the Fermi-edge will always appear at the same value in our measurements, because the detector and the sample are connected and grounded.

By using different photon sources different electronic levels in the solid can be probed. 21.21eV (HeIα) or 40.81 eV (HeIIα) (Elander, 1984) addresses the electronic levels inside the valence orbitals, whereas a light quantum from a X-ray source probes the core levels of the surface atoms (Henzler, Göpel, and Ziegler, 1994).

2.1. UV Photo Emission Spectroscopy and Angle Resolved UV Photo Electron Spectroscopy

The Ultraviolet Photo Emission Spectroscopy (UPS) is the most direct measurement method to image the frontier orbitals of a metal or even from conjugates organic molecules which inherit the electronic, optical and chemical properties of the material (Offenbacher et al., 2016).

This method enables an investigation of technical relevant substrate-molecule systems, even at room temperature (Koller, Puschnig, et al., 2016). Its high surface sensitivity arises from the small mean free path length of the produced photoelectrons in the order of a few Å (Hüfner, 2003).

The probing of the DOS by the light of a He-discharge lamp (UV) directly produces the corresponding UPS spectrum, also called energy dispersion curve (EDC), like in fig. 2.2.

2.1. UV Photo Emission Spectroscopy and Angle Resolved UV Photo Electron Spectroscopy

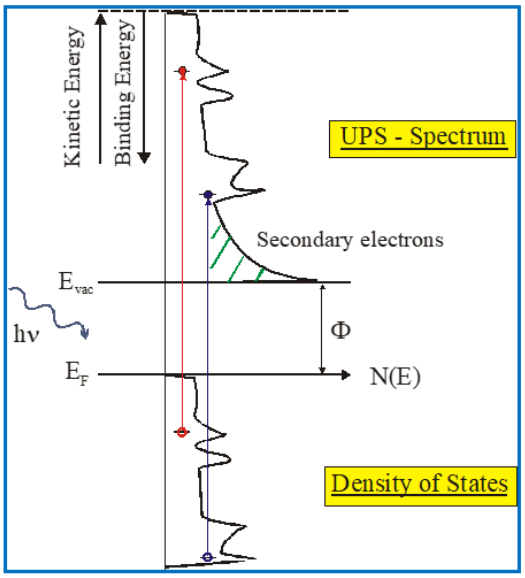

Figure 2.2.: The Density of states, and hence the orbitals the electrons are emerging from are directly mapped as peaks in the UPS spectrum. This graphic contains 2 photons with their excitation.

The peak positions correspond with the orbital binding energies, which is important for the band alignment. The height of the peaks, their intensity, reveal the molecular orientation and the band structure. The suppression of the substrate features is a function of coverage and therefore telling something about the growth mode. Finally the secondary electron cutoff is important for the work function Φ calculation.

To each EDC (fig. 2.3a) an image (fig. 2.3b) exists. The later one is used to select the areas of high intensity and cut out a big amount of the background before the data processing in the EDC starts.

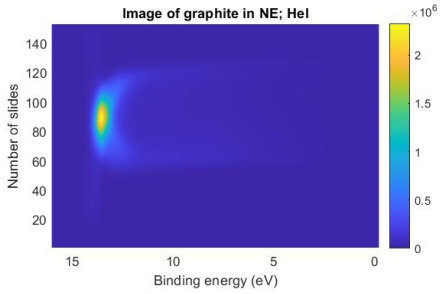

(a) HeI image of graphite. The maximum intensity has 2325224 counts and is located on the x-axis at $E_b = 13.6$ eV and at slide 88 at the y-axis.

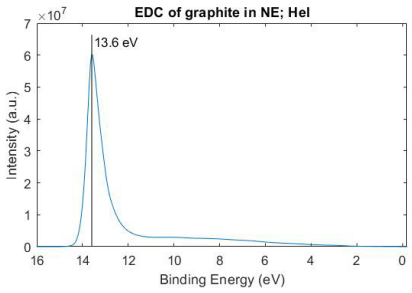

(b) To the image related EDC spectrum of graphite.Teh intensity maximum is clearly the secondary electron peak at $E_b = 13.6$ eV.

Figure 2.3.: The two possible imaging methods of an HeI photoemission experiment carried out on a Graphite sample in NE ($\theta = 254°$) and angular mode with pass energy 10 eV and energy range $E_{kin} = 0 - 20$ eV.

The information for the images and EDCs is derived by the mechanism of the photo effect, the energy conservation of the process as well as the unaltered $k_{||}$ - component of the wave vector of the excited electron.

The $k_{||}$ component of the exited electron inside the metal and in the vacuum is the same and therefore allows to address its direction via the polar (ϕ) together with the azimuth angle (θ) like shown in fig. 2.4a and fig. 2.4b. This enables a 2 dimensional image of the surface band structure since the 1970s.

2.1. UV Photo Emission Spectroscopy and Angle Resolved UV Photo Electron Spectroscopy

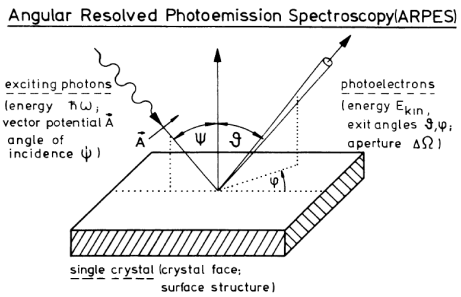

(a) Path of rays in an ARUPS experiment, with the polar ϕ and the azimuthal direction of the emitted electron.

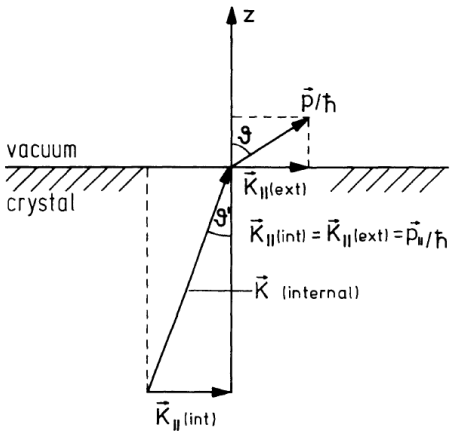

(b) A more distinct description of the transition of the photo electron from the sample into the vacuum based on the conservation of $k_{||}$ beside the energy with the momentum $\vec{p} = \hbar \cdot \vec{K}$.

Figure 2.4.: Sketches of the photoemission process taken from (Hüfner, 2003).

$$k_{||} = |\vec{K}| \cdot sin(\theta) \ [\mathring{A}^{-1}]$$
$$k_{||} = \sqrt{\frac{2 \cdot m \cdot E_{king}}{\hbar^2}} \cdot \sin\theta \tag{2.2}$$

$k_{||}$ in eq.2.2 can be further separated in its 3 room directions, where the x- and y- components are the important ones for the momentum maps. The mentioned k_z-part is not conserved.

$$k_x = k_{||} \cdot cos(\phi) \tag{2.3}$$
$$k_y = k_{||} \cdot sin(\phi) \tag{2.4}$$
$$k_z = k_{||} \cdot cos(\theta) \tag{2.5}$$

To gain a 3 dimensional image, even from molecules and adsorbates on the surface, the angle resolved photo emission spectroscopy ARUPS experienced an evolution into the photo emission tomography. A new theoretical approach utilizes the angular distribution of the photo current which allows to reconstruct even 3 dimensional orbitals in real space (Puschnig et al., 2013).

Depending on how many different angular adjustments and photon energies are applied, the ARUPS outcome can be a spectrum, a band map or a momentum map like shown in fig. 2.5 . This thesis only contains spectra and the theoretically with DFT calculated momentum maps of picene.

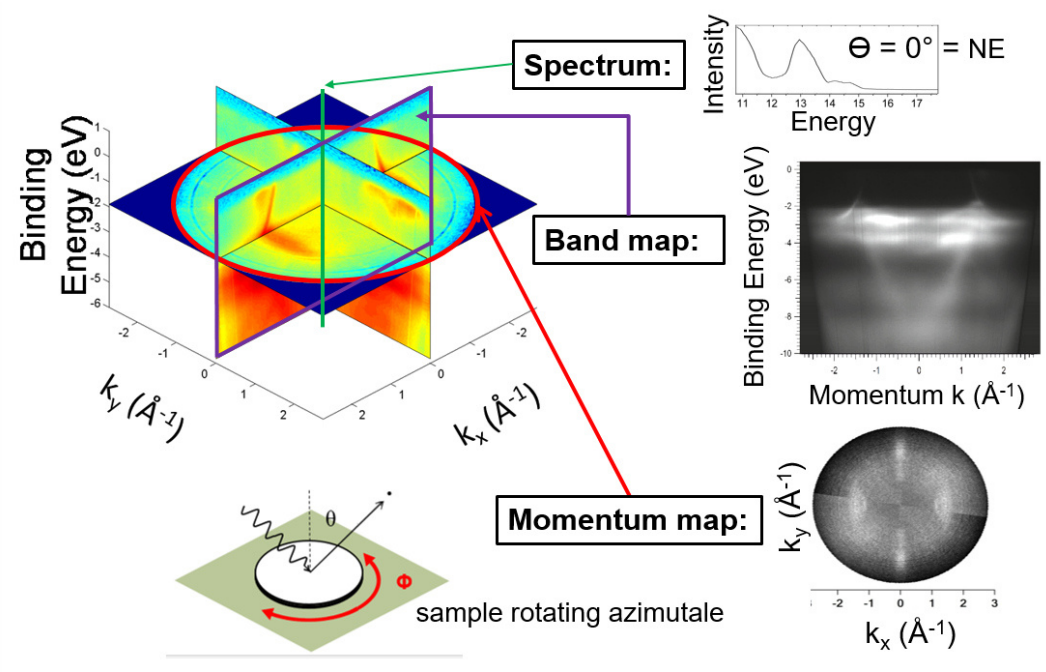

Figure 2.5.: The different outputs of an ARUPS experiment as a spectrum, a band map or a momentum map.

The theory that validates the experimental method is the so called one-step-model which roots on a single coherent sequence for the photo electron from the wave function of the binding orbital Ψ_i to the wave function of the final state Ψ_f in the vacuum (Puschnig et al., 2013).

The sum of all those transitions is expressed in the photo current I (eq. 2.6) for which Fermi's golden rule holds. It's parameterized not only by the E_{kin} of the detected electrons, but also by their polar and anzimuthal angles ϕ and θ.

$$I(\theta, \phi; E_{kin}) \propto \sum_i |\left\langle \Psi_f(\theta, \phi; E_{kin}) \right| \mathbf{A} \cdot \mathbf{p} \left| \Psi_i \right\rangle|^2 \times \sigma(E_i + \phi + E_{kin} - h\omega) \quad (2.6)$$

In this dipole approximation $\mathbf{A}$ is the vector potential of the exciting electromagnetic light wave. $\mathbf{p}$ is extracted from the measured $\mathbf{K}$ following the De-Broglie-relation $\mathbf{p} = \hbar\,\mathbf{k}$, visualized in fig. 2.4b .

This whole systematic can be rewritten in a plane-wave approximation (Koller, Puschnig, et al., 2016):

$$W_{i->f} \sim |\left\langle \Psi_i \right| \hat{H}_{int} \left| \Psi_f \right\rangle|^2 \delta(h\nu - E_b - E_f - \Phi) \quad (2.7)$$

The δ-function ensures the energy conservation of the whole process. This time the perturbation operator with $\hat{H}_{int} \approx \mathbf{E} \cdot \nabla$ contains the interaction with the exciting electronic field vector of the light $\mathbf{E}$ with the impulse operator of the electron $\hat{p} = -i\hbar\nabla$.

It turned out to be possible to describe the initial state as a one-electron wave function, resembling an orbital in quantum theory. A plane wave characterizes the finals state. Both are joined by a Fourier transformation, sharing the same wave vector:

$$W_{i->f} \sim |\Psi_i(k_x, k_y, k_z)|^2 \quad (2.8)$$

Now it is possible to see the final wave function as projection of the initial state, the electron orbital expressed in eq.2.8.
The due to the measurement lost phase can be imprinted by an iteration process. As a result the momentum maps and the three dimensional shaped simulations of the molecule orbitals are possible like for the HOMO of Picene in fig. 3.8a. The LUMO which is empty can be seen too due to charge

transfer from the metal to the molecule.

For charge transfer the alignment of the substrates work function and the band of the molecule are crucial for charge transfer. Koller, Blyth, et al., 2000 revealed that a measurement of the work function is enough to determine such a situation as the ionization potential of the film stays constant.

Fig. 2.6 by Hüfner, 2003 serves to illustrate the connections of the physical quantities in the following discussion. As already mentioned the UPS spectrum is a direct image of the valence electron orbitals of a metal, like for Cu(110) in fig.2.6 or an organic molecule.

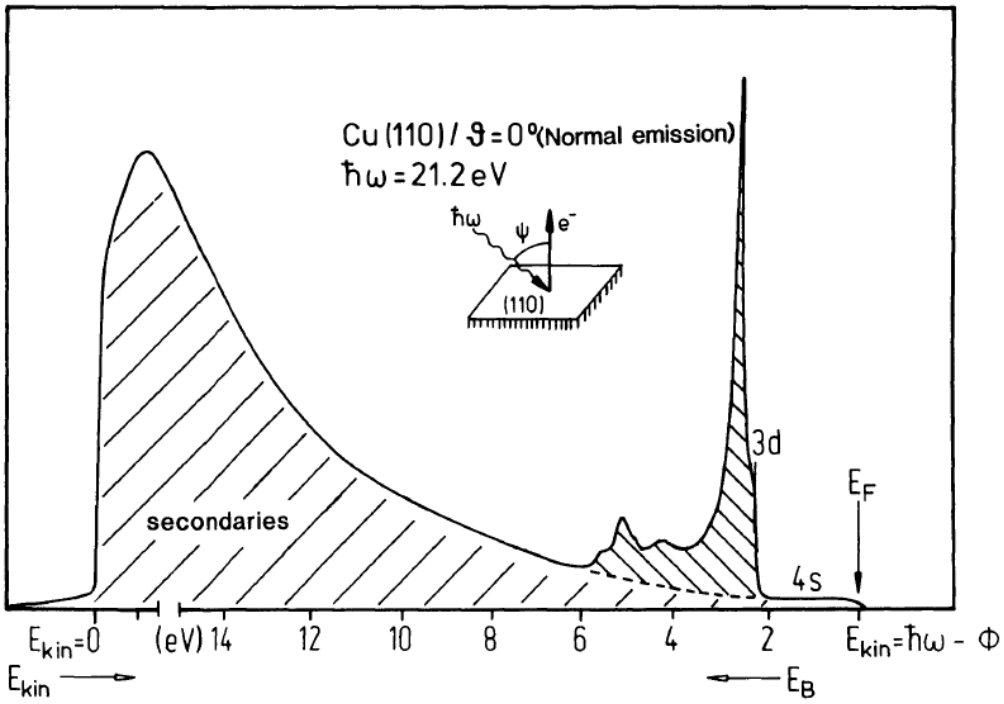

Figure 2.6.: UPS spectra of Cu(110) in normal emission showing the secondary electron cutoff, the Fermi energy, the two energy scales as well as the features of the metal band.

The energy difference between the Fermi level E_F and the minimum energy of the secondary electron cutoff E_c illustrated in fig. 2.6 gives the spectral width. Subtracting it from the energy of the incident photons gives the work function ϕ.

$$\Phi = h\nu - (E_F - E_c) \tag{2.9}$$

Otero, Vázquez de Parga, and Gallego, 2017 describe the change of the work function due to the deposition of a molecule. The work function value is specific for each metal face and consists of a contribution of the bulk chemical potential and an electrostatic potential across the interface. On the surface the positive charge density goes to zero whereas the electrons spill-out into the vacuum, producing a surface dipole. Due to the deposition of a molecule the electrons rearrange and the spill-out is suppressed, the so called 'pillow'- or 'push back'-effect. This affects the value of the work function. Usually it is lowered with increasing thickness of the molecule sheet, till one monolayer is filled. This is the onset where the value in general stays constant regardless how high the multi layer grows. This effect happens in all systems. If charge transfer happens, the interface dipole change again and the work function shifts to a higher value.
The graphic 2.7 exemplifies the case of a molecule on a metal surface, omitting the interface dipole. On the left side the LUMO is energetically higher than the Fermi-edge of the metal, no charge transfer is possible. On the right side it is the opposite situation resulting in a filling of the LUMO. More detailed information provides Otero, Vázquez de Parga, and Gallego, 2017.

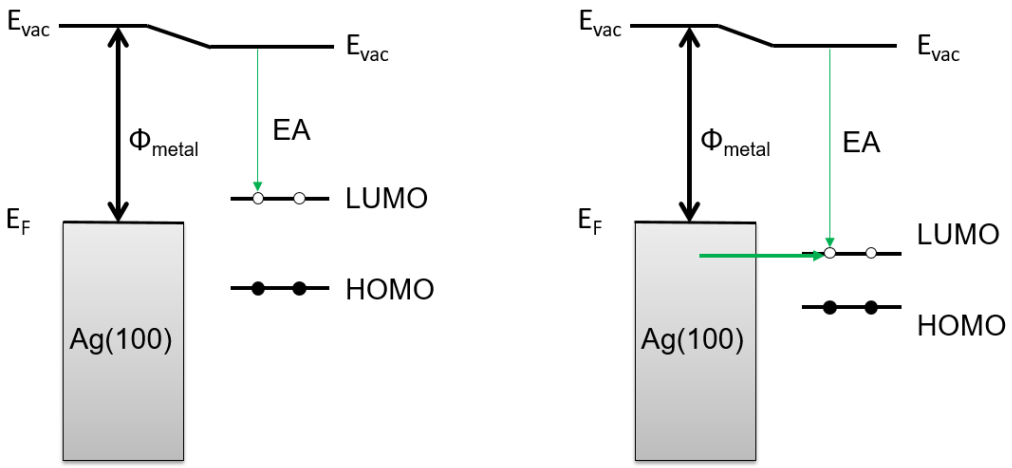

Figure 2.7.: On the right side a charge transfer is possible due to the fact, that the LUMO is energetically lower than the Fermi-edge of the metal. On the left side the situation is the other way round and no LUMO filling can occur. The vacuum level rearranges due to the assumed Fermi-pinning.

At the experimental setup in Graz, independent of the metal, the Fermi-edge always remains at the same value, the vacuum energy level changes. This is accomplished by connecting the detector and the sample beside grounding both.

From the molecular data base of Puschnig (Puschnig, P. *Molecular data Base*, http://143.50.77.12:5000/) his group calculated the DOS shown in fig.2.8 for a picene molecule in gas phase. Based on this the shapes of the molecules frontier orbitals as k-maps along with their shapes in real space are simulated, to be seen in sec. 3 figures 3.7a to 3.9b.

2.2. XPS

The XPS method works analogue to the UPS, only the energies of the photons is higher (Mg k_α: 1253,6 eV and Al k_α: 1486,6 eV), and core level electrons can be excited. This allows a conclusion of the chemical elements

on the sample. Here we have applied XPS to determine the cleanliness of the substrate prior to deposition and to estimate the molecular coverage in sec. 4.

2.3. Data processing

The predominant applied method in this work rests on comparing the binding energies of the peaks in the EDC spectra with the positions of the LUMOs and HOMOs in the DOS (fig. 2.8) of a gas phase Picene molecule calculated from DFT, accomplished by the group of Pushnig.

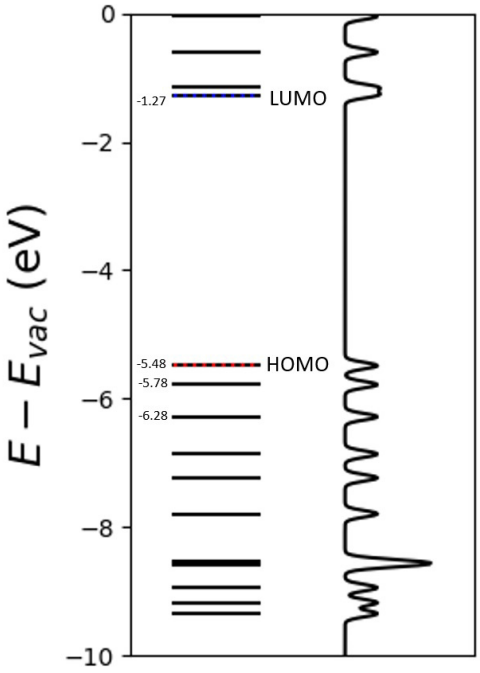

Figure 2.8.: DFT based DOS calculations for the frontier orbitals of a picene molecule in gas phase by the Group Peter Pushnig (page 12)

The binding energy of the molecule orbitals and their distances in the DOS are a starting point to adjust with the peaks found in the UPS spectra. The

work function in eq. 2.10 ensures the adjustment to the adsorbed situation. The NIST homepage (Standards and Technology, n.d.) provides the values for the ionization potential and electron affinity of the molecule, in this case Picene with $I_p = 7.51$ eV, $EA = 0,54$eV. Emperically often an additional shift of 1.25 eV was observed (ref.: G. Koller private communications), which is included as last term in 2.10 .

$$HOMO = I_p - \phi - 1.25 \tag{2.10}$$

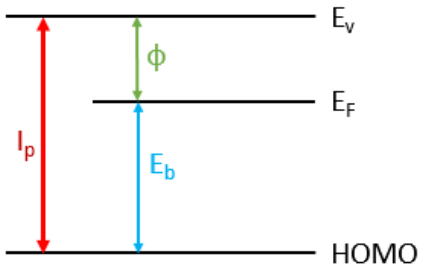

Figure 2.9.: Schematic representation of eq. 2.10 for the HOMO. The kinetic energy is measured in the vacuum state E_V.

3. General overview of Picene and the substrates used

The metallic substrates Ag(110), Ag(100), Cu(110) as well as Cu-p(2x1)O serve as template for the growth of Picene for layer thicknesses ranging between (sub)monolayers up to several tens of layers. In the following the electronic and geometric structure of the substrates and picene is given. The relevant literature is summarized.

3.1. The Substrates

Both, Silver and copper, have fcc lattices and belong to the same main group (11), but differ in their lattice parameters. For Cu(110) the oxygen reconstruction doubles the periodicity in the [1-10]-direction and also reduces the interaction strength with he picene. The substrates are all an-isotropic surfaces, which make an alignment of the molecules along the substrates corrugation direction more likely.

3.1.1. Substrate surface unit cell

The lattice constant of Ag is $a = 4.08$ Å and $a = 3.61$ Å for Cu. Based on the lattice constant the area of the surface unit cell Ω and their vectors $\vec{a}$ and $\vec{b}$ are derived by the subsequent equations taken from Irrera, S. (2005). *Structural and Electronic Properties of Chiral Molecules on Surfaces.* PhD Thesis.Dipartimento di Chimica ,UNIVERSITA DEGLI STUDI DI ROMA.

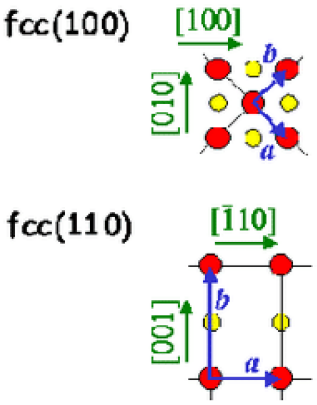

Figure 3.1.: Structure of a fcc(100) and a fcc(110) surface by Irerra (citation page 15) . The red spheres are in the 1st, the yellow in the 2nd plane beneath. $\vec{a}$ and $\vec{b}$ are the 2D surface lattice vectors and the square braces indicate the directions on the surface .

The surface unit cell for a fcc(110) face following the principles in fig. 3.1 is given by:

$$\vec{a} = \frac{a}{\sqrt{(2)}}\,(1,0)\,\mathring{A} \tag{3.1}$$

$$\vec{b} = a\,(0,1)\,\mathring{A} \tag{3.2}$$

$$\Omega = \frac{a^2}{\sqrt{(2)}}\,\mathring{A}^2 \tag{3.3}$$

In case of a fcc(100) surface unit cell the situation is again sketched in 3.1 and leads to:

$$\vec{a} = \frac{a}{2}\,(1,-1)\,\mathring{A} \tag{3.4}$$

$$\vec{b} = \frac{a}{2}\,(1,1)\,\mathring{A} \tag{3.5}$$

$$\Omega = \frac{a^2}{2}\,\mathring{A}^2 \tag{3.6}$$

Inserting for Ag(110) gives:

$$\vec{a} = 2.8\,(1,0)\,\mathring{A} \tag{3.7}$$

$$\vec{b} = 4.0\ (0,1)\ \mathring{A} \tag{3.8}$$

$$\Omega = 11.7\ \mathring{A}^2 \tag{3.9}$$

This leads to a distance from one row to the other on the Ag(110) surface of 4.0 Å concerning eq.3.2.

Inserting for Ag(100) gives:

$$\vec{a} = 2.0\ (1,-1)\ \mathring{A} \tag{3.10}$$

$$\vec{b} = 2.0\ (1,1)\ \mathring{A} \tag{3.11}$$

$$\Omega = 8.3\ \mathring{A}^2 \tag{3.12}$$

20.4 nm is the distance between the quadratic arranged 1st layer on Ag(100).

Inserting for Cu(110) gives:

$$\vec{a} = 2.5\ (1,0)\ \mathring{A} \tag{3.13}$$

$$\vec{b} = 3.6\ (0,1)\ \mathring{A} \tag{3.14}$$

$$\Omega = 9.21\ \mathring{A}^2 \tag{3.15}$$

Cu(110), again with a rectangular surface unit cell has 3.6Å distance between the rows concerning eq.3.2.

The passivation of Cu(110) leads to oxygen rows in the [001] direction in a 5.1 Å distance, which is in 90° to the pristine copper surface.

3.1.2. Substrate electronic structure

In case of metals, HeI photoemission spectroscopy images the electronic structure, especially of the valence band. With eq. 2.9 the calculation of the metal specific work function from the EDC spectra was accomplished.

Table 3.1 compares the work functions of the single-crystals used in the experiments and their values taken from Hölzl and Schulte, 1979.

substrate	work function exp.	work function lit.
Ag(110)	$\Phi = 4.39$ eV	$\Phi = 4.52$ eV
Ag(100)	$\Phi = 4.77$ eV	$\Phi = 4.64$ eV
Cu(110)	$\Phi = 4.57$ eV	$\Phi = 4.48$ eV
Cu-p(2x1)O	$\Phi = 4.97$ eV	no reference

Table 3.1.: List of the experimental derived work function values of the used single crystals and their literature ones.

Unfortunately the LEED wasn't working throughout the experimental time frame, which makes the measurement directions arbitrary. A default azimuth adjustment was taken by applying the single crystal's placement in preceding experimental setups, to get as close as possible to the predominant directions.
The valence orbitals in the electron configuration of Ag $[Kr]4d^{10}5s^1$ can be found in the EDC spectra of Ag(110) in fig.3.2a as well as for Ag(100) in fig.3.2b under different polar angular adjustments together with the HeI satellite.
The same applies for the outermost orbitals of copper. The 4s- as well as the 3d-band mentioned in the electron configuration of Cu $[Ar]3d^{10}4s^1$ are visualized in the EDC spectra of Cu(110) in fig.3.3a as well as for Cu-p(2x1)O in fig. 3.3b. The HeI satellites are expected just below the Fermi edge, but are too weak to be discerned.

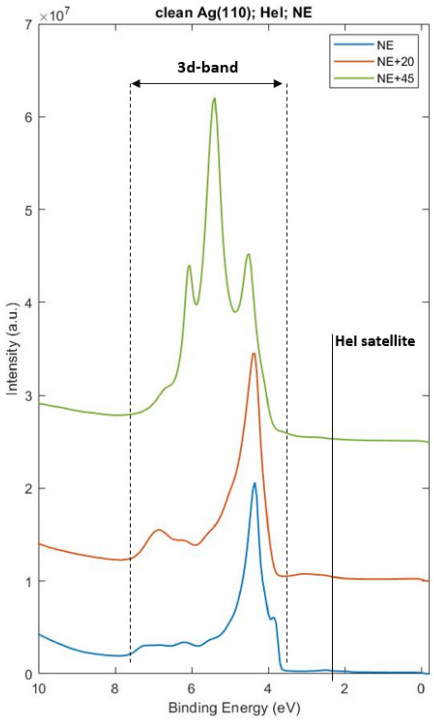

(a) EDC spectra of Ag(110) in 3 polar adjustments (see inset top right) with the metal 3d-band and the HeI satellite.

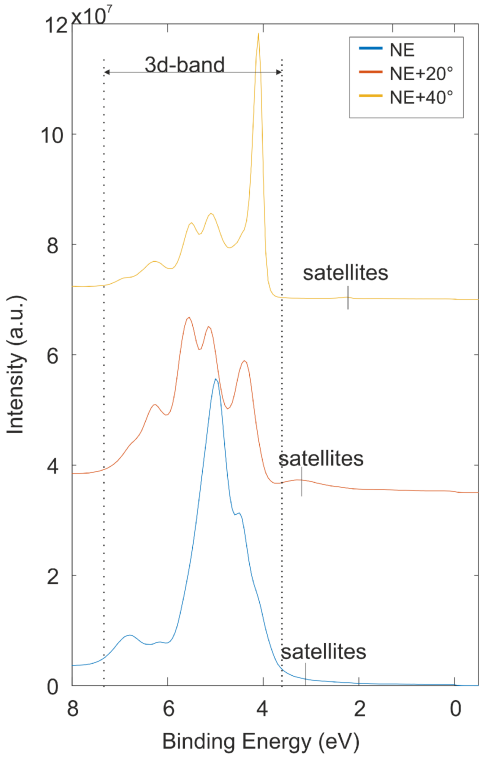

(b) EDC spectra of spectra of Ag(100) in 3 polar adjustments (see inset top right) with the metal 3d-band and the HeI satellite.

Figure 3.2.: HeI photoemission spectra of Ag(110) and Ag(100) in 3 different polar angles.

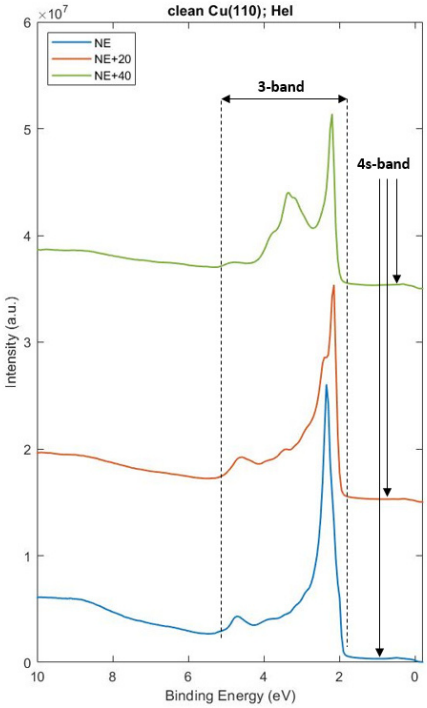

(a) EDC spectra of Cu(110) in 3 polar adjustments (see inset top right) with the metal sp- as well as 3d-band.

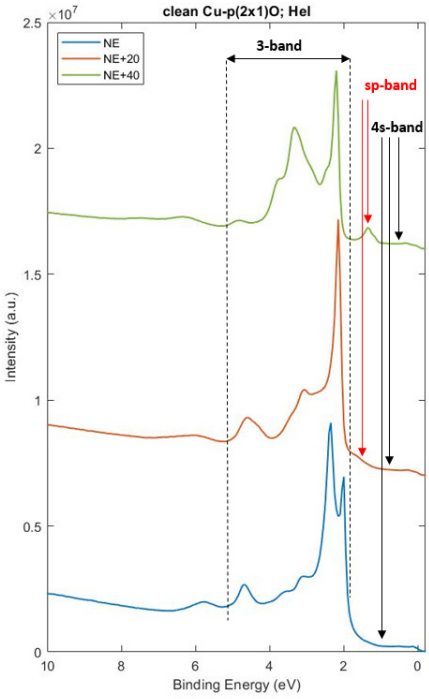

(b) EDC spectra of Cu-p(2x1)O in 3 polar adjustments (see inset top right) with the metal sp - as well as 3d-band.

Figure 3.3.: HeI photoemission spectra of Cu(110) and Cu-p(2x1)O in 3 different polar angles.

3.2. The organic molecule - Picene

Picene, $C_{22}H_{14}$, is an isomer of pentacene with an armchair arrangement of its five benzene rings (Kelly et al., 2016), pictured side by side in fig.3.4b and fig.3.4c. It condenses in a monoclinic crystal formation with lattice constants $a = 8.48$ Å, $b = 6.154$ Å, $c = 13.515$ Å and $\beta = 90.46°$. It belongs to the $P2_1$ space group and a unit cell contains two non-equivalent molecules (Roth et al., 2010).
Picene shows superconductivity with K doping ($T_c = 20°$ K) along with a high hole mobility (3 cm^2V^{-1} s^{-1}) and a strength against oxidation, which

rests on its bigger band gap of 3.3 eV compared to other similar polyacenes like pentacene with 2.2eV. This makes Picene a promising future material for semiconductor devices (Liu et al., 2014).

3.3. Electronic structure of Picene

The DOS as well as the structure formula of Picene is somewhat in between the n-phenyle like arrangement of 3P and the n-acene like one of 5A (fig. 3.4a to 3.4c).

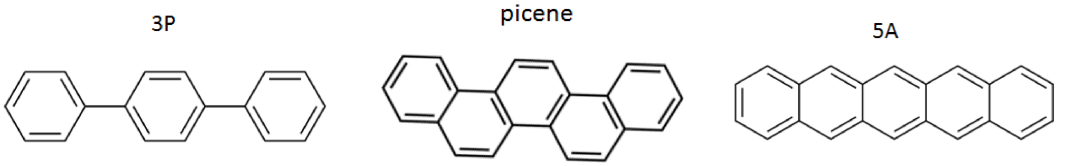

(a) Structural formula of 3P with terphenyl like bonding

(b) Structural formula of picene, uniting both binding types.

(c) Structural formula of 5A with acene like bonding.

Figure 3.4.: Structural formulas of picene (b) versus Terphenyl (a) and Pentacene (c)

Even though picene is an isomer of pentacene with the same number of benzene rings, it has a similar large gap energy in the DOS (fig. 3.5a to fig. 3.5c) as the shorter 3P, indicating that both are closer in their effective conjugation length (fig. 3.4a to 3.4c). And indeed one can see a terphenyl moiety in picene. this lower conjugation is a result of the zig-zag arrangement and also the molecular length of picene is similar to that of terphenyl. Lesser orbital conjugations result in a wider gap, but brings advantage in the stability against oxidation Liu et al., 2014.
Comparing the DOS of the three molecules in fig. 3.5a to fig. 3.5c illustrates that Picene shares a similar binding energy for the HOMO with 3P whereas the number of orbitals subsequent to the frontier orbitals and their splitting resembles that of 5A.

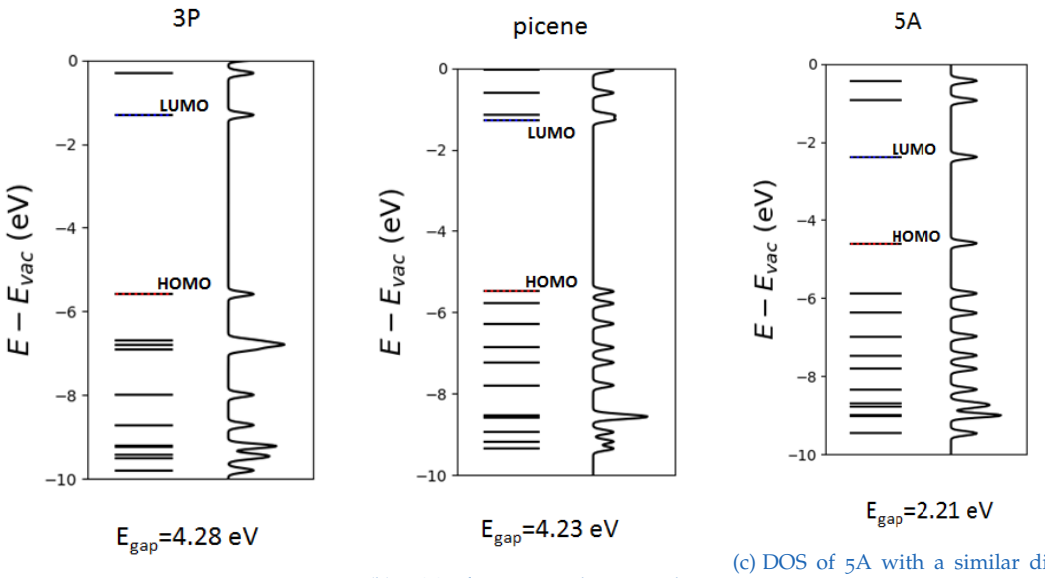

(a) DOS of 3P, with a similar gap to picene.

(b) DOS of picene, in between the one of 3P and 5A.

(c) DOS of 5A with a similar distribution of the HOMOs as Picene.

Figure 3.5.: DFT based DOS of 3P, picene and 5A

The above molecules may also be seen as building blocks of graphene (fig. 3.6). Embedding picene in a graphene structure (fig. 3.6) clearly visualizes the single bonds with terphenyl character in the vertical direction beside the acene- like double bonds in the diagonal orientation.

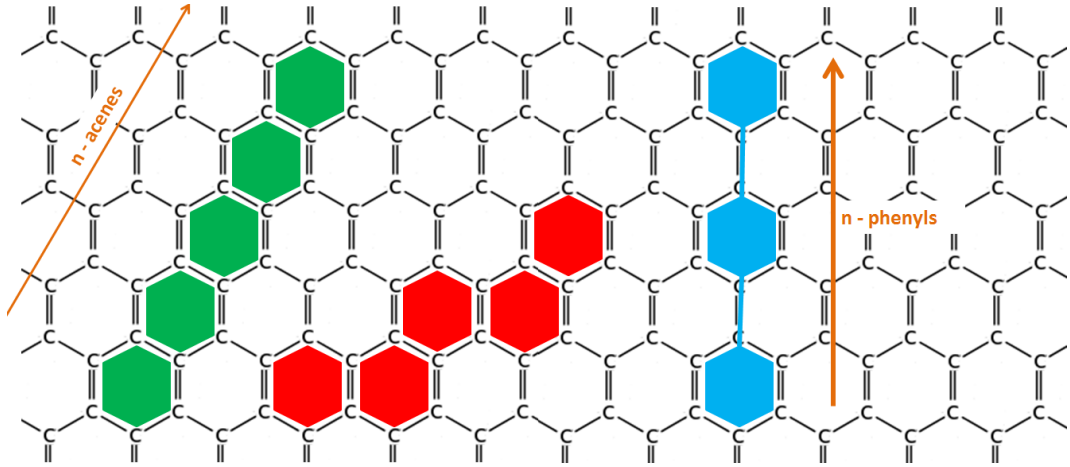

Figure 3.6.: 3P, Picene and 5A embedded in Graphene structure.

With the molecular data base by Puschnig (citation page 12) , based on DFT, the group of Peter Puschnig calculated the DOS and simulated the momentum maps of the LUMO beside the HOMO and the HOMOPuschnig-1 together with their appearance in real space in fig. 3.7a to fig. 3.9b.

The momentum map of the LUMO 3.7b has 2 nodal planes in k_x beside k_y and 4 major loops at $|k_x| = 1.5$ Å^{-1} and $|k_y| = 0.9$ Å^{-1}. The planar orbital is thus only observable at higher polar take off angles and azimuthally not along the molecules main axes.

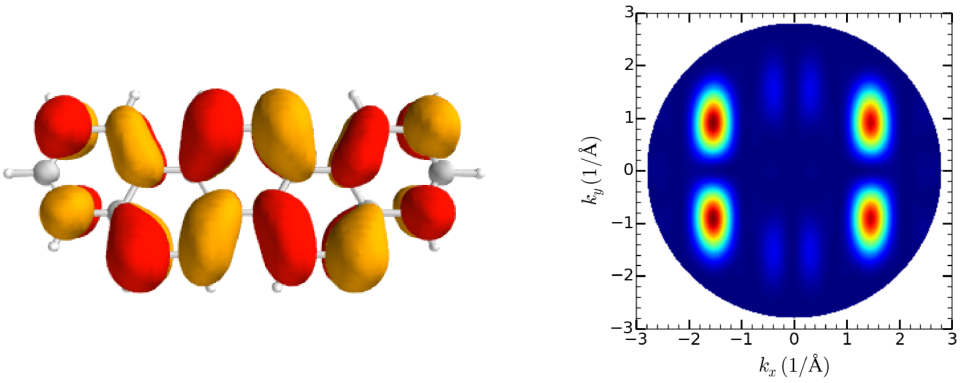

(a) Simulation of the LUMO in real space.

(b) Simulation of the LUMO as momentum map.

Figure 3.7.: DFT based simulations of the LUMO of picene.

The momentum map of the HOMO 3.8b has 1 nodal planes in k_y and 2 major loops at $|k_x| = 0.0$ Å^{-1} and $|k_y| = 1.5$ Å^{-1}. The HOMO can thus be best seen at higher take off angles and perpendicular to the molecular long axis.

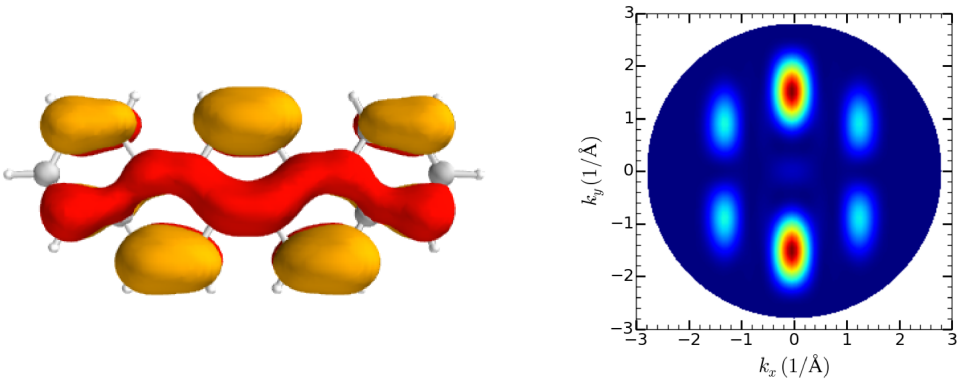

(a) Simulation of the HOMO in real space.

(b) Simulation of the HOMO as momentum map.

Figure 3.8.: DFT based simulations of the HOMO of picene.

The momentum map of the HOMO-1 has 1 nodal plane in k_x and 2 major loops at $|k_x| = 1.5$ Å^{-1} and $|k_y| = 0.0$ Å^{-1}. The HOMO-1 can thus be best

seen at higher take off angles and along the molecular long axis, it should thus posses an opposite dichroism the HOMO.

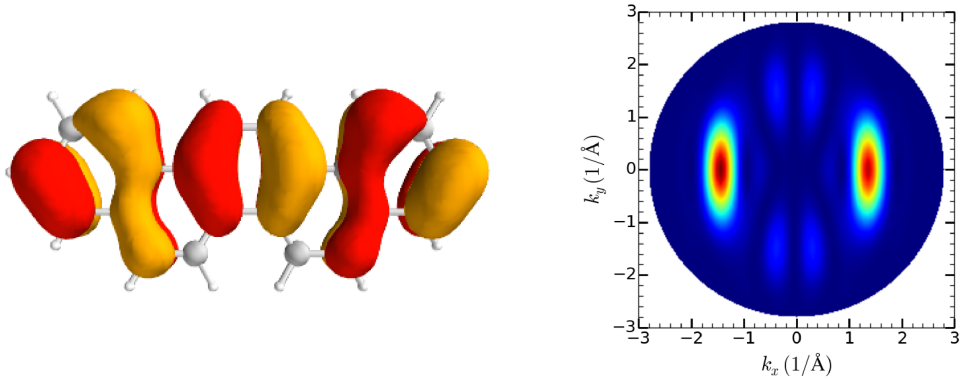

(a) Simulation of the HOMO-1 in real space.

(b) Simulation of the HOMO-1 as momentum map.

Figure 3.9.: DFT based simulations of the picene HOMO-1.

3.4. Picene on Ag and Cu: Status of literature

Picene on Ag(100) has already been described in the literature. Huempfner et al., 2016 investigated the electronic and geometric properties of a monolayer Picene on this surface with LEED, STM and UPS experiments. Kelly et al., 2016 were interested in the understanding of the electronic structure of small coverages up to monolayers of picene on Ag(100), using STM, scanning tunneling spectroscopy and augmented by electronic structure calculations.
Y. Wang et al., 2011 performed DFT calculations in connection with UPS experiments to study the growth and electronic properties of highly crystalline Picene films on Ag(110). Beside LEED even UPS experiments were applied by Q. Wang et al., 2017 for picene on Ag(110) as well as Cu(110).

3.4.1. General - Ag(100)

Huempfner et al., 2016 investigated the molecular structure of 1 monolayer picene on Ag(100). The molecular long axis is oriented along the [010] surface direction.

The basis structure consists of two parallel molecules per unit cell, one face-on and one tilted along it's long axis for 45° to the surface normal grown in a highly ordered point-on-line epitaxy structure.
Kelly et al., 2016 confirmed this findings with the performed STM experiments.

3.4.2. Geometric structure - Ag(100)

Huempfner et al., 2016 monitored the growth mode of picene at room temperature step by step with LEED visualized in fig. 3.10. At low coverages a disc with a four fold symmetry inside emerges (fig. 3.10.a). This suggests a random arrangement, but with minimum distance to neighbour molecules. The four fold symmetry indicate an already starting of orientation along predominant directions imprinted by the substrate.
At even higher coverages (fig. 3.10.b,fig. 3.10.c) the opacity gets weaker and prominent diffraction spots appear. At the thickness of 1 monolayer the highest molecular density is reached and the ring like pattern vanishes completely (fig. 3.10.d). During the increasing of the film thickness the diffraction patterns remains the same. This implies highly ordered islands beside poorly structured areas at low coverages. The growth precedes laterally upon increasing molecular layers.
The spots within and not on the ring-like pattern suggest two molecules per unit cell.
It was possible to assign all the diffraction features in the LEED. The green ones are the expected ones created by the molecules, the blue ones originate from multiple scattering with the substrate (fig.3.11.e, fig.3.11.f).

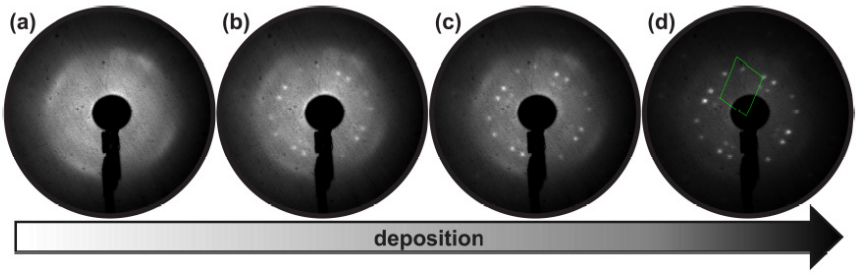

Figure 3.10.: Taken from Huempfner et al., 2016. LEED images during the deposition of picene on Ag(100) at 27 eV.

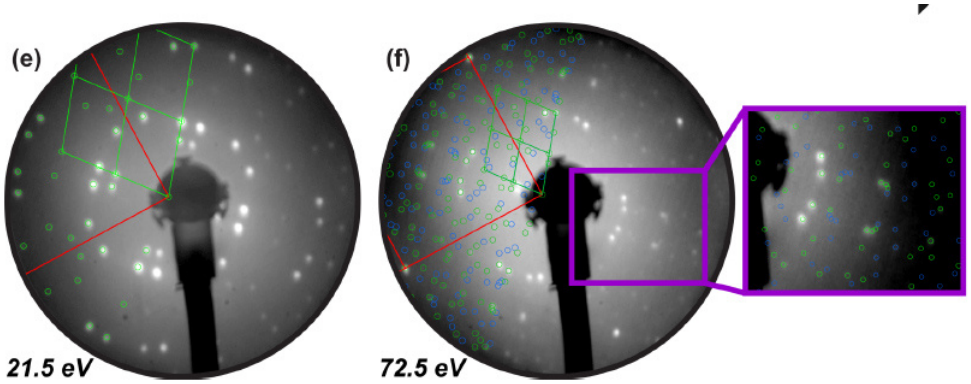

Figure 3.11.: Taken from Huempfner et al., 2016. For better visibility of the diffraction pattern, the intensities are scales logarithmically and distortion was corrected by LEEDCal.

The 1 monolayer epitaxy matrix (eq. 3.16) underlines a point-on-line growth due to the integers in the second column.

$$\begin{pmatrix} 2.41 \pm 0.001 & -3 \pm 0.01 \\ 3.11 \pm 0.01 & 4 \pm 0.01 \end{pmatrix} \tag{3.16}$$

Huempfner et al., 2016 reports bulk-like structure is favoured by Picene even in thin films on metal surfaces with slight modification due to the substrate, asserted with STM. In fig.3.12a the unit cell picked from the LEED (fig. 3.10.d to fig. 3.11.f) is inserted in the STM picture in green. The STM

further allows the conclusion of two diverse orientated molecules per unit cell due to changing contrast of neighbouring molecules (fig. 3.12a).

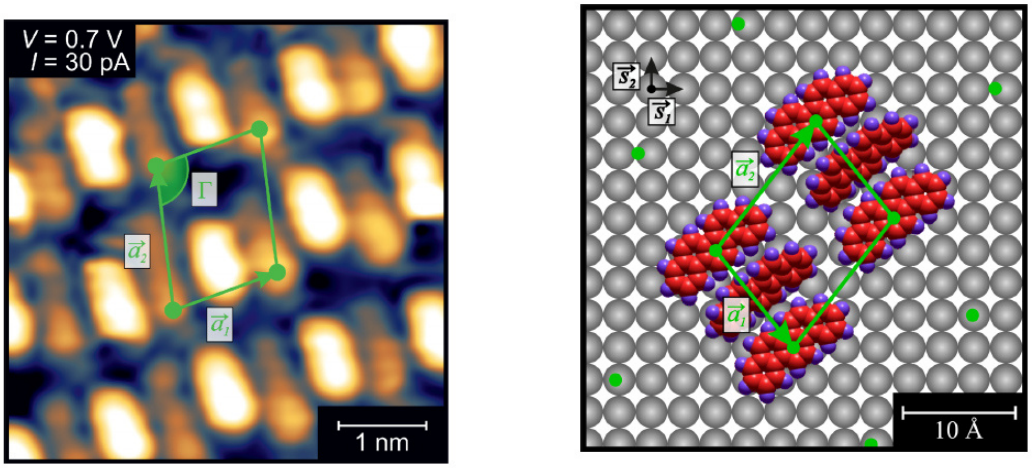

(a) STM image of 1 ML picene on Ag(100) wiht the unit cell found in the LEED inserted in green.

(b) Structural model in arbitrary adsorption sides of picene on Ag(100) based on the measurements.

Figure 3.12.: STM-image and structural model of Picene on Ag(100) by Huempfner et al., 2016.

The structural model of picene on Ag(100) in fig. 3.12b roots on the the outcome of the different experimental methods with arbitrary assumed adsorption sides.

The STM results performed at 77°K and 150°K of Kelly et al., 2016 underline the findings of Huempfner et al., 2016. They too found picene align along the $< 010 >$ direction of Ag(100) (sec.3.1.1).
At low coverages the molecules are isolated due to repulsive interactions. They found Picene lie flat on the surface up to half a monolayer and with one monolayer one molecule in the unit cell starts to tilt for 30° with respect to the plane of the surface.
At still higher coverages in the mulitlayer phase the system precedes in the Stranski Krastanov mode, building 3D islands of two or more layers of picene molecules on top of the monolayer.

3.4.3. Electronic structure - Ag(100)

Huempfner et al., 2016 published measured momentum maps of 1 monolayer with the HOMO at 2.6 eV ,the HOMO-1 at 2.9 eV and the HOMO-2 at 3.5 eV for picene. They also confirmed the 45° tilt of one of the two molecules located in the unit cell. No LUMO filling occurred, the HOMO is well beneath the Fermi-level. The lacking of fine structure in the measured momentum maps indicate no intermolecular interactions.

3.4.4. General- Ag(110)

Y. Wang et al., 2011 investigated the electronic structure in highly crystalline picene films, which grow epitaxially on Ag(110) in a standing-up-orientation.

3.4.5. Geometric structure - Ag(110)

RHEED measurements (fig.3.13) performed by Y. Wang et al., 2011 reveal a highly crystalline Picene monolayer with a good epitaxial relationship to the Ag(110) substrate, supporting a standing-up orientation of the molecules from the start. A monoclinic film structure monitored with the RHEED point in a strong resemblance with the bulk parameters.
They found the unit cell of Picene is 3 times longer in the $[\bar{1}10]$ direction than the one of the substrate. Atomic Force Microscopy showed island growth for multilayers.

Q. Wang et al., 2017 too reckons two molecules in a unit cell, one adsorbed flat beside the second one tilted edge-on and no coverage dependent change in the surface unit cell. The even at multilayer thickness visible Fermi-edge hints at Stranski Krastanov growth mode.

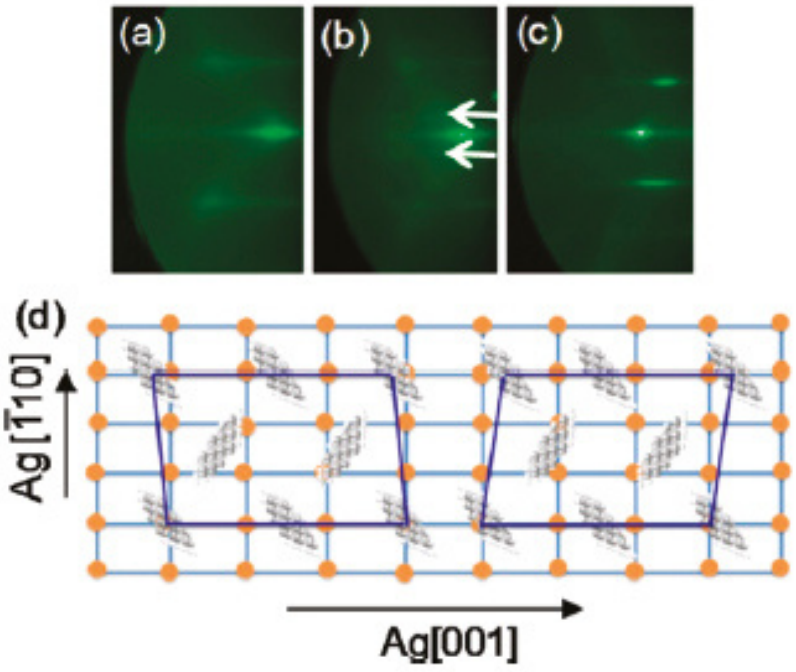

Figure 3.13.: Taken from Y. Wang et al., 2011. RHEED image of a) pristine Ag(110) b) 1 monolayer picene measured along Ag[001] c) 1 monolayer picene measured along Ag[1̄10] d) A sketch of a unit cell of a picene monolayer on Ag(110).

3.4.6. Electronic structure - Ag(110)

The UPS experiments in alignment with the DFT calculations revealed for Y. Wang et al., 2011 in the case of highly ordered picene thin films on Ag(110) the HOMO at 2.6 eV, the HOMO-1 at 3.96 eV and the HOMO-2 at 3.5 eV. On pristine picene films the distance between the HOMO and HOMO-1 acounts only for 0.3 eV like in fig.3.14.

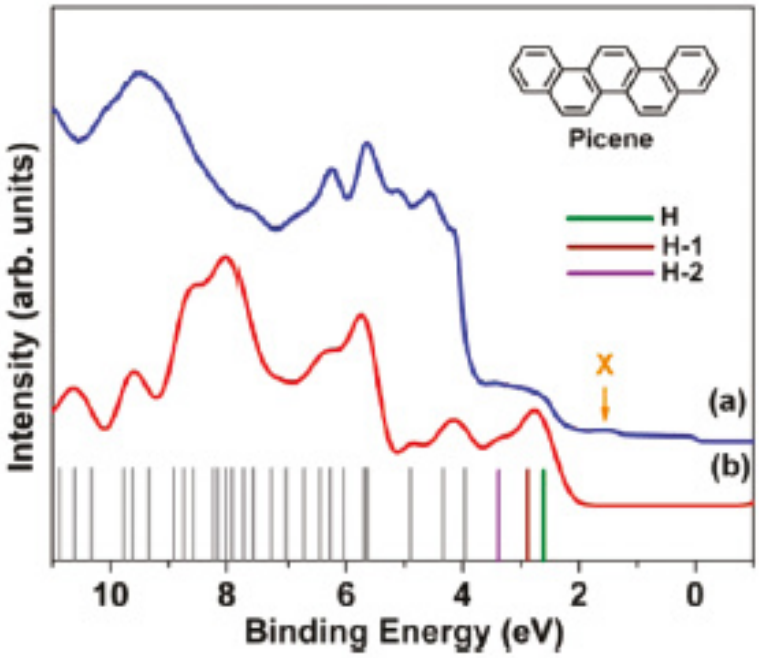

Figure 3.14.: UPS spectra of a picene multilayer on Ag(110) a) measured b)simulated from Y. Wang et al., 2011 with the HOMO and HOMO-1 in a 0.3 eV distance and trapped state at location x.

3.4.7. Cu(110)

Q. Wang et al., 2017 reports a strong overlap of the copper 4s as well as 3d band with the HOMO and HOMO-1 emissions of picene (fig. 3.15). No hybridization, no charge transfer is reported.

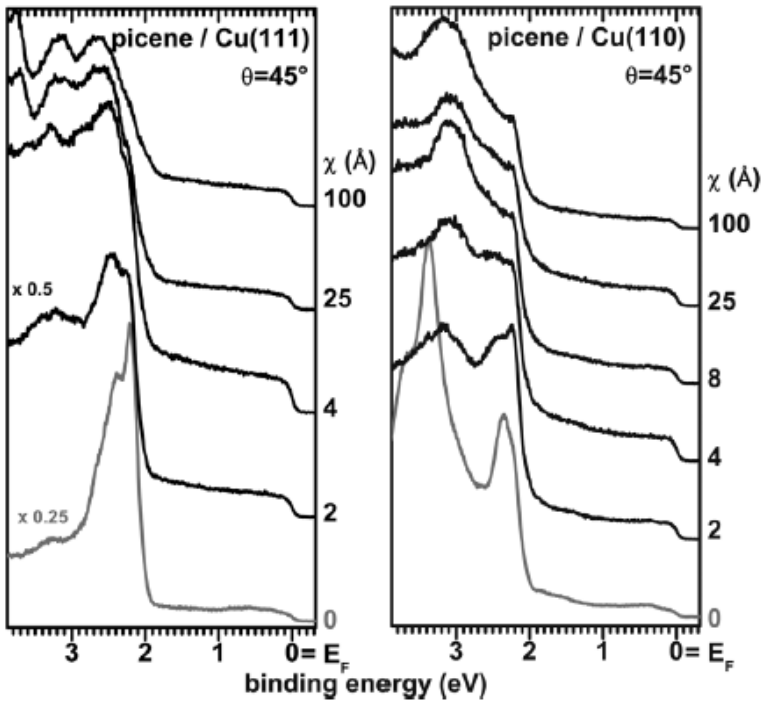

Figure 3.15.: Q. Wang et al., 2017 published in the right picture a dosing series on Cu(110) togehther with the clean metal surface.

3.5. Sample preparation

The sample is mounted on the manipulator and rests in the preparation chamber at a base pressure of $10 \cdot 10^{-10}$ mbar during cleaning procedures and moleculare evaporation. Only for measurements a transition to the analyzer chamber, having the same pressure, is performed.
The cleaning procedure of the single crystal consists of cycles with alternating annealing and sputtering. The degree of surface contamination validates the amount of repetitions. Annealing was always the starting point followed by sputtering. The end of a cleaning cycle was again annealing.
Ag(110) as well as Ag(100) were heated up to $T_c = 21$ mV (550° C) by applying a current of 2.1 A (6.44 V) an a high voltage of 268 V (57.0 mA).

The sputtering was carried out with Argon at a pressure of $p_{Ar} = 1.0 \cdot 10^{-4}$ mbar and a current of 13.3 µA for 30 minutes.
The thermocouple wasn't mounted on the copper single crystal directly, so no direct statements about temperature can be made. However, the annealing temperature of this metal is slightly lower (about 500° C) compared to the one of silver. The settings during annealing were to 2.1 A (6.61V) and a high voltage of 252 V (67.7 mA) for 4 minutes.

To produce a picene film of defined thickness a quarz-micro-balance mounted on the preparation chamber and placed at the sample's later evaporation position, was used. The counting proceeds in digits. For the conversion in Å the molecular density of Picene with 1.2 g\cm^3 is necessary:

$$\frac{1}{1.2} = 0.83 \tag{3.17}$$

For Ag(110) we know from sec. 4 based on the development of the work function that 2 digits are a monolayer, which therefore accounts to $0.83 \cdot 2 = 1.7$ Å.

Additionally we produced an oxygen reduced Cu(110) surface. We started wit flashing the Cu(110) single crystal with 1.3 A for 5 minutes. Afterwards 20 L oxygen, meaning $p_{O_2} = 1.0 \cdot 10^{-7}$ mbar for 200 sec. were dosed into the preparation chamber.

4. The electronic structure of Picene fro monolayers to thin films

4.1. Picene on Ag(110)

Here, we have investigated the electronic structure of picene grown on Ag(110) as a function of coverage with (AR)UPS using HeI (21.22 eV) and HeII (40.82 eV) radiation. The films were mainly grown at room temperatur, but thicker films were also laid at LNT (liquid nitrogen temperature) to avoid island growth.

Fig. 4.1 shows the work function development of picene\Ag(110) as a function of coverage, with the values summarized in Tab. 4.1. The work function saturates already at about 3.57 eV and a coverage of 2 dig., which we defined in the following as a monolayer. Using a density of 1.2 g\cm^3 this corresponds to less than 2 Å (1.63 Å) thickness, see sec. 3.5. The work function remains essentially constant with an uncertainty of $\pm$0.05.eV.

.

surface	work function	color in fig.4.1
clean Ag(110) in Hölzl and Schulte, 1979	$\Phi = 4.52$ eV	non
clean Ag(110) RT	$\Phi = 4.39$ eV	red
clean Ag(110) RT	$\Phi = 4.31$ eV	non
1 di. RT	$\Phi = 3.85$ eV	red
2 di. RT	$\Phi = 3.57$ eV	red
3 di. RT	$\Phi = 3.57$ eV	red
27 di. RT	$\Phi = 3.63$ eV	red
30 di. LNT	$\Phi = 3.55$ eV	blue
81 di. LNT	$\Phi = 3.59$ eV	blue
81 di. thawed	$\Phi = 3.53$ eV	green

Table 4.1.: Table of the coverage dependent work function for a Picene/Ag(110) system.

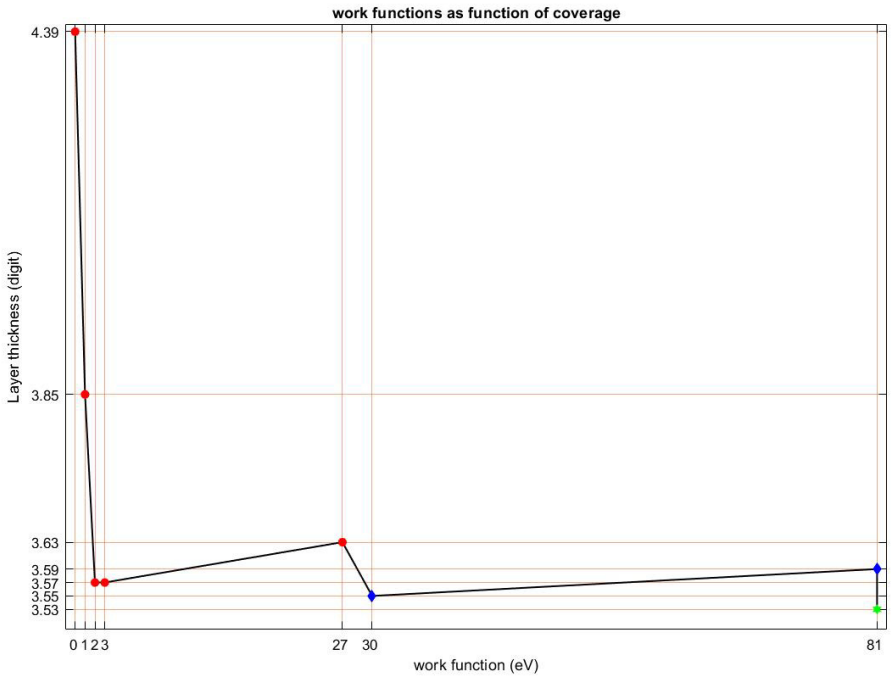

Figure 4.1.: Work function as function of coverage.

Fig. 4.2 and 4.3 show photoemission spectra of picene/Ag(110) as a function of coverage for NE and $NE + 40^{\circ}$ off normal emission geometry, respectively. To identify the emissions, we have included the DOS of gas phase picene (fig.2.8 in sec. 2). The DOS at the top is aligned to the 81 dig. LNT condensed picene film, which we conclude to be free from substrate emissions, as this amounts to about 69 Å high planar molecular layers. The DOS at the bottom is aligned to the 2 dig. Thick film, i.e. a monolayer.
In the thin film spectra in the range of a monolayer the Fermi-edge is clearly visible, but it is also apparent for the 27 dig. RT and the 30 dig. LNT grown films, which indicates island growth. The minor emission at 2.25 eV can be assigned as HeI satellite due to it's absence in the HeII control spectra of the clean Ag(110) surface (fig. 4.9a) and with a monolayer picene (fig. 4.9b). For the bottom three spectra (a 0.5 to 1.5 monolayers) we find an emission at 3 eV which we attribute to comprising both the HOMO and the HOMO-1 orbital and the HOMO-2 being at 3.65 eV, which fits well to the gas phase DOS. Below that orbital at about 4 eV the steep onset of the metal 3d-band rises. The coverage is too low as to be able to suppress the metal features significantly like the multilayers.

Lets consider now the top spectrum in 4.2, the 81 dig. LNT grown multilayer. At first we notice that the HeI satellite is now to weak to be recognized. The DOS aligned to the multilayers match the peaks, by assuming a collective shift of 0.40 ± 0.05 eV to higher binding energies, which we attribute to the worse screening in the condensed molecular film, compared to molecules in direct contact with a metal substrate. Again the leading peak at about 3.1 eV contains both HOMO and HOMO-1 orbitals.

Considering now the thinner LNT multilayer of 30 dig. and the 27 dig. one laid at RT, we find indications that both monolayer and mulitlayer features are superimposed. For instance the leading peak at 2.5 to 3.5 eV seems to consist of two maxima, separated by about 0.4 eV. The first plateau at 2.6 eV contains the HOMO and HOMO-1 of the monolayer, while the second maxima at about 3.3 eV contains the HOMO and HOMO-1 of the multilayer.

This points towards a Stranski Krastanov growth mode with first a monolayer growth followed by the multilayer islands.

In 4.3 the same series is presented for a photoelectron take-off angle of 40°, which supports the above made statements. Regarding the individual spectra now angular differences are apparent, which may be due to a non oriented molecular layer or an unfavorable experimental geometry, which due to the non working LEED could not be exactly determined.

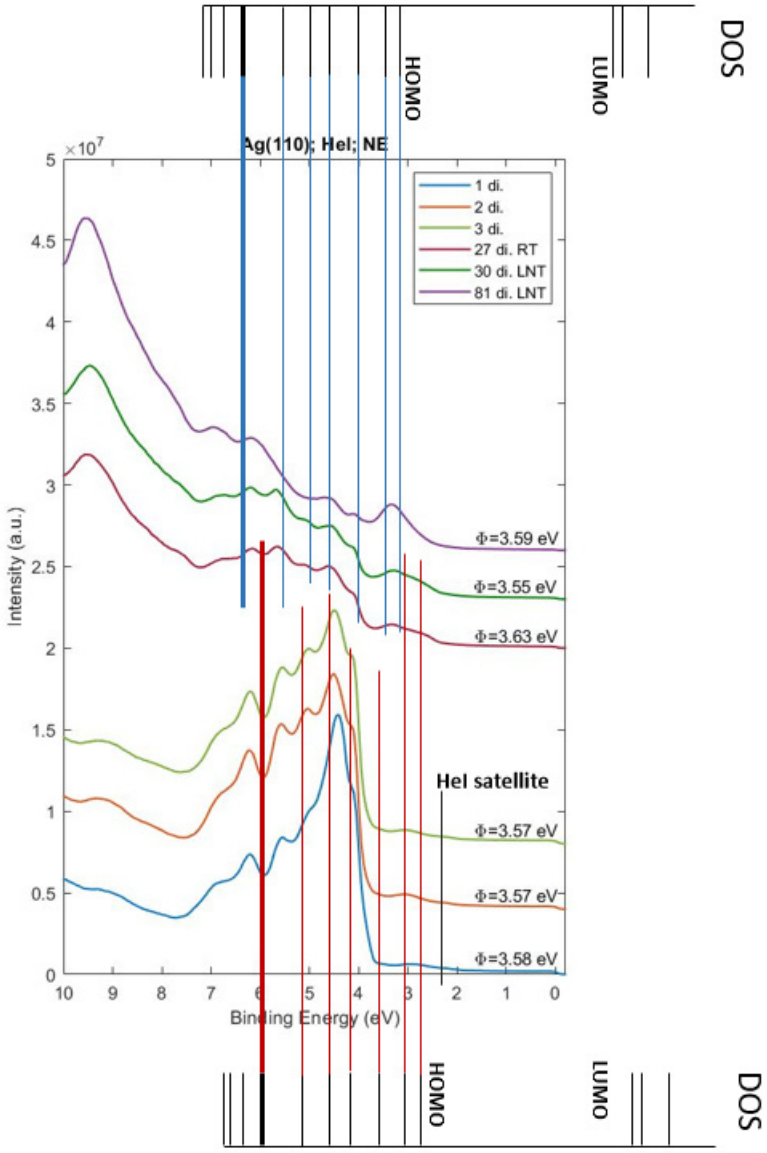

Figure 4.2.: HeI photoemisssion spectra recorded in NE ($\theta = 254°$) of Picene on Ag(110) as a function of coverage (see inset top right). The respective work functions are included. The picene calculated by DOS shown at the top has been aligned to the lowest binding energy emission of the 81 di. LNT film, while the DOS at the bottom is aligned to the respective emission o the 2 di. film. Structure from the HeI satellite are indicated, the Ag d-band is visible in the steep slope at 4.0 eV in the thin films comparable to the pristine surface in sec. 3.

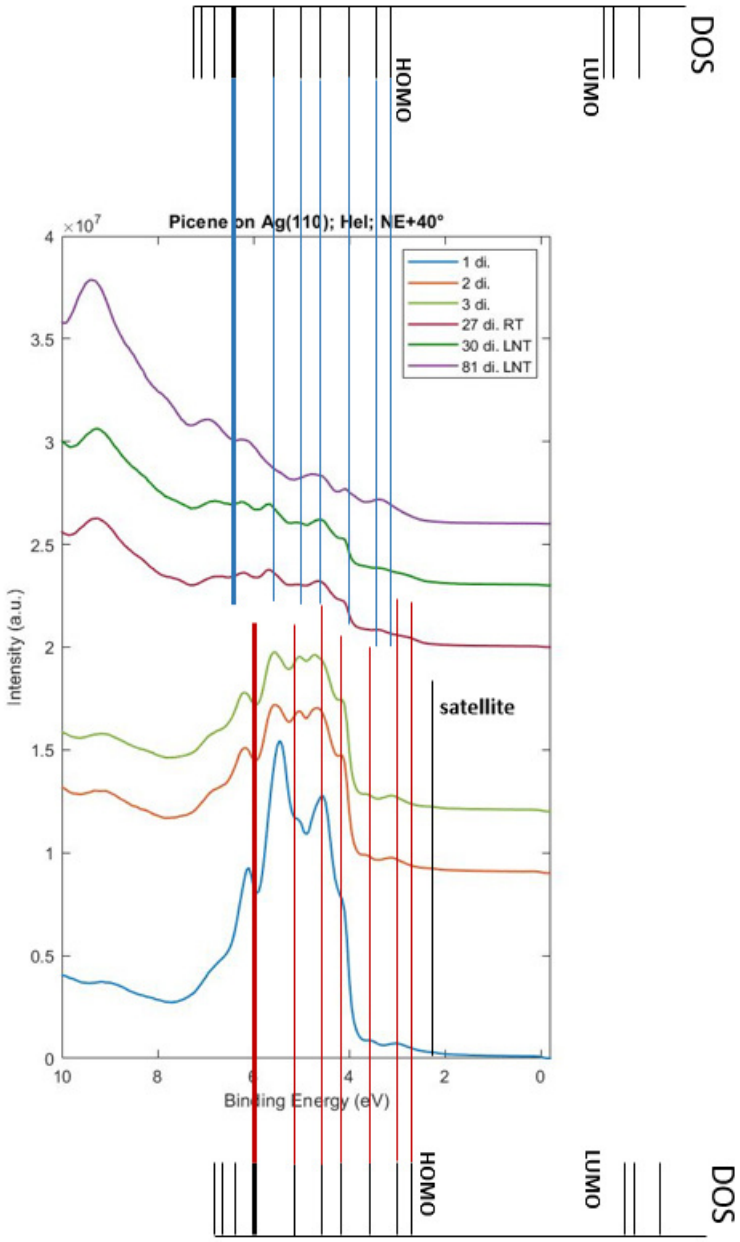

Figure 4.3.: HeI photoemisssion spectra recorded in $NE + 40°$ of Picene on Ag(110) as a function of coverage (see inset top right). The DFT based DOS of Picene at the top is aligned to the frontier orbitals of the 81 di. LNT multilayer as well as to the 2 di. monolayer at the bottom. The HeI satellite clearly emerges in the thin films. The imprint of the d-band clearly shines through in the steep onset at 4 eV in the low coverages, and is suppressed in the thick films.

In fig. 4.4 we compare a multilayer adsorbed at RT, with one produced entirely at LNT and the same one after 12 hours of thawing back to RT. The LNT phase is strikingly different to the other two. The DOS is aligned to the LNT phase, which is different in it's appearance to the other two. In the condensed phase the molecular features start with the HOMO and HOMO-1 of the multilayer merged into one peak. In case of the RT multilayer and the thawed one a broader shoulder occur carrying the HOMO as well as the HOMO-1 of the monolayer ahead of the ones belonging to the thicker film. This is a result of the Stranski Krastanov growth mode. It is interesting, that the condensed phase reconstructs in the process of thawing into the same configuration as the multilayer at RT. At around 6.3 eV again a splitting of the single peak in the condensed phase into two separate ones in the other multilayers exist, but this time the origin can only be guessed.

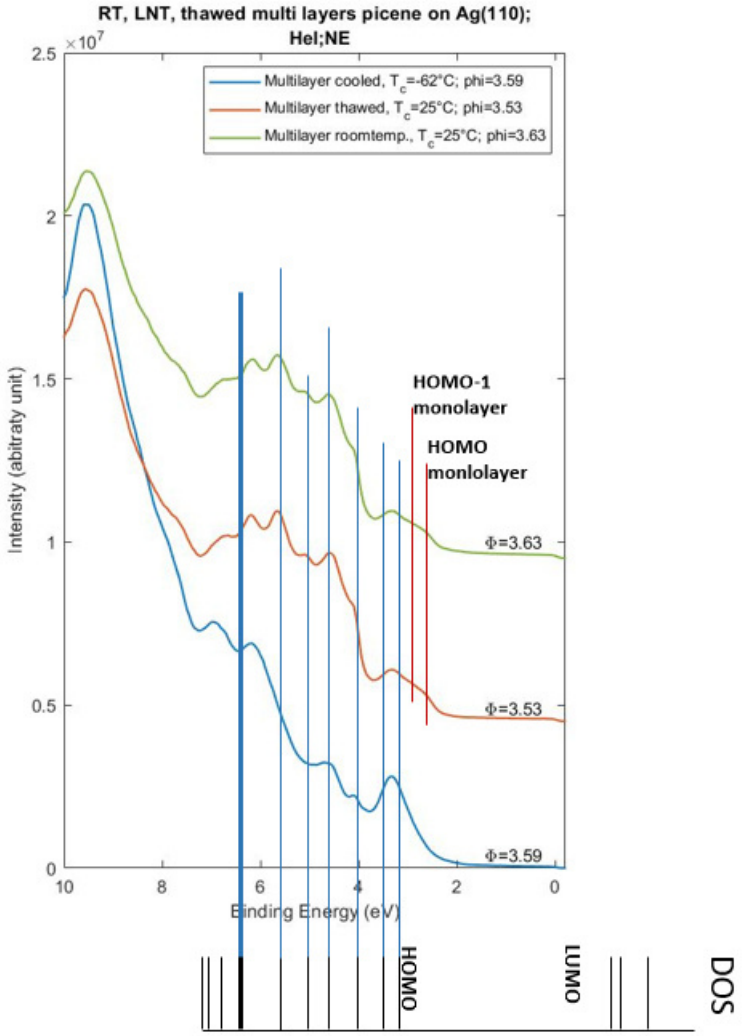

Figure 4.4.: HeI photoemisssion spectra recorded in NE ($\theta = 254°$) of Picene multilayers on Ag(110) produced at RT, entirely at LNT and this one thawed over 12 h back to RT (see inset top right). The respective work functions are included. The adjustment of the DOS to the LNT phase matches the emissions of the other thick films too. In the RT and thawed multilayer the HOMO and HOMO-1 of the monolayer shine through. No temperature induced shift of the high coverage frontier orbitals occurs.

Fig. 4.5 directly compares the graphs of clean Ag(110) and with a monolayer Picene for three different polar angles. From this we can assign the picene orbitals from HOMO down to HOMO-3. The orbitals show no noticeable angular dependencies, indicating no preferred orientation. In particular for a planar orientation the momentum maps of these orbitals would have no intensity at normal emission, which is not observed in the data.

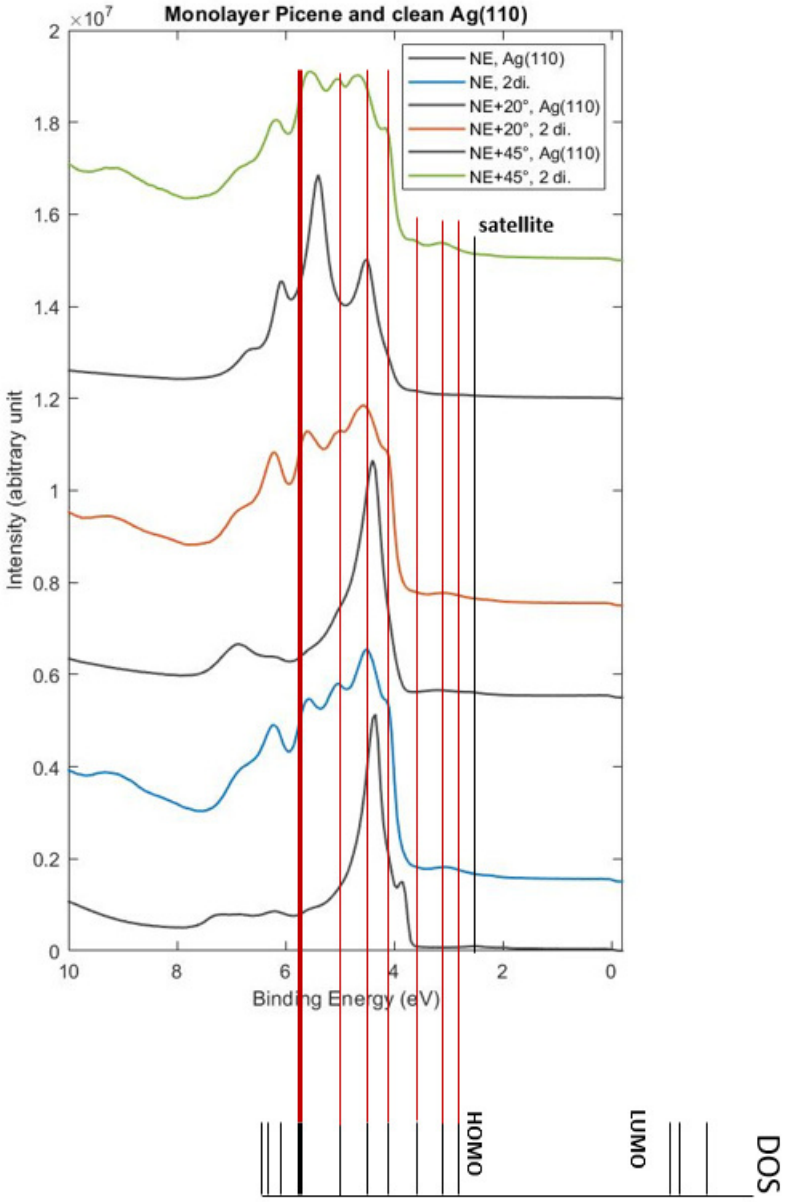

Figure 4.5.: HeI photoemission spectra recorded for alternating clean Ag(110) and monolayer Picene in 3 different polar adjustments (see inset top right). The intensities for a monolayer Picene in NE as well as $NE + 20°$ are diminished by a factor of 0.35, all others by a factor of 0.5.

In the following figures 4.6, 4.7 and 4.8, He I ARUPS measurements of a picene monolayer are shown for the nominal [001], the [1-10] and 45° to [001], respectively. Note that due to a not working LEED the orientations are rather arbitrary and results from a visual comparison of the crystal appearance and earlier measurements. Again no particular angular dependency for the three anzimuthal directions is perceived, indicating no preferred orientation.

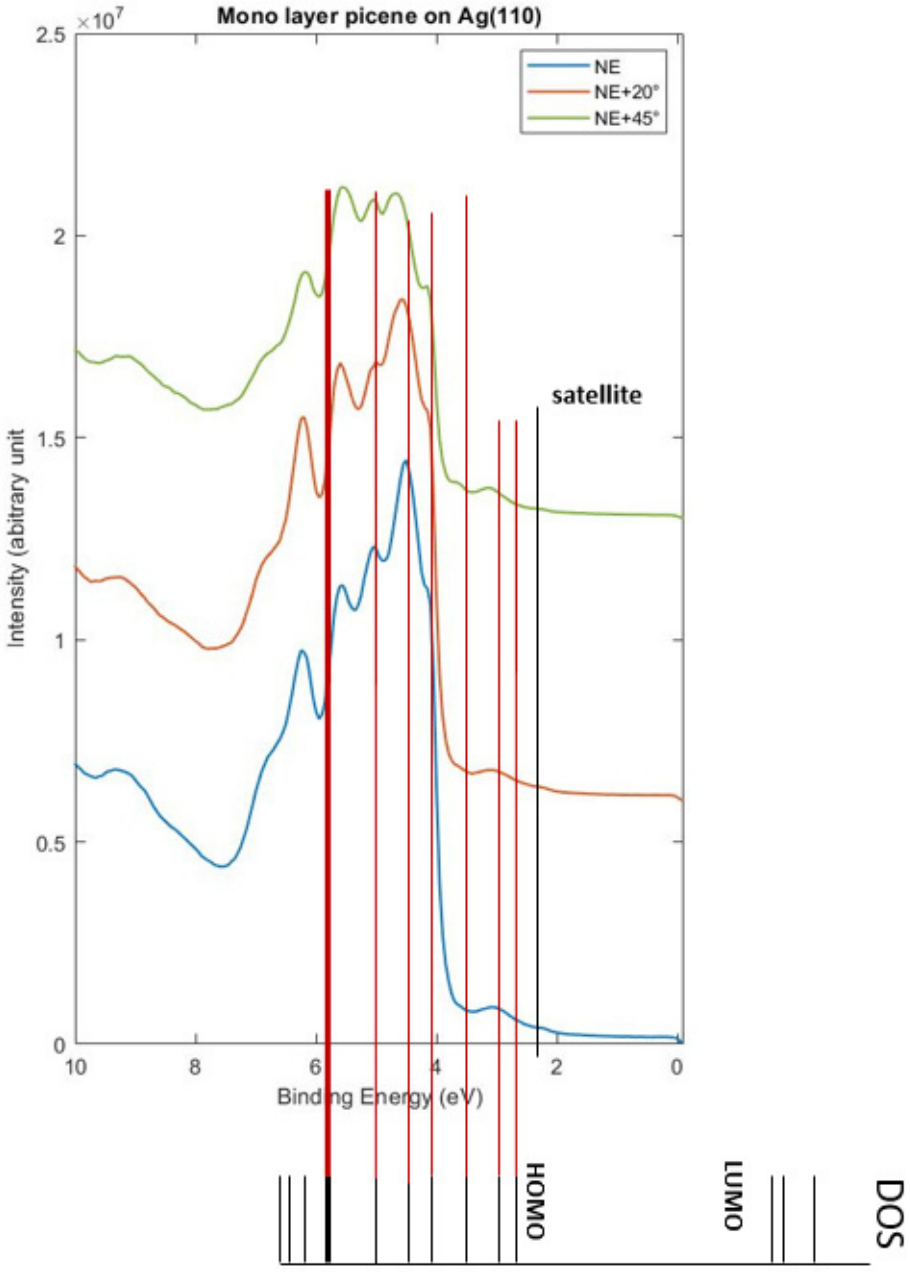

Figure 4.6.: HeI photoemission spectra recorded for and monolayer Picene in 3 different polar adjustments (see inset top right) in the default azimuth. The alignment of the DOS to the monolayers show no significant change of the HOMOs due to the angular changes. The imprint of the metal-d band is most significant in the steep rise of the monolayer curves around 4 eV. The HeI satellite clearly emerges.

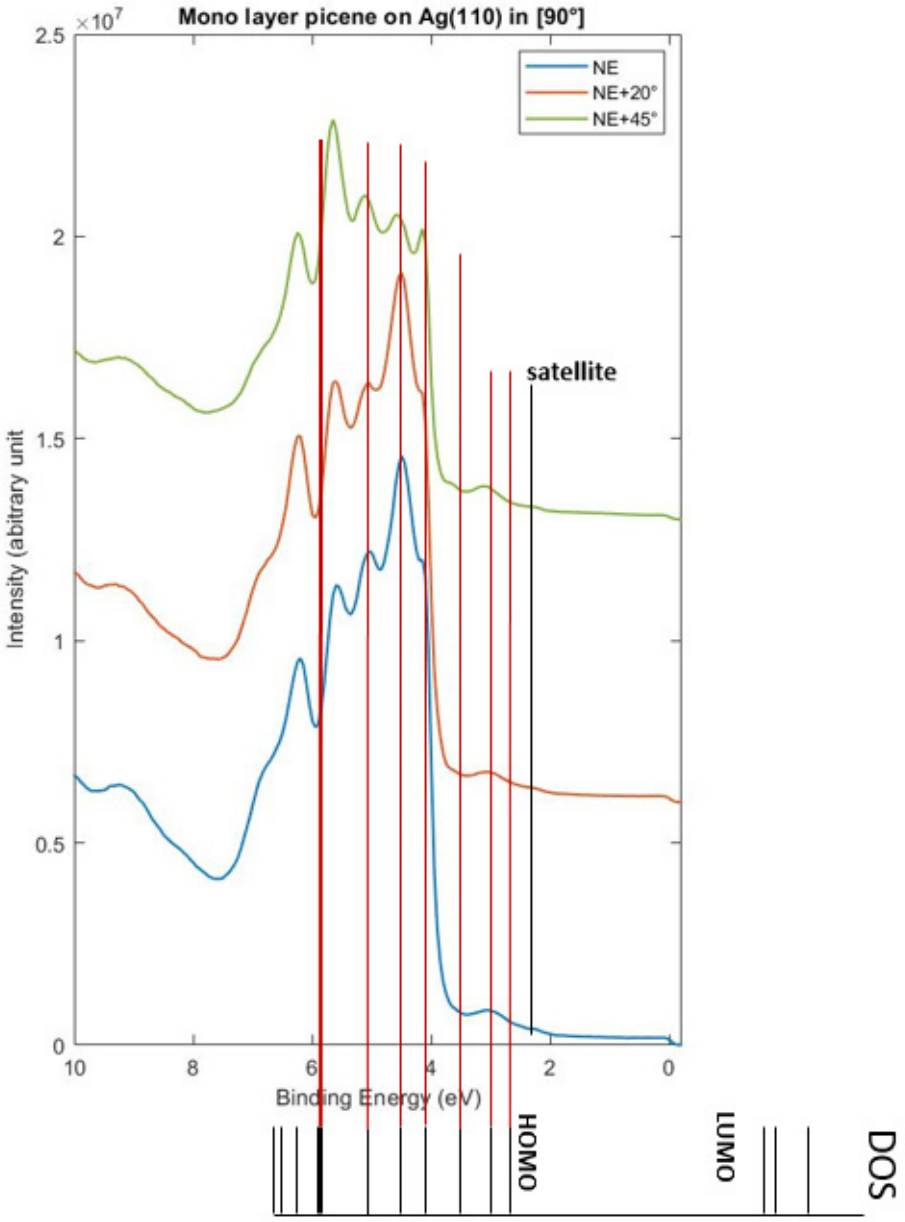

Figure 4.7.: HeI photoemission spectra recorded for and monolayer Picene in 3 different polar adjustments (see inset top right) in [90°] off the default azimuth. The alignment of the DOS to the monolayers show no significant change of the HOMOs due to the angular changes. The imprint of the metal-d band is most significant in the steep rise of the monolayer curves around 4 eV. The HeI satellite clearly emerges.

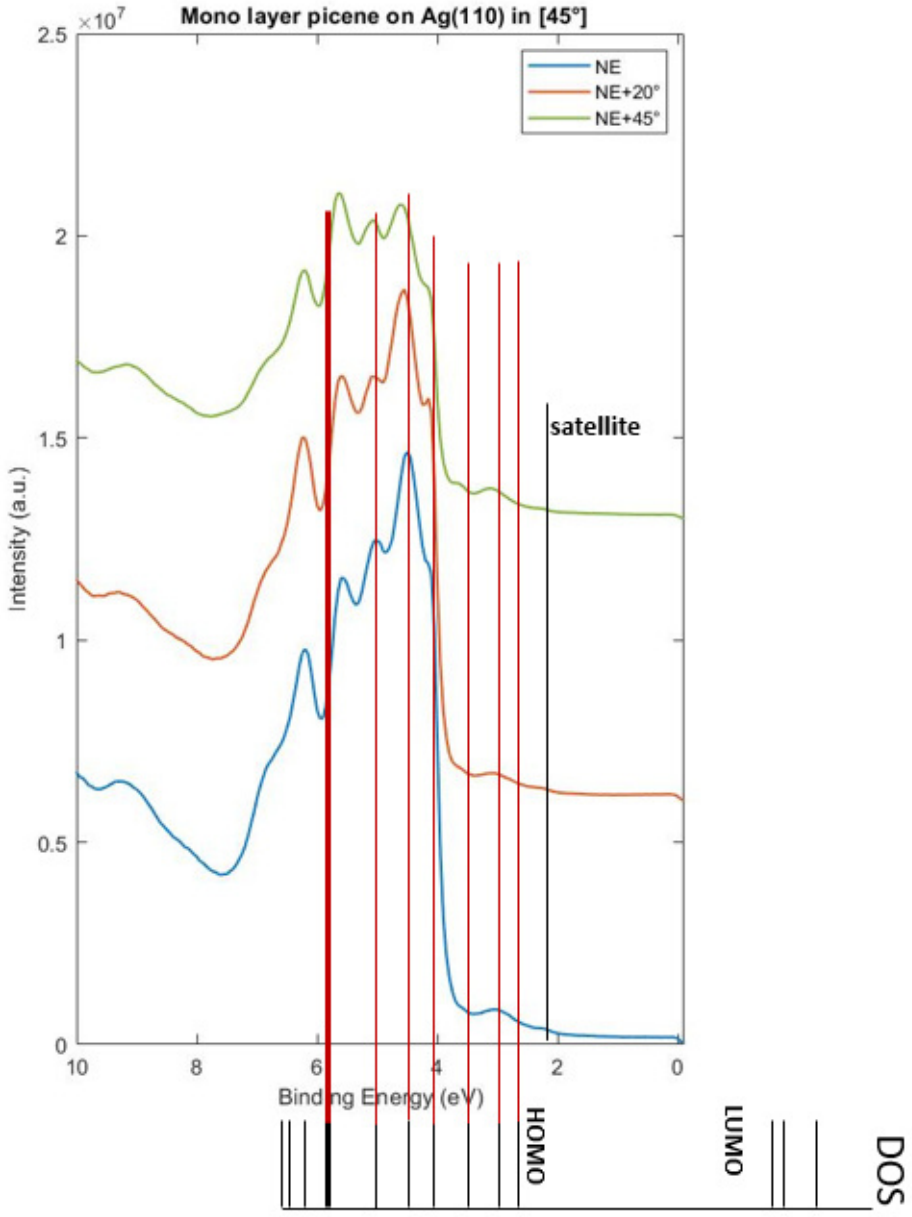

Figure 4.8.: HeI photoemission spectra recorded for and monolayer Picene in 3 different polar adjustments (see inset top right) in [45°] off the default azimuth. The alignment of the DOS to the monolayers show no significant change of the HOMOs due to the angular changes. The imprint of the metal-d band is most significant in the steep rise of the monolayer curves around 4 eV. The HeI satellite clearly emerges.

n.

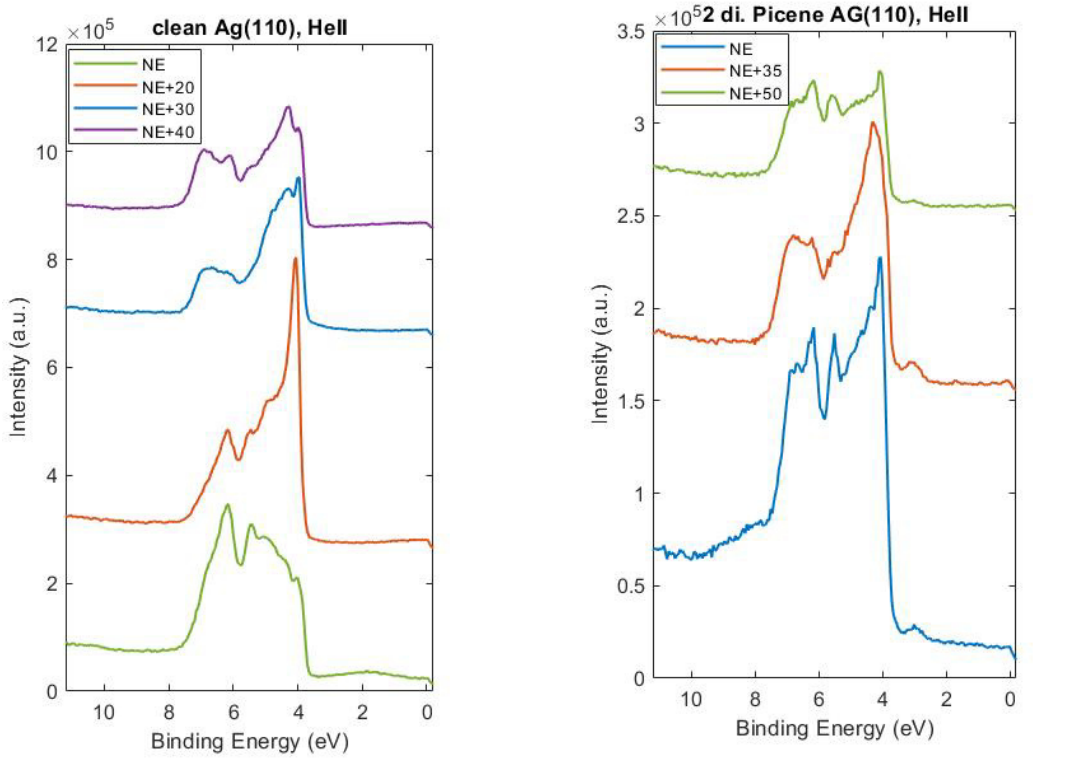

(a) He II EDC spectra of clean Ag(110) in NE, $NE + 20°$, $NE + 30°$.

(b) He II EDC spectra of Ag(110) with a mono layer picene exhibits in all three polar angles a peak at 3.45 eV.

Figure 4.9.: HeII photoemission spectra of clean Ag(110) and with a monolayer Picene)

In fig. 4.9 He II ARUPS of the clean Ag(110) 4.9a is compared to that of a monolayer of picene. From the molecular orbitals only the peak consisting of HOMO and HOMO-1 can be clearly discerned at 2.5 eV. No clear angular behavior is found however, the aforementioned peak seems to have a maximum for 35°, not incompatible with a near planar absorption geometry.

In summary the alignment of the DOS to the mono- as well as the multilayers show a uniform shift of all frontier orbitals accounting for 0.40 ± 0.05 eV to

higher binding energies for thicker films. No clear angular dependency was found for the molecular orbitals irrespective of coverages or changes in the polar and azimuthal orientation. Furthermore the appearance of the Fermi-edge and the strong d-band at above a monolayer thickness indicate island growth, developing in Stranski Krastanov growth mode for multilayers. Even for a fully covering condensed multilayer at LNT, upon warming up to room temperature the molecules restructure into islands.

In comparison with literature in sec.3, we were able to perform the same experimental output as Y. Wang et al., 2011 for the HOMO, HOMO-1 as well as the HOMO-2 in the multilayer. They further states a growth in multilayer islands due to the still prominent Fermi-edge at high coverages of 35 Å, which is conform to our findings.
The fact that we see molecular features in NE speaks contra a flat lying assembling of the molecules on the Ag(110) surface. Indeed, Y. Wang et al., 2011 proclaims a standing-up orientation from the start based on RHEED (Reflection high-energy electron diffraction) and Q. Wang et al., 2017 a monolayer structure of one tilted beside one flat molecule due to LEED measurements.

4.2. Picene on Ag(100)

In this section we focus on the electronic structure of picene on Ag(100) in dependency of the picene coverage applying HeI photoemission spectroscopy and XPS. All films are grown at room temperature. Lacking a LEED the azimuth remains undefined throughout all the succeeding measurements.

Fig. 4.10 visualizes the work function evolution with dosage form tab. 4.2. The work function for Picene on Ag(100) decreases rapidly with increasing picene exposure and levels of at about 2 dig., which will be defined as a monolayer. Using the picene density of 0.86 g/cm^3, and 2 di. exposure, a monolayer on silver is reached at about 1.6 Å. A distinct multilayer with 50 di. thus amounts to nominally 41.5 Å.

surface	work function
clean Ag(100) in Hölzl and Schulte, 1979	$\Phi = 4.64$ eV
clean Ag(100) RT	$\Phi = 4.77$ eV
1 di. RT	$\Phi = 3.78$ eV
2 di. RT	$\Phi = 3.61$ eV
10 di. RT	$\Phi = 3.57$ eV
50 di. RT	$\Phi = 3.50$ eV

Table 4.2.: Work function related to Picene layers on Ag(100).

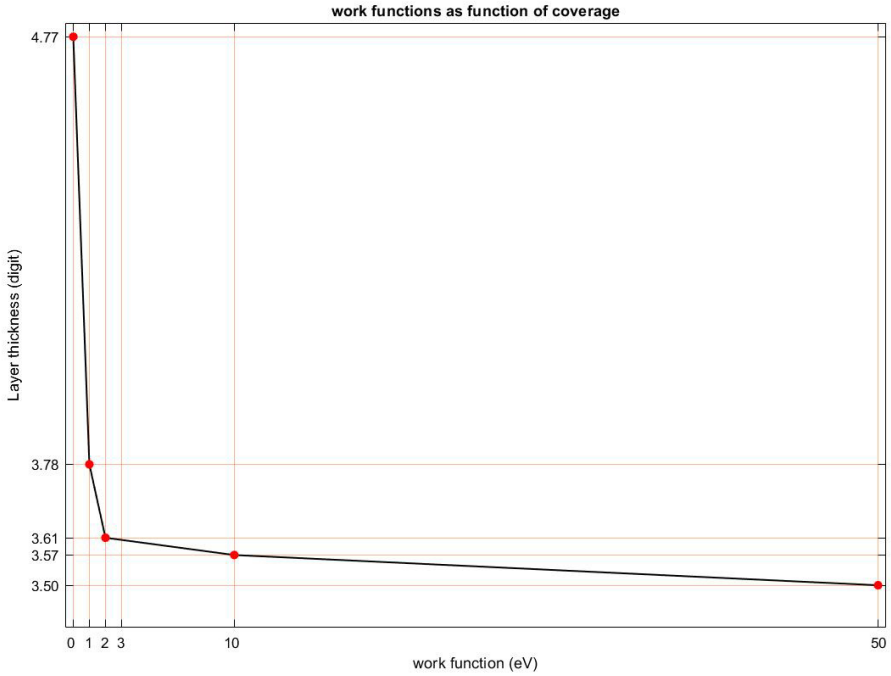

Figure 4.10.: The work function evolution of Picene on Ag(100). The monolayer is defined at 2 dig..

In section 2.3 we outlined a method to assign peaks in the EDC spectra by inserting the work function of the monolayer into eq.2.10 to align the calculated DOS. This has been applied to fig. 4.11 to 4.13 and the DOS aligned for

the monolayer is displayed below each figure. Fig. 4.11 to 4.13 show coverage dependent He I photoemission spectra of picene films on Ag(100) for three polar electron take-off angles NE, $NE + 20°$ and $NE + 40°$. The He I satellite emission is marked for the clean substrate, shown at the bottom of each film.

surface	Φ	**HOMO**	**HOMO-1**	**HOMO-2**
2 di. RT	$\Phi = 3.61$ eV	2.65 eV	2.95 eV	3.45 eV

Table 4.3.: Positions of the frontier orbitals in a monolayer Picene on Ag(100) based on the Φ of the EDCs together with the DOS, calculated using 2.10.

In NE geometry of fig. 4.11 the HeI satellite at about 3 eV is weak and thus will not interfere with molecular features. First we consider the sub-monolayer and the monolayer at 1 di. and 2 di. respectively. The positions of the HOMO to the HOMO-2 are well visible before the onset of the Ag d-band at 4 eV and agree excellent with the DOS included in the bottom of the figure. Even deeper lying orbitals, overlapping wit the Ag d-band, can be identified from the calculated DOS. Looking at the 10 and 50 di. exposure, one clearly finds the spectra to be a superposition of monolayer and multilayer contributions, which indicates Stranski Krastanov growth, as found for Ag(110). In the topmost multilayer spectra one can identify the position of the HOMO to be at 3.1 eV binding energy and use this to align the calculated DOS. This is shown at the top of the figure, which allows now to identify picene orbitals attributed to the multilayer. For instance this allows to identif HOMO -2, which is apparent as a weak shoulder at the leading edge of the Ag d-band at 3.8 eV.

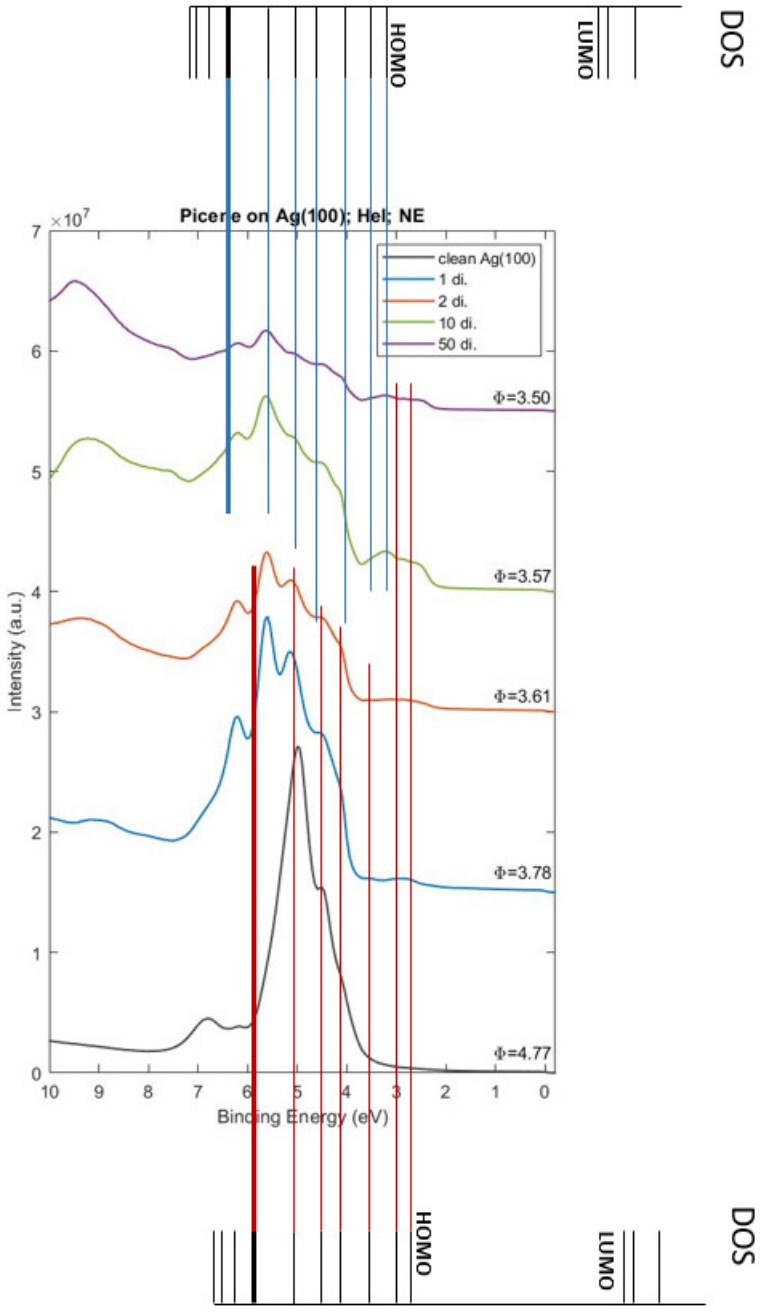

Figure 4.11.: HeI photoemission spectra in normal emission geometry of Picene on a Ag(100) substrate, shown as a function of coverage. The calculated DOS are shown to the bottom and top of the figure, with an alignment to the monolayer and multilayer, respectively.

In $NE + 20°$ fig. 4.12 the HeI satellite at 3.1 eV is more distinct and interferes slightly with the HOMO in the 1 di. film. Apart from this, the spectra are rather similar to the NE spectra, with only the leading orbitals of the 10 and 50 di. thick layers being more distinct.

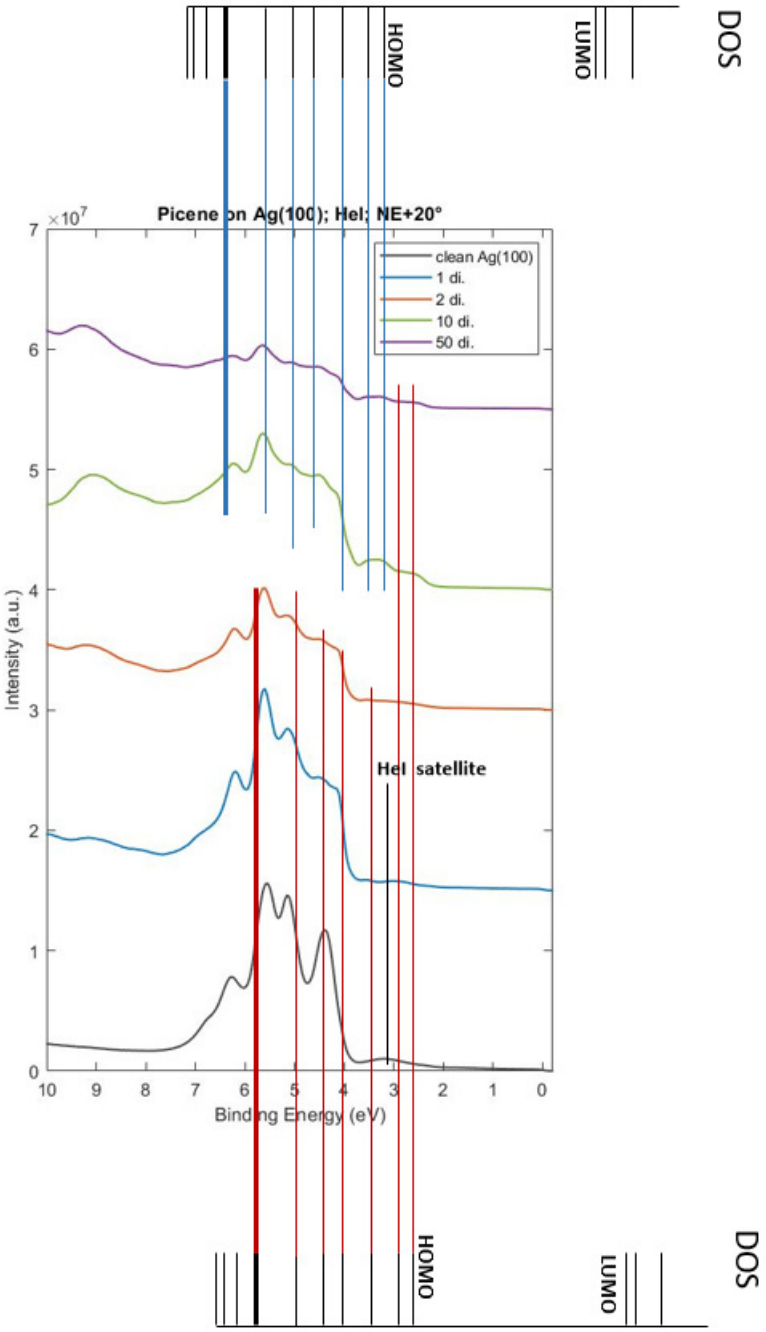

Figure 4.12.: HeI photoemission spectra in normal emission $NE + 20°$ geometry of picene on a Ag(100) substrate, shown as a function of coverage. The calculated DOS are shown to the bottom and top of the figure, with an alignment to the monolayer and multilayer, respectively.

Also in $NE + 40^{\circ}$ spectra of fig. 4.12 are rather similar to the experimental geometries discussed above and no strong angular dependencies are found. Again the HeI satellite is only weak at 2.20 eV and Filmdoes not interfere with the low exposures. It should be noted that the HOMO and/or HOMO-1 emission are most distinct in this geometry.

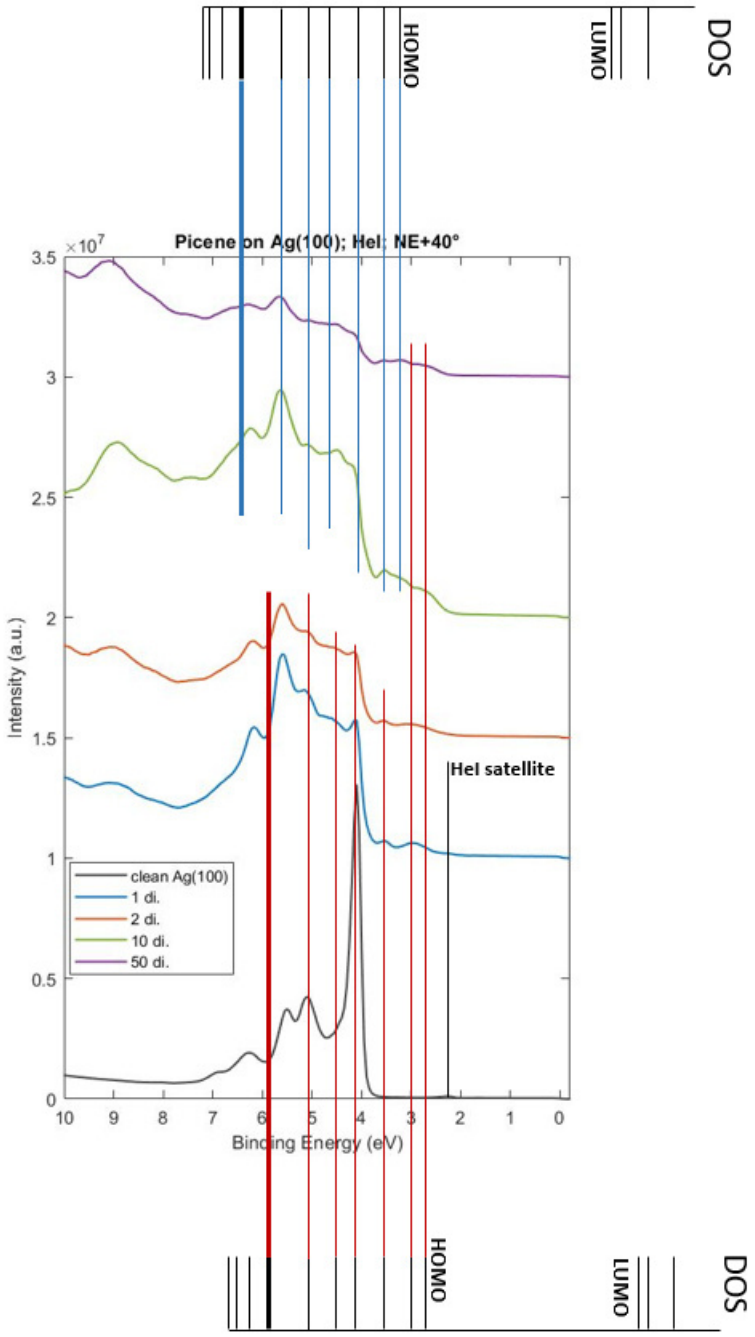

Figure 4.13.: HeI photoemission spectra in normal emission $NE + 40°$ geometry of picene on a Ag(100) substrate, shown as a function of coverage. The calculated DOS are shown to the bottom and top of the figure, with an alignment to the monolayer and multilayer, respectively.

Summarizing, the emissions in the EDC spectra for picene on Ag(100) perfectly obey the DOS based calculated values. The appearance of monolayer emissions in the high coverage films point in the direction of island growth. Due to only one azimuthal measurement orientation a statement about angular dependencies of the orbitals is not possible.

Our results agree with Huempfner et al., 2016 published based on his PES experiments for a monolayer picene on Ag(100), to be looked up in sec. 3.4. Furthermore, the Stranski Krastanov growth mode stated by Kelly et al., 2016 is supported by our experiments showing monolayer emissions shining through the multilayer EDCs. e.

4.3. Picene on Cu(110)

This chapter describes the electronic structure of various picene coverages on a Cu(110) surface, measured with He I ARUPS. The work functions for the individual picene films are listed in table 4.4 and displayed in fig. 4.14. From the saturation value of the work function reduction of about 3.75 eV the monolayer is defined to be at around 3 di coverage.

surface	work function
clean Cu(110) in Hölzl and Schulte, 1979.	$\Phi = 4.48$ eV
clean Cu(110) RT	$\Phi = 4.57$ eV
2 di. RT	$\Phi = 3.80$ eV
4 di. RT	$\Phi = 3.73$ eV
34 di. RT	$\Phi = 3.78$ eV

Table 4.4.: Work function change due to different layer thicknesses of Picene on Cu(110). As expected, for a monolayer of 2 di. the work function is higher than for multilayer of 4 di. and 34 di.

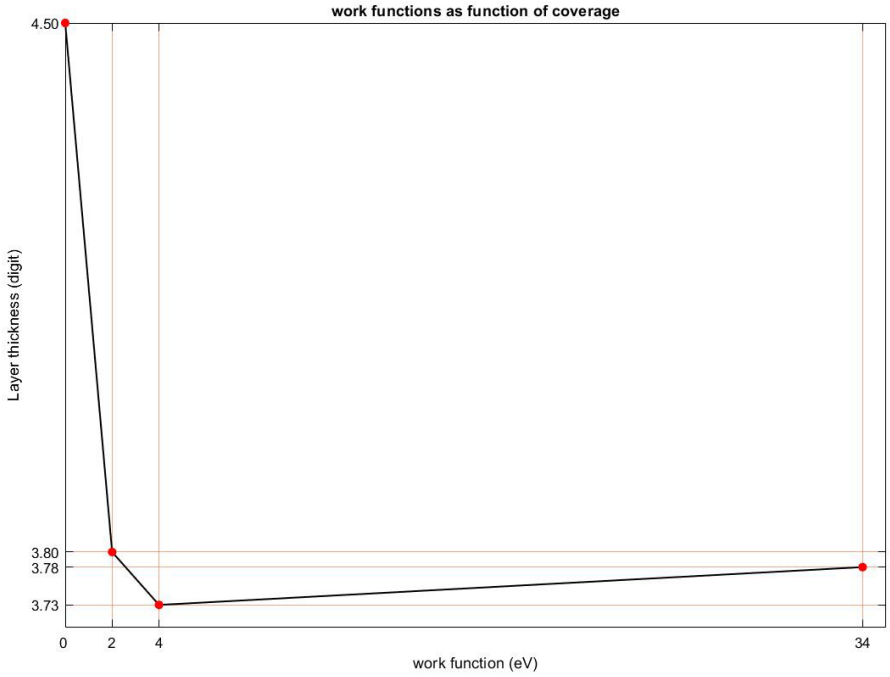

Figure 4.14.: Work function as function of coverage for Picene on Cu(110). The Φ value decreases with molecular layer thickness.

This monolayer work function (3.75 eV) was again used to determine the position of the HOMO in the monolayer by applying equation 2.10 (compare section 4.2). In table 4.5 the calculated values for the frontier orbitals are given together with the work function.

surface	Φ	**HOMO**	**HOMO-1**	**HOMO-2**
2 di. RT	$\Phi = 3.80$ eV	2.5 eV	2.8 eV	3.3 eV

Table 4.5.: Positions of the frontier orbitals in a mono as well as a multilayer picene on Cu(100) based on the Φ of the EDCs together with the DOS.

In fig. 4.15 to fig. 4.17 together with the respective Cu(110) substrate is measured with He I ARUPS for the three polar geometries NE, $NE + 20°$, as well

as $NE + 40°$. It should be noted that the azimuthal direction could not be determined due to a failure in the LEED, however, from the measurements in chapter 4.4 it is estimated that the azimuthal direction is close to [001]. In all three pictures the DOS of the monolayer at the bottom is aligned to the HOMO binding energy as given in tab. 4.5. The agreement for the 2 and 4 di exposures (both are near a monolayer) appears rather good as can be seen in Fig. 4.15 to Fig. 4.17. However, it should be noted that all frontier orbitals are buried in the Cu d-band (2 – 4 eV energy range), which makes them difficult to identify.

Considering now the 34 di. Nominal multilayer. The molecular features are more distinct and both the Cu d-band and the Fermi edge are reduced but still apparent. This again shows that the picene molecules have formed islands above a monolayer coverage, i.e. Stransky-Krastanov growth mode. The position of the HOMO (and other orbitals) of the molecular monolayer stays, but the position of the orbitals of the molecular multilayer islands is difficult to ascertain. It is suggested that the multilayer HOMO is at 3 eV binding energy, i.e. at 0.5 eV higher energy than for the monolayer, with the deeper orbitals at their corresponding positions.

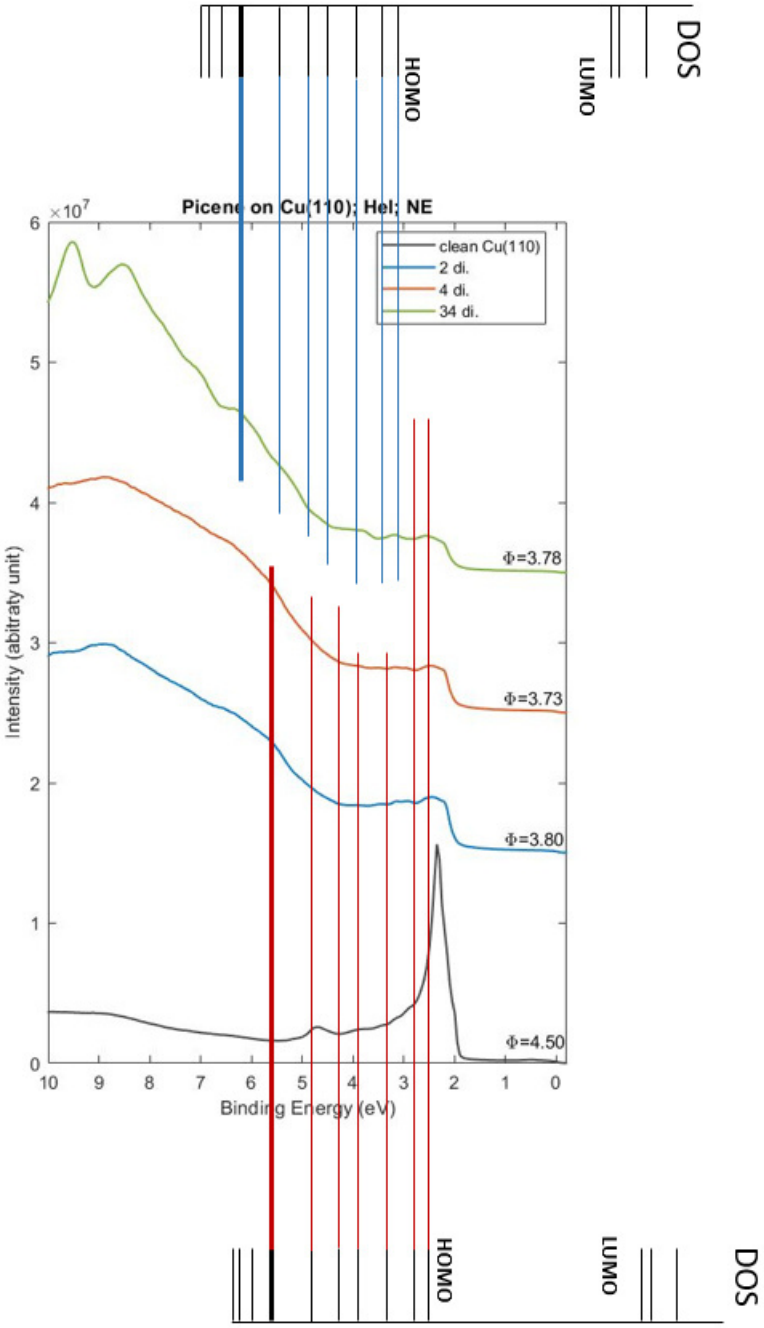

Figure 4.15.: HeI photoemission spectra in normal emission geometry of picene on a Cu(110) substrate, shown as a function of coverage. The calculated DOS are shown to the bottom and top of the figure, with an alignment to the monolayer and multilayer, respectively. The intensity of the substrate is diminished by a factor of 0.6.

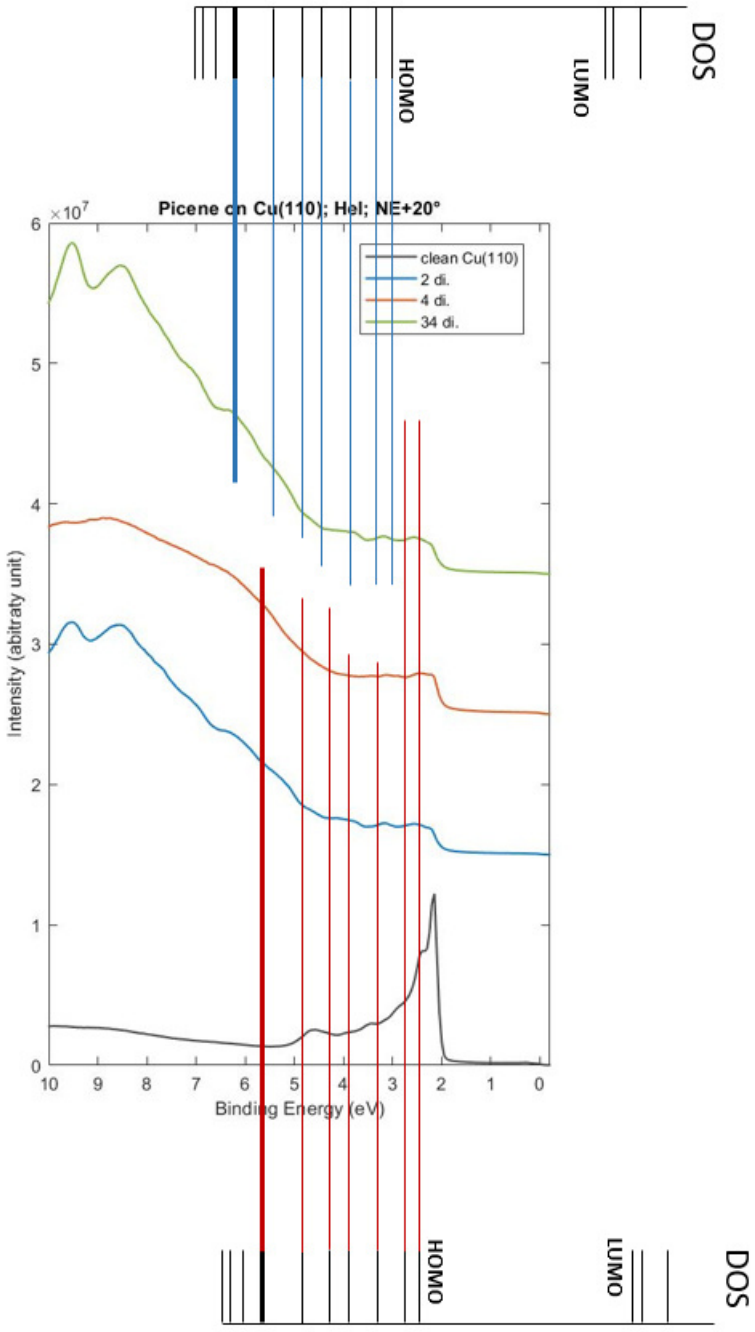

Figure 4.16.: HeI photoemission spectra in normal emission $NE + 20°$ geometry of picene on a Cu(110) substrate, shown as a function of coverage. The calculated DOS are shown to the bottom and top of the figure, with an alignment to the monolayer and multilayer, respectively. The intensity of the substrate is diminished by a factor of 0.6.

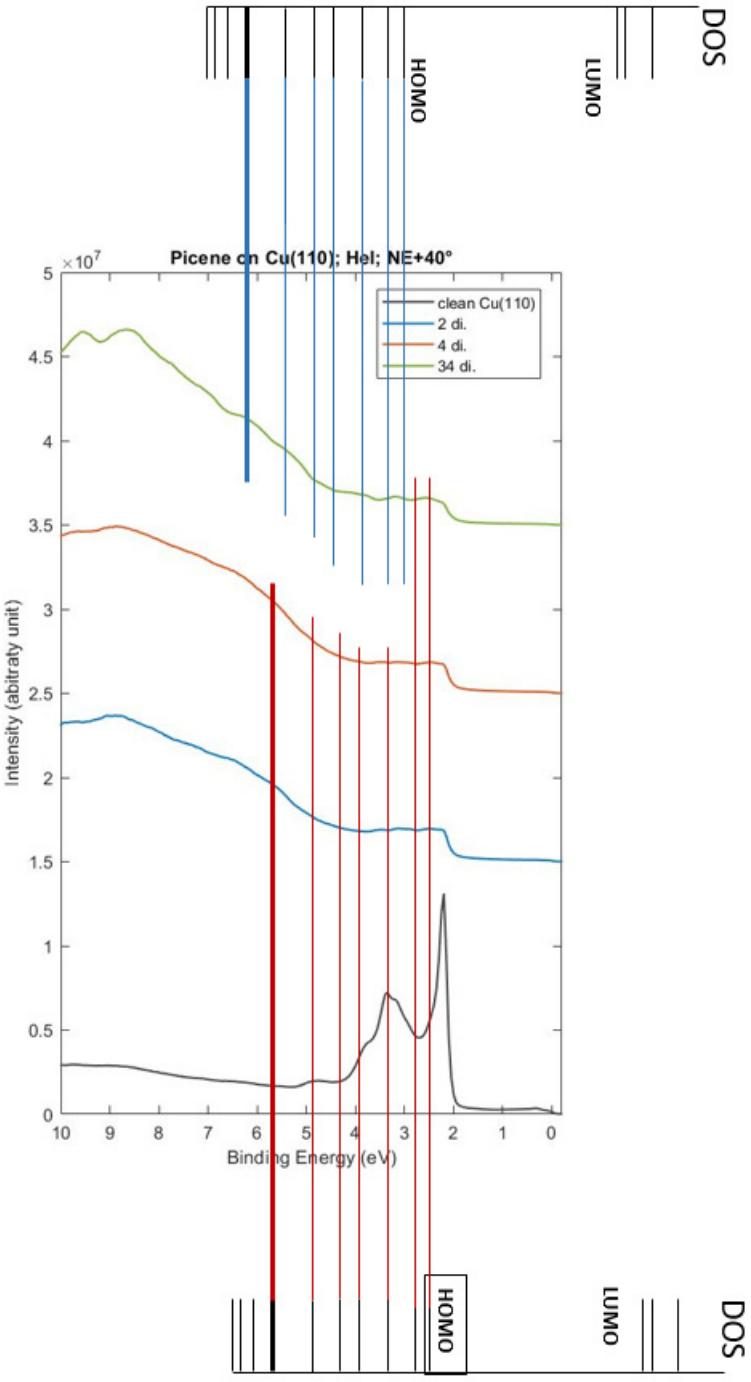

Figure 4.17.: HeI photoemission spectra in normal emission $NE + 40°$ geometry of picene on a Cu(110) substrate, shown as a function of coverage. The calculated DOS are shown to the bottom and top of the figure, with an alignment to the monolayer and multilayer, respectively. The intensity of the substrate is diminished by a factor of 0.8.

In fig. 4.18, a Al K_{alpha} XPS survey spectra of clean and picene exposed Al K_{alpha} XPS ssurvey spectra of clean and picene exposed Cu(110) surfaces are shown. Concentrating on C1s we find that the carbon amount on the surface increases higher with Picene coverage. Concomitant with picene exposure the intensity of the Copper substrate peaks reduces.

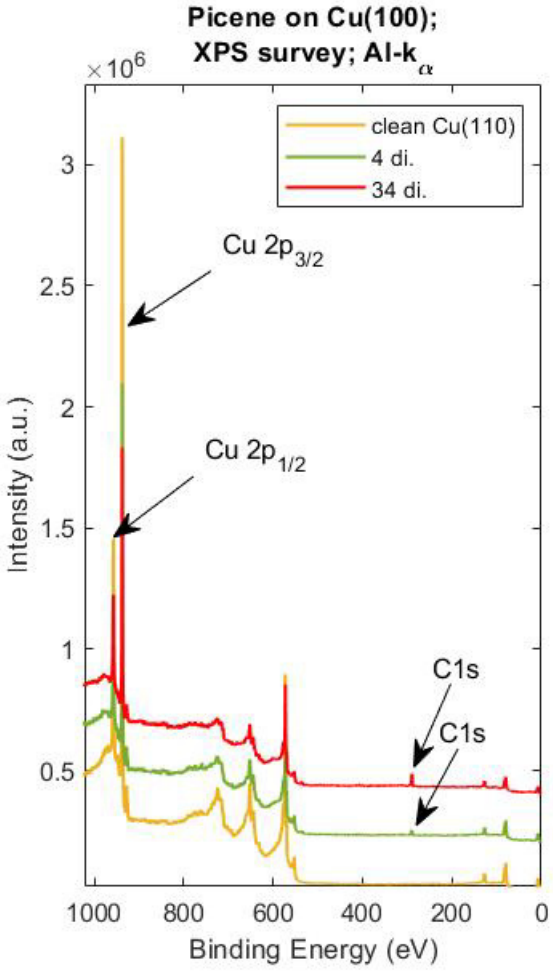

Figure 4.18.: XPS Al K_α survey.

Our results agree with the work of Q. Wang et al., 2017, with the picene HOMo and HOMO-1 emissions of the EDC spectra being burried in the Cu

3d-band for the thin films measured here.

4.4. Cu-p(2x1)O

In this part the electronic structure of picene films on Cu-p(2x1)O laid at room temperature is investigated. Electronically the oxygen exposure passivates the Cu(110) surface and causes a rise of the work function. Tab. 4.6 contains the values for this Cu-p(2x1)O surface in dependency of the Picene coverage. In contrast to the silver surfaces the work function reaches its minimum at 4 dig. of exposure or even beyond, rather than 2 dig.. This later saturation of the work function may hint at a different growth type to the clean metal substrates.

surface	**work function**
clean Cu-p(2x1)O RT	$\Phi = 4.97$ eV
2 di. RT	$\Phi = 4.55$ eV
4 di. RT	$\Phi = 4.49$ eV
34 di. RT	$\Phi = 4.41$ eV

Table 4.6.: The work function change with increasing of Picene coverage on Cu-p(2x1)O to lower values.

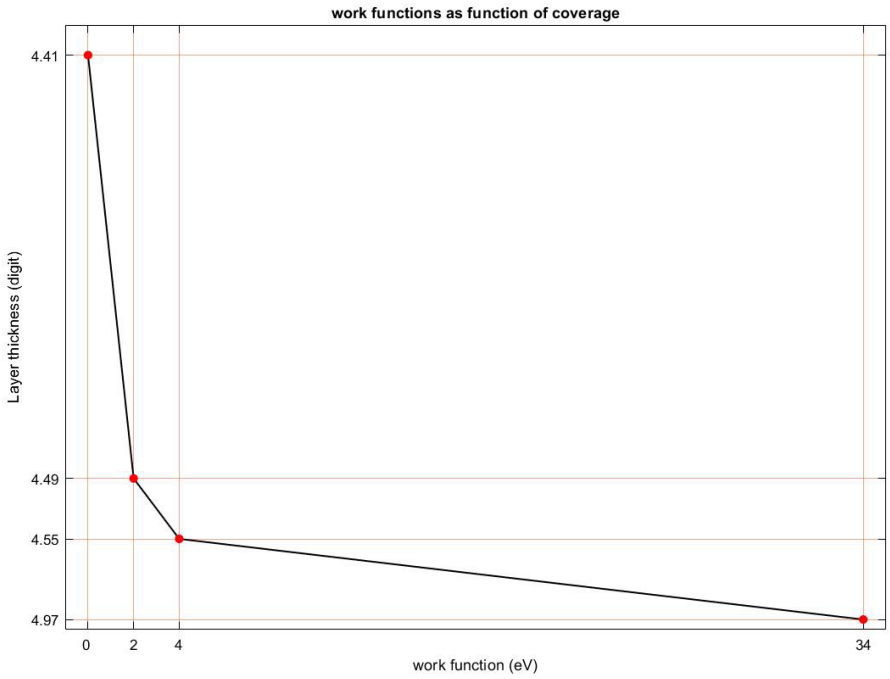

Figure 4.19.: The work function as a function of coverage on a Cu-p(2x1)O surface.

In fig. 4.20 to fig. 4.24 He I photoemission spectra, recorded in the three polar angles NE, $NE + 20°$ beside $NE + 40°$ are shown. The azimuthal direction is estimated to be near [001]. From dispersion of the O_2p features in the clean substrate spectra at the bottom of the above figures. The estimated position for the O_2p bonding orbitals are NE: 5.8 eV, NE+20: 6 eV and NE+40: 6.3 eV, while the O2p antibonding orbitals are at NE: 1,8 eV, NE+20: 1,6 eV and NE+40: 1,3 eV.

Considering the 34 dig. spectra in fig. 4.20 to fig. 4.24 we notice a distinct Fermi-edge and indications of the Cu d-band suggesting a non complete coverage of the film, compatible with Stranski Krastanov growth. The leading maximum at 2.3 eV is thought to consist of HOMO and HOMO-1 orbitals, with the HOMO at 2.15 eV and HOMO-1 at 2.45 eV. This was used as an

anchor point to the calculated DOS (top of figure). On the other hand this peak displays a distinct shoulder at 1.7 eV, which is attributed to the HOMO and HOMO-1 of the monolayer. Thus we align the monolayer HOMO to 1.55 eV and use this to position the calculated DOS (bottom of figure). Again the monolayer and multilayer are separated by about 0.5 eV, comparable to the other substrates. From the work function but also the appearance of the coverage dependent photoemission spectra it is suggested that 4 dig. rather than 2 dig. constitute a monolayer. This is in contrast to the clean metal substrates. A possible explanation will be that on the metals the first layer absorbs planar, whereas for the oxygen reconstructed copper surface the picene molecules arrange themselves in a tilted, edge on geometry along the Cu-O rows. This would lead to a higher molecular density within the layers and will thus require a higher exposure to fill one layer. It should be noted that such an alignment has been observed for several chainlike molecules before (Koller, Berkebile, et al., 2007, Oehzelt et al., 2007).

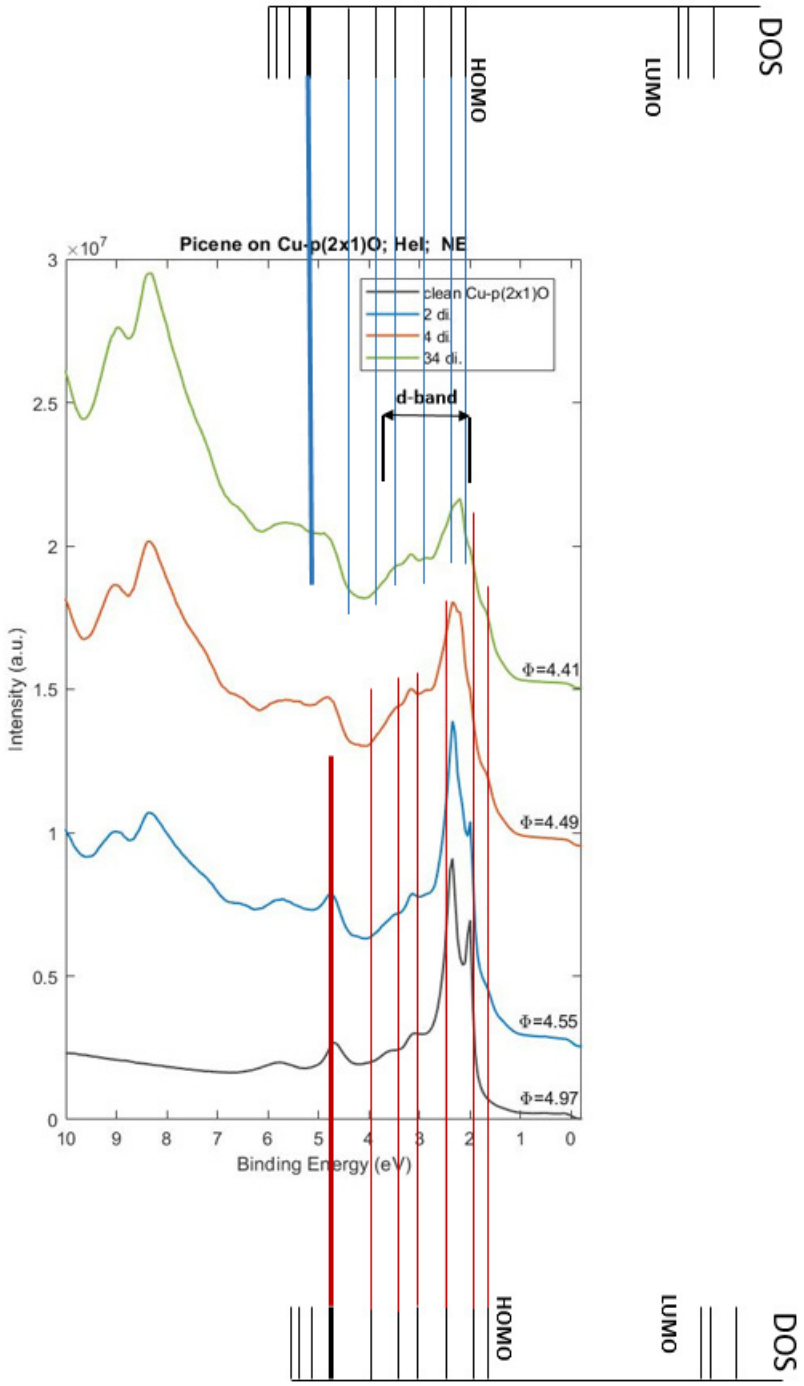

Figure 4.20.: Dosing series on Cu-p(2x1)O including the substrate in NE aligned with the DOS to the monolayer (4 di.. The Intensities of the clean Cu-p(2x19O surface are diminished by a factor of 0.5.

For $NE + 20°$ in fig. 4.22 the situation looks similar to NE. In the monolayer the HOMO's peak at 1.7 eV clearly emerges and serves as anchor for the DOS at the bottom. The HOMO-1 is found at 2.20 eV, shifted to a higher binding energy for 0.2 eV.
In the multilayer the HOMO peak of the monolayer clearly shows up at 1.7 eV. The peak at 2.20 eV is assigned to the HOMO-1. This again leads to a close arrangement of the particular DOS addressed the thin and the thick Picene film.

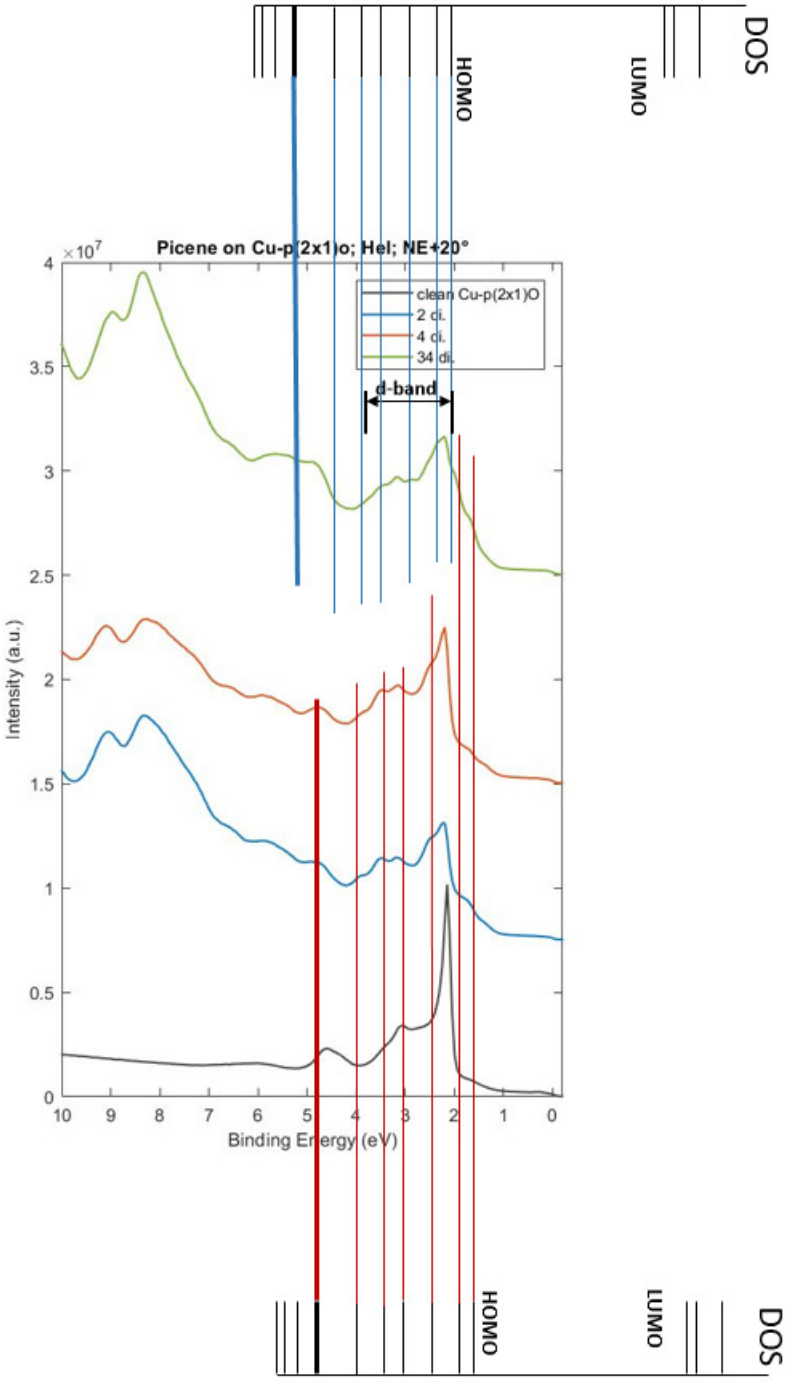

Figure 4.21.: Dosing series on Cu-p(2x1)O including the substrate in $NE + 20°$. The Intensities of the clean Cu-p(2x19O surface are diminished by a factor of 0.5.

In $NE + 40°$ pictured in fig. 4.22 the sp-band at 1.35 eV is most distinct, even in the high coverage.

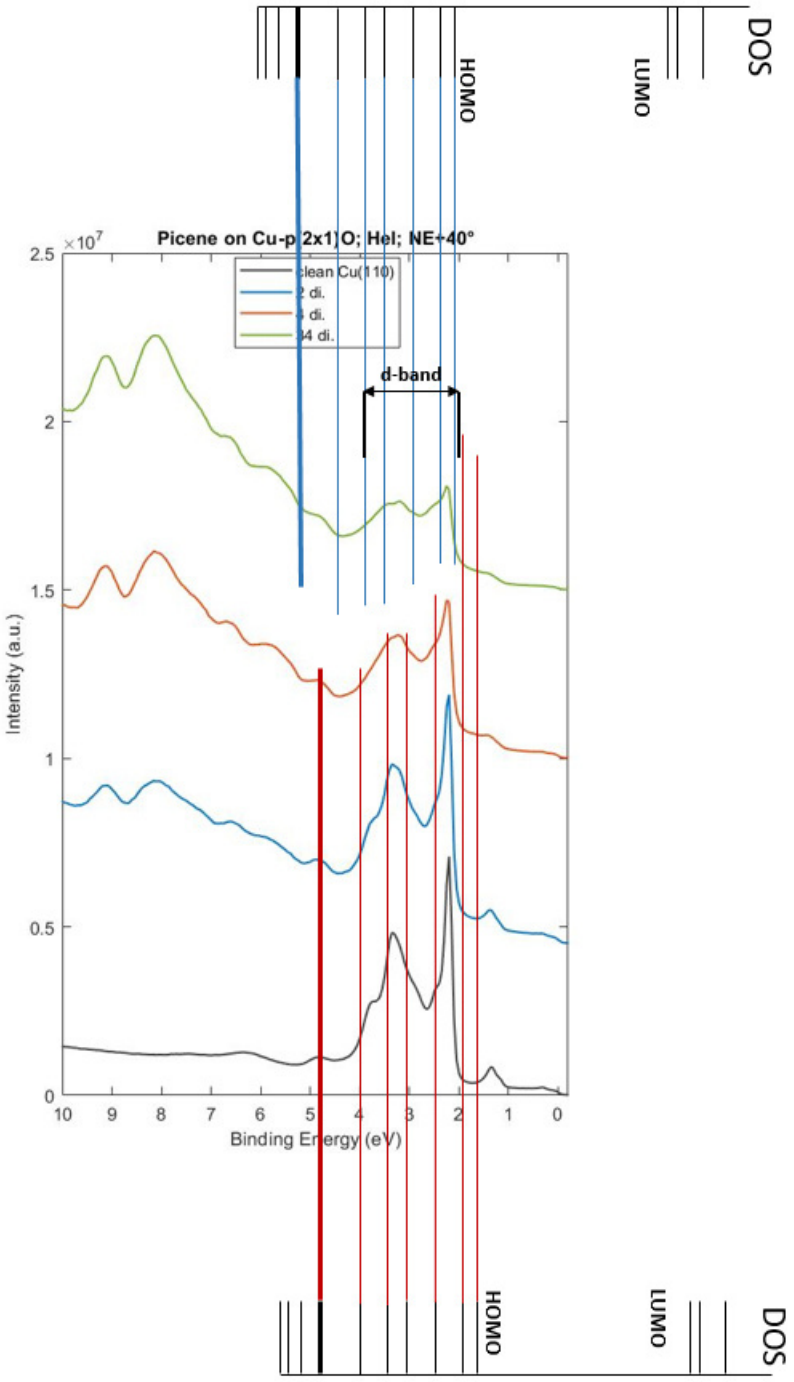

Figure 4.22.: Dosing series on Cu-p(2x1)O including the substrate in $NE + 40°$. The Intensities of the clean Cu-p(2x19O surface are diminished by a factor of 0.5.

To get an insight for a possible angular dependency of the orbitals in the picene low coverage regime, in addition, two more azimuth configurations with $\pm 45^{\circ}$ off the default one were investigated in fig. 4.23 to fig. 4.25. The alignment of the orbitals is taken from the previous section. Comparing the azimuthal directions, on finds the differences mainly in substrate, i.e. the O_2p orbitals and the copper d-band. The orbital emission are to weak and hidden in the d-band for a clear assessment, however in all cases it appears that the molecular orbitals are more pronounced at higher polar take off-angles.

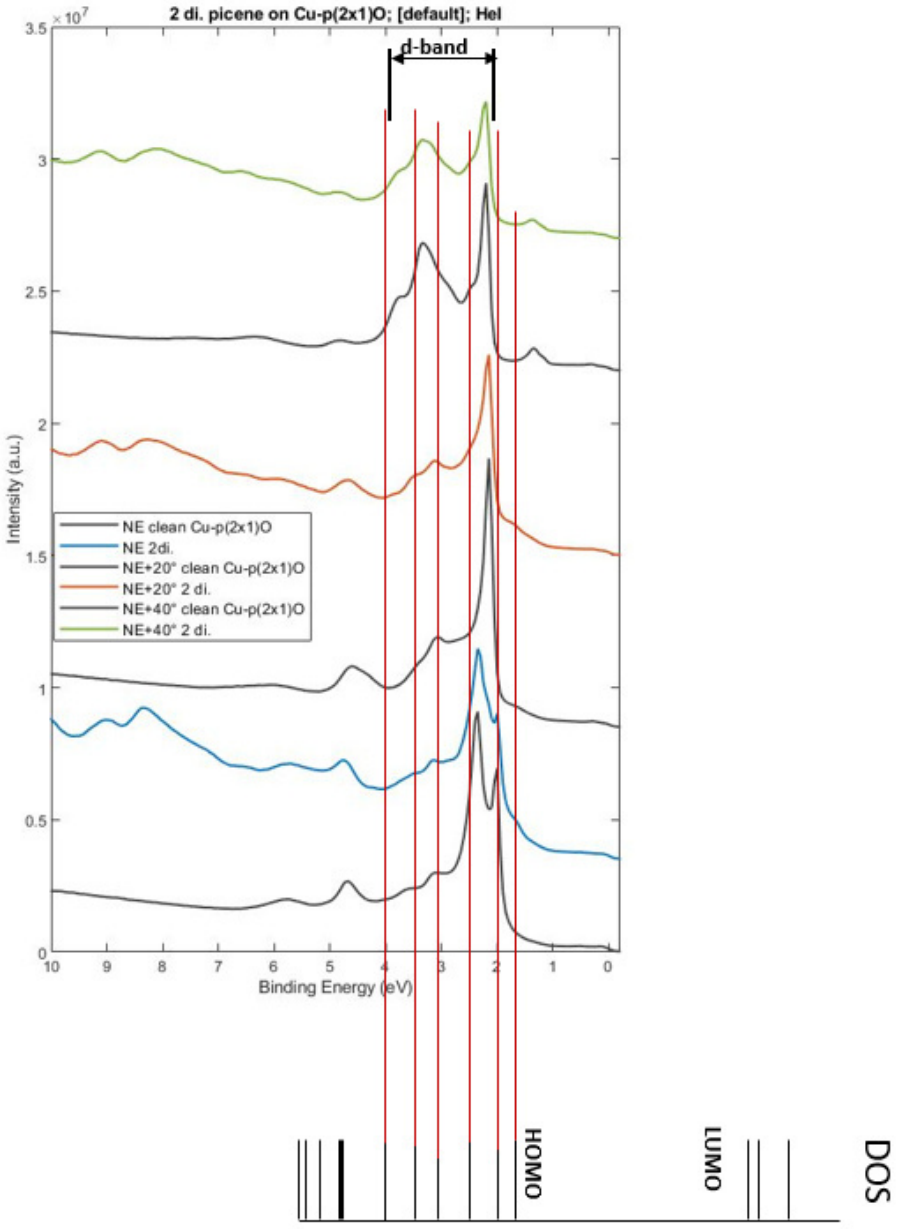

Figure 4.23.: He I ARUPS spectra in the default azimuth for half a monolayer picene on Cu-p(2x1)O measurements are displayed together with their respective substrate emission underneath. The intensities of the clean substrate is diminished by a factor of 0.5 and the one for the monolayer by diminished by a factor of 0.7

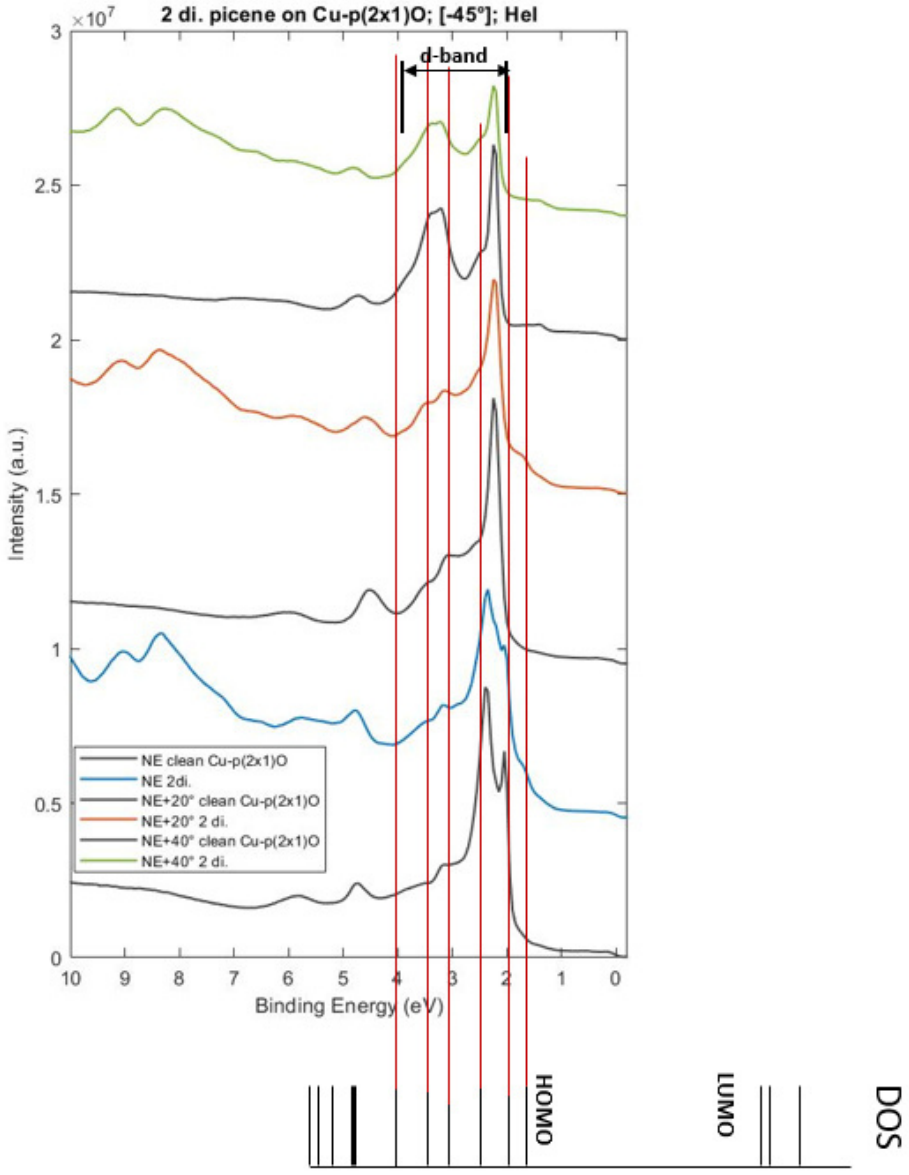

Figure 4.24.: He I ARUPS spectra in an anzimuthal direction of $[NE - 45°]$off the default adjustment for half a monolayer picene on Cu-p(2x1)O are displayed together with their respective substrate emission underneath. The intensities of the clean substrate is diminished by a factor of 0.5 and the one for the monolayer by diminished by a factor of 0.7 .

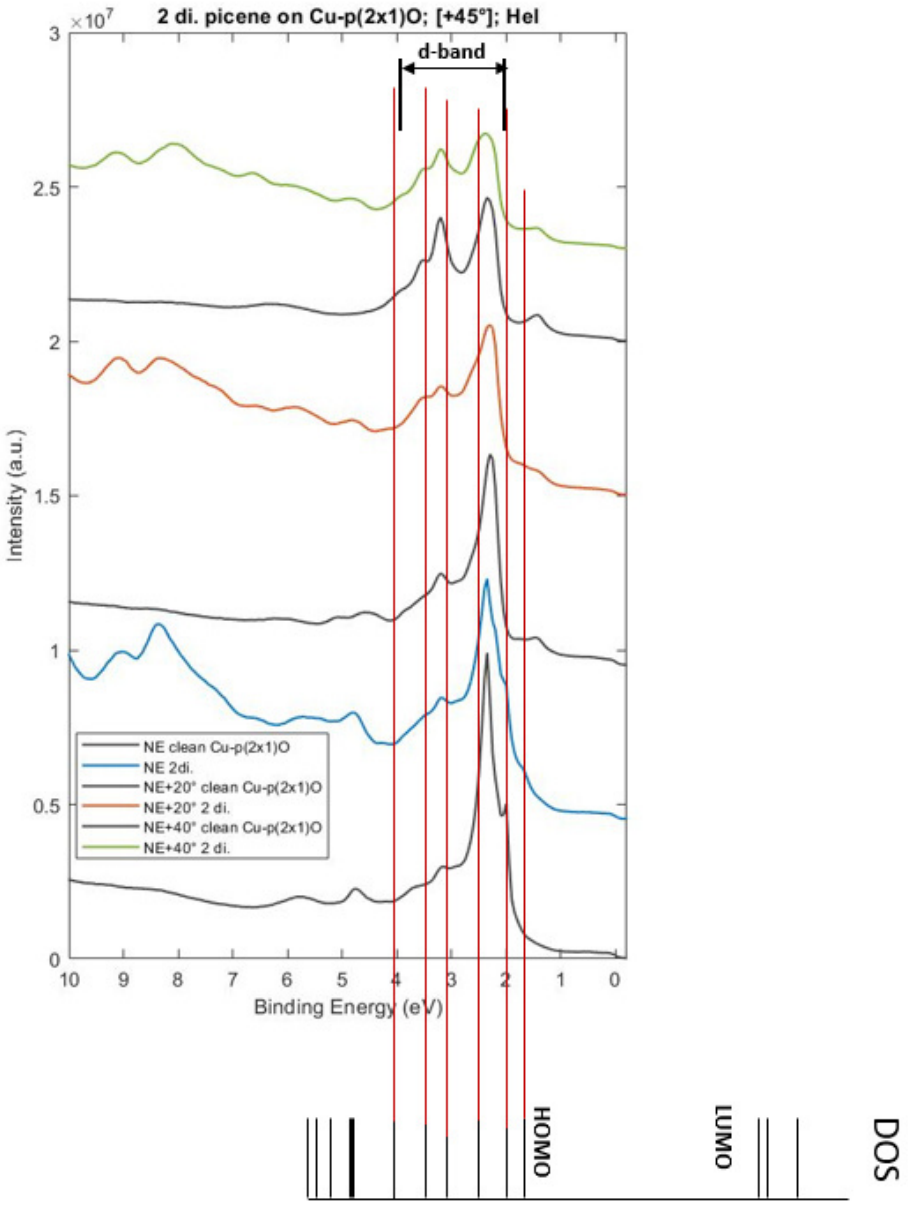

Figure 4.25.: He I ARUPS spectra in an anzimuthal direction of $[NE + 45°]$ off the default adjustment for half a monolayer picene on Cu-p(2x1)O are displayed together with their respective substrate emission underneath. The intensities of the clean substrate is diminished by a factor of 0.5 and the one for the monolayer by diminished by a factor of 0.7

5. Scienta SES - 200 spectrometer system

The UPS and XPS data acquisition takes place in the Scienta SES 200 spectrometer system (Koller, 2002).

The preparation chamber provides the possibilities for sample cleaning and surface preparation by evaporating molecules. The transfer of a single crystal to the analyzer compartment carries out an OMNIAX 600 manipulator, with an in-house devised as well as crafted sample holder. The component is capable of azimuthal rotation accompanied by the variation of the temperature range of the sample due to heating to 1500 K or cooling down to 90° K using liquid nitrogen. The main spectrometer chamber bears the plugins for the He-discharge lamp (VG HI 191), the X-ray source (VG XR 3, double anode Mg \Al) along with an optional electron gun (Staib) and the exit to the detection unit. An ion pump combined with a titanium sublimation pump (TSP) hold the base pressure at about $1 \cdot 10^{-10}$mbar.

The hemispherical electron analyzer Scienta SES-200 exhibits a high position sensitivity. The intersection with the chamber and the port, are aligned in a manner that the incoming light and the detector share the same plane. Furthermore the angle between the detector and the port encloses 47°.

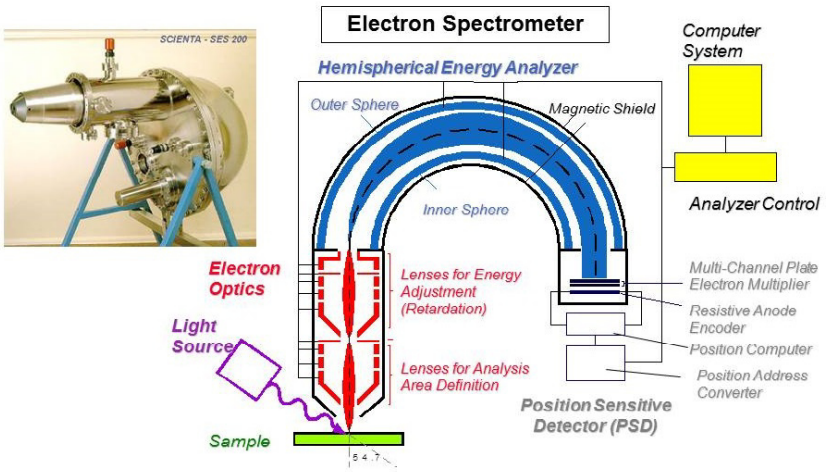

Figure 5.1.: Scienta SE 200 system with the optical path for the detected electrons.

5.1. Calibration

The XPS as well as the UPS light source together with the detector are built-in on their places and are in a triangular constellation with the sample. Figure 5.2 sketches the beam path for the UPS-discharge lamp.

To collect data from different polar angles for the momentum maps, the sample rotates, which causes a changing of the incoming light's shape on the surface from a cycle to an ellipse (fig.5.2), but it also changes polarization of the light. In addition, the sample can already be seen as part of the detectors photoelectron imaging system, which may be affected by the sample rotation, required in looking at different electron take off angles.

In the following it is tried to evaluate this angular dependencies for the variousexperimental settings and possibly to suggest a procedure for an angular calibration of the photoemission spectra

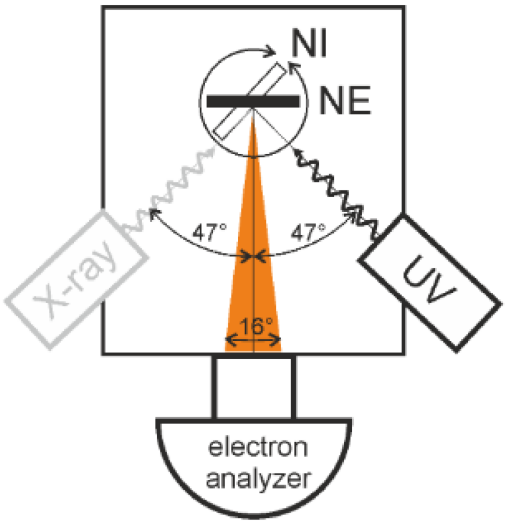

Figure 5.2.: Measurement geometry of the Scienta SES 200 analyser by Reinisch, 2015.

5.1.1. Parameters for calibration setup

The detection system works in two selectable modes, an angular beside a spatial one, illustrated in fig. 5.3. Additionally, the detector offers several energies for the electrons. While, both the detection modes and the various pass energies have to be accounted for with the UPS-HeI, UPS-HeII and the XPS light source, we will focus on the standard He I set up and a pass energy of 10 eV.

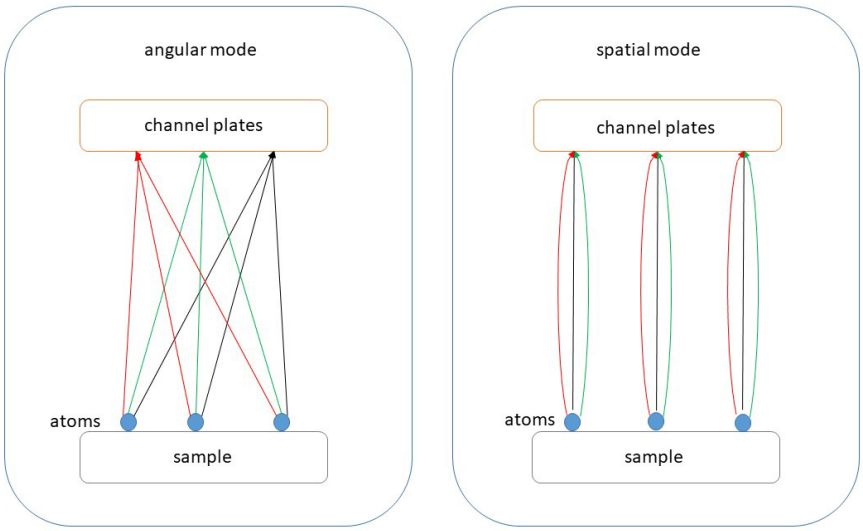

Figure 5.3.: The two detecting modes.

5.1.2. Normalization

Possible normalization procedures to account for the different photoelectron emission angles would be (a) normalization to the Fermi-edge height, (b) the area of excitation and (c) the dark counts.

(a) Normalization to the Fermi edge height was dismissed for the low count rate and because its is not free from angle dependent electronic states.

(b) The area of excitation (a.o.e) is a possibility and resembles accounts for the region on the sample on which the light incidences. Therefore the raw data is normalized by $\cos(47 \pm \Theta)$. $\cos(47°)$ is the position sample to port. The specific polar angle for the measurement if positive has to be included as subtraction and the other way round.

(c) The dark ground (d.g.) includes the area in which no intensity is expected, beyond the Fermi-edge. Therefore the raw data is scaled by the

energy of $E_{Fermi} + 1$ eV to $E_{Fermi} + 3$ eV.

5.1.3. Graphite for calibration

Graphite is assumed to possess no oriented particles as paste, and thus emits isotropically in all directions. This makes it the perfect candidate to perform HeI HeII, XPS calibration measurements to get a hind of the angular relation to the intensity. Of course there are electronic states, as Zhou, Gweon, and Lanzara, 2006 reports from localized states in graphite with nondisperse nature at binding energies 2.9 eV, 4.3 eV and 7.8 eV in the EDCs.
It is thinkable that a graphite paste despite its obiviously disarrayed structure still may include some order, which would then lead to some angular effects in the polar emissions. A possible reason for such a preferred alignment may arise in the production of the 'isotrop' carbon layer, which is painted on a sample plate and by the paint brush particles may be preferentially aligned.

5.2. Calibration data analysis

In order to get a calibration we measured the graphite sample for different modes, pass angles and photon sources as shown in the tables 5.1 to 5.3.

Detection mode	Pass energy (eV)	Polar angles (°)	Steps (°)	Data files .txt
angular mode	5 eV	$-30°$ to $+60°$	2	SPE0090_02 to SPE0138_02
angular mode	10 eV	$-30°$ to $+60°$	2	SPE0161_02 to SPE0211_02
spatial mode	2 eV	$-25°$ to $+60°$	25	SPE0040_02 to SPE0064_02
spatial mode	5 eV	$-25°$ to $+60°$	25	SPE0040_02 to SPE0064_02
spatial mode	10 eV	$-25°$ to $+60°$	25	SPE0040_02 to SPE0064_02
spatial mode	20 eV	$-25°$ to $+60°$	25	SPE0040_02 to SPE0064_02

Table 5.1.: List of the calibration measurement series for HeI photoemission spectra in the energy range $E_{kin} = 0 - 20$ eV.

Detection mode	Pass energy (eV)	Polar angles (°)	Steps (°)	Data files .txt
angular mode	5 eV	$-25°$ to $+55°$	5	SPE0142_20 to SPE0158_20
angular mode	5 eV	$-25°$ to $+55°$	5	SPE0248_20 to SPE0264_20
angular mode	10 eV	$-25°$ to $+55°$	10	SPE0265_20 to SPE0272_20
angular mode	20 eV	$-25°$ to $+55°$	5	SPE0213_20 to SPE0229_20
angular mode	50 eV	$-25°$ to $+55°$	5	SPE0230_20 to SPE0246_20
spatial mode	20 eV	$-25°$ to $+55°$	25	SPE0074_20 to SPE0079_20

Table 5.2.: List of the calibration measurement series for HeII photoemission spectra in the energy range $E_{kin} = 25 - 40$ eV. Only in the thired row the energy range is extended to $E_{kin} = 0 - 40$ eV

Detection mode	Pass energy (eV)	Polar angles (°)	Steps (°)	Data files .txt
angular mode	10 eV	$-30°$ to $+60°$	5	SPE0289_02 to SPE0307_02
angular mode	10 eV	$-25°$ to $+55°$	25	SPE0311_02 to SPE0314_02
spatial mode	10 eV	$-25°$ to $+50°$	25	SPE0312_02 to SPE0314_02
spatial mode	10 eV	NE	0	SPE0324_02
spatial mode	20 eV	NE	0	SPE0321_02
spatial mode	100 eV	NE	0	SPE0316_02
spatial mode	200 eV	NE	0	SPE0322_02

Table 5.3.: List of the calibration measurement series for Mg K_α XPS spectra in the energy range of the Fermi-edge (rows 2 and 3), at the 1Cs peak (rows 4 to 7) and the He I range (row 1).

In this chapter the analysing of the data is shown on the example of He I ARUPS measurements in angular mode with pass energy 10eV, as this parameters are used for the UPS measurements in this thesis.

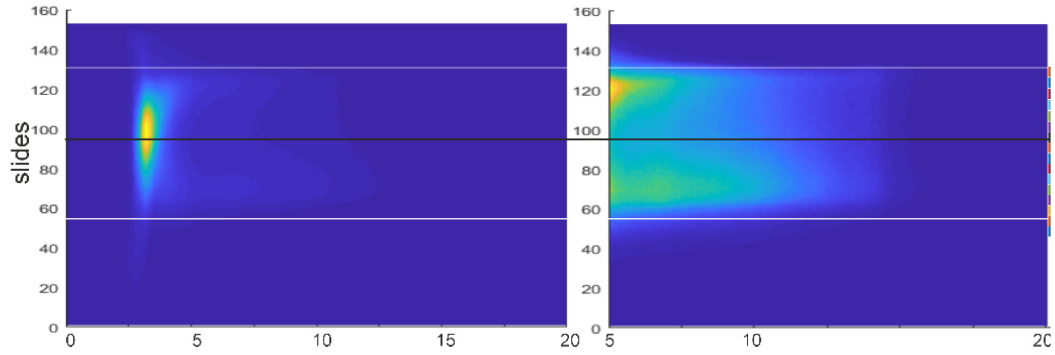

Figure 5.4.: Rawdata for normal emission (NE) geometry with He1 PE10 in angular mode.

Figure 5.4 shows the image of the measurement for the NE geometry, measured for kinetic energy from 0 to 20 eV. For this measurement the slides represent the angle distribution. The region marked with the white lines are 16° of the measurement, which is the angular acceptance of the detector. For the UPS spectra one integrates over slides.

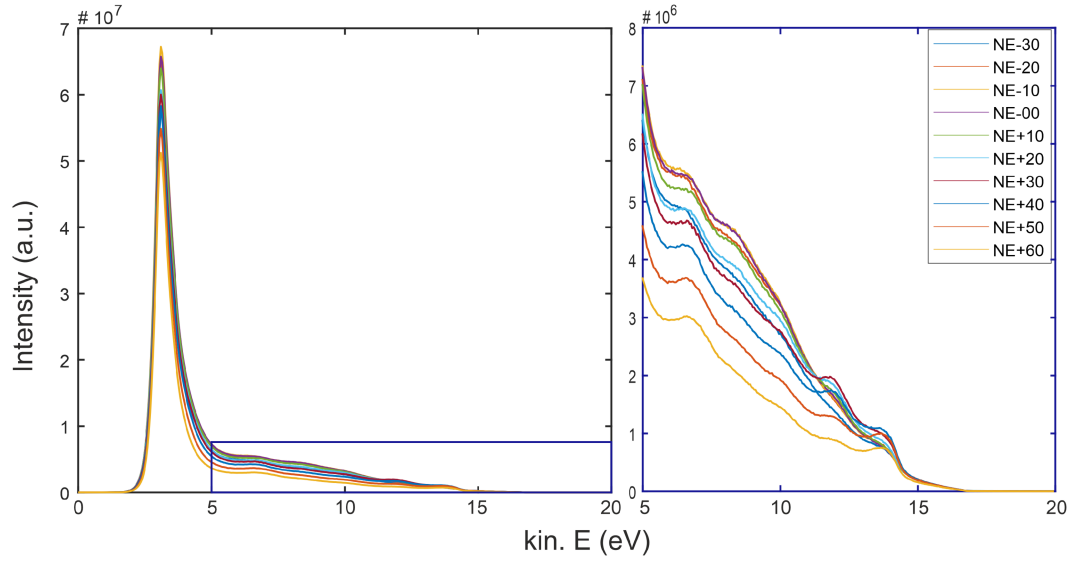

Figure 5.5.: Integrated Intensity over all slides for different take-off angle θ

In figure 5.5 the UPS spectra are shown for the different measurements

from $NE - 30°$ to $NE + 60°$, integrated over all slides (also the dark count slides). From the figure 5.5 we see that the intensity of the measurements is depending on the kinetic energy we measure as well from the takeoff angle. In literature different normations are suggested as for example with the area of the light, as spot of the light on the sample changes with the rotation of it. So the area of the spot gets from an circle at the normal incidence to the light, which is 47° of the normal emission to the detector were the spot is an ellipse (fig. 5.2). In the following figure 5.6 show the same measurements as figure 5.5 but now only the 3 slides in the middle of the measurements are taken.

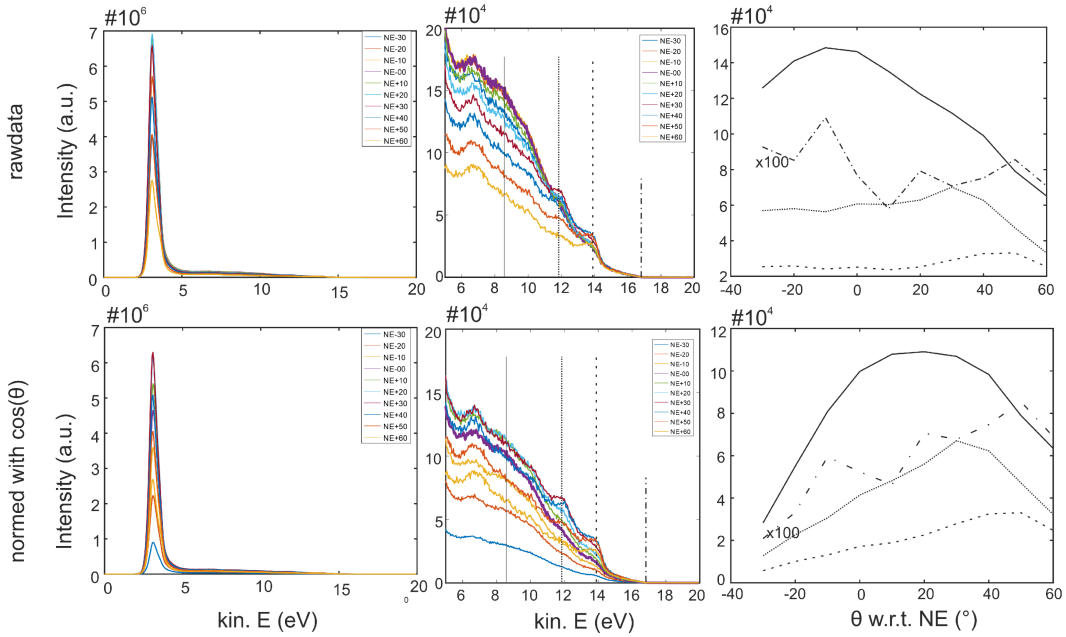

Figure 5.6.: HeI photoemission EDC spetra of graphite in angular mode with pass energy 10 eV and the energy range of $0 - 20$ eV.
Pictures on the top line: Left) EDC spectra of the raw data. Middle) the raw data without the secondary electron peak. The black lines mark arbitrary chosen kinetic energies to investigate the progress of the intensity dependend on the emission angle. Right) The intensity progress in dependence of the emission angles at 4 different kinetic energies.
Images on the bottom line: Left) EDC spectra of the raw data normalized to the area of excitation. Middle) the raw data normalized to the area of excitation without the secondary electron peak. The black lines mark arbitrary chosen kinetic energies to investigate the progress of the intensity dependend on the emission angle. Right) The intensity progress in dependence of the emission angles at 4 different kinetic energies.

Fig. 5.6 expresses a comparison of the normalzed data to the raw data, focusing on the angular dependendy of the intensity at 4 arbitrary chosen kinetic energies. The right pitures on the top and the bottom show the same for both data sets. Around NE (0°) nearly all 4 curves have a constant and linear section concerning the intensity. At low angles for all 4 graphs the intensity is at lowest and at highest around $NE + 30\circ$ to $NE + 40\circ$ bevore decending again towards $NE + 60\circ$.

It is a good start for the normalitions but it is not a complete solution as also the intensity distribution over the channelplates have to be taken in account. As for that we looked at the geometries NE, $NE - 30°$, $NE + 30°$ and $NE + 50°$ a bit closer at the different slides as shown in figure 5.7 to 5.10.

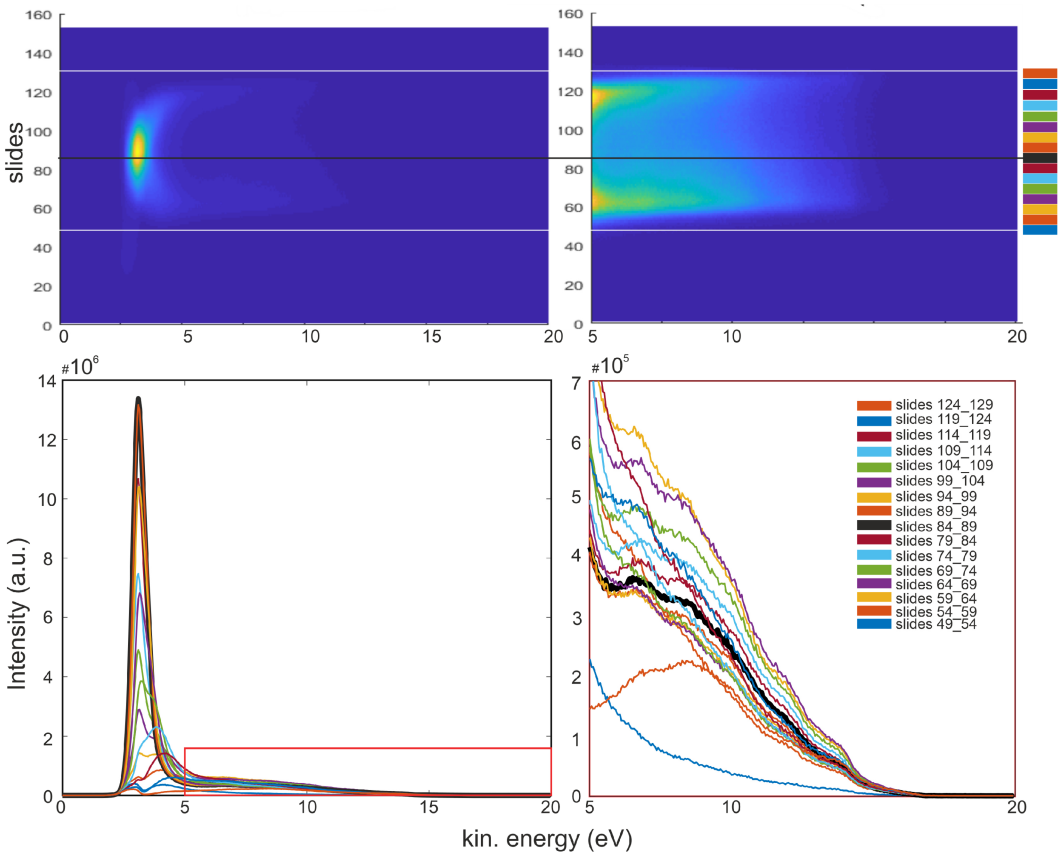

Figure 5.7.: Rawdata for normal emission (NE) geometry with He1 PE10 in angular mode. On the right side the full measurement data as image, with the labeled intensity region of interest and as EDC spectra bearing a prominent secondary electron peak. On the right side The secondary electrons are cut out, only the graphite intensities remain. The image is sliced into regions of 5 slides each, which are plotted as EDC spectra beneath.

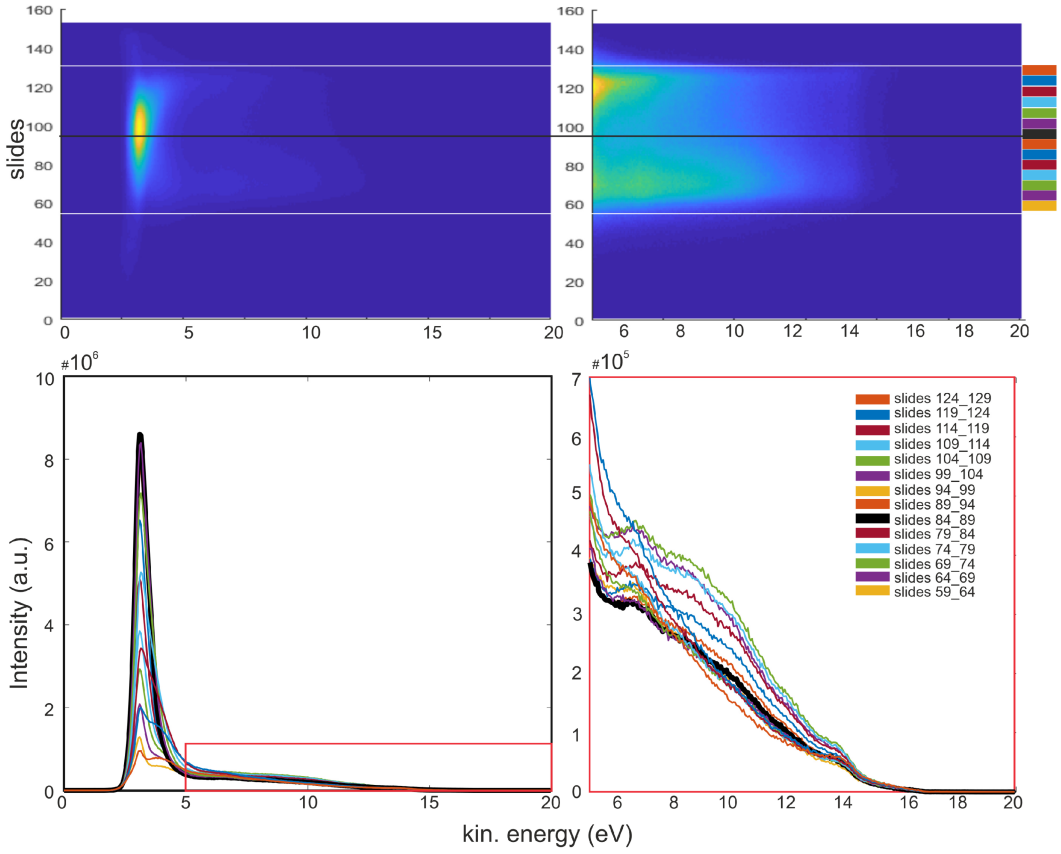

Figure 5.8.: Rawdata for $NE - 30°$ geometry with He1 PE10 in angular mode. On the right side the full measurement data as image, with the labeled intensity region of interest and as EDC spectra bearing a prominent secondary electron peak. On the right side The secondary electrons are cut out, only the graphite intensities remain. The image is sliced into regions of 5 slides each, which are plotted as EDC spectra beneath.

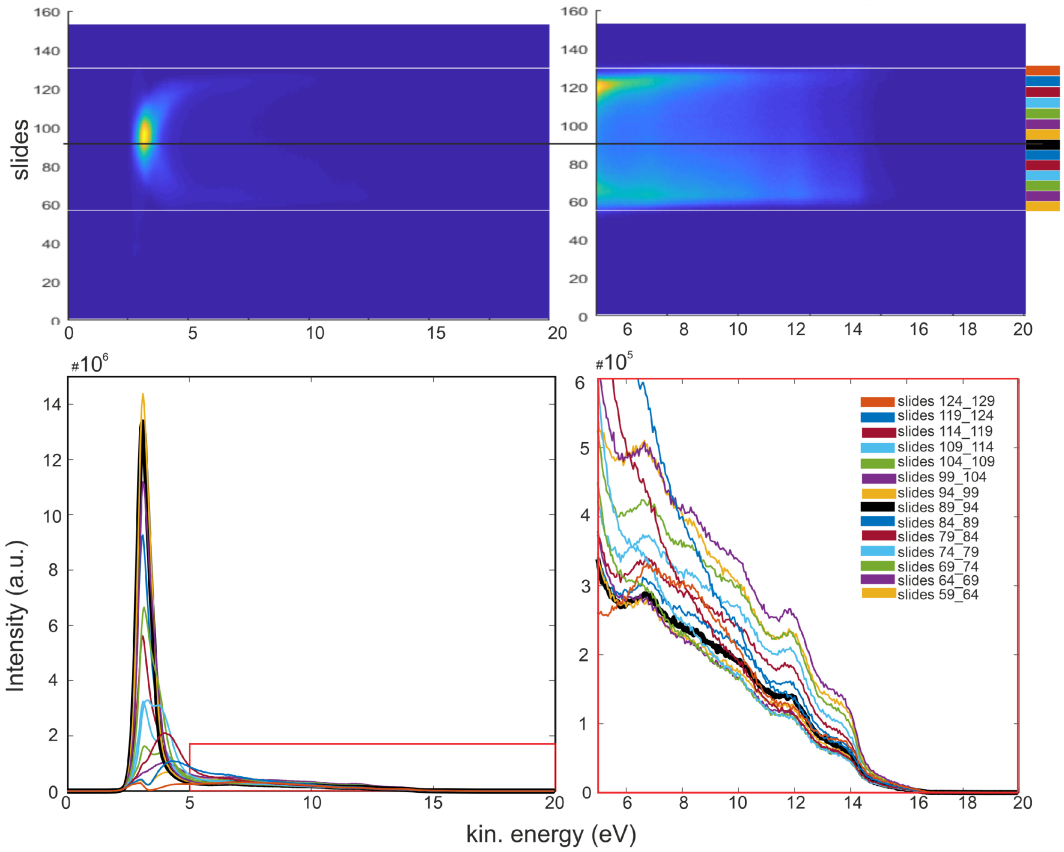

Figure 5.9.: Rawdata for $NE + 30°$ geometry with He1 PE10 in angular mode. On the right side the full measurement data as image, with the labeled intensity region of interest and as EDC spectra bearing a prominent secondary electron peak. On the right side The secondary electrons are cut out, only the graphite intensities remain. The image is sliced into regions of 5 slides each, which are plotted as EDC spectra beneath.

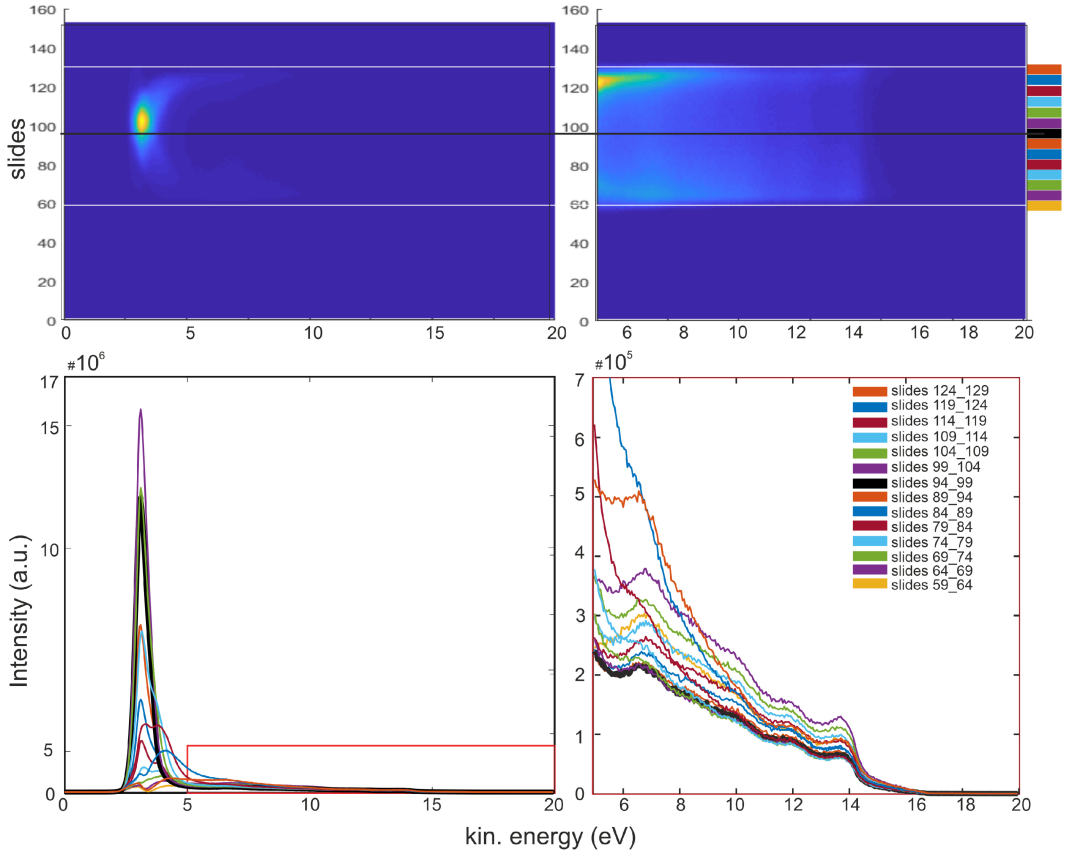

Figure 5.10.: Rawdata for $NE + 50°$ geometry with He1 PE10 in angular mode. On the right side the full measurement data as image, with the labeled intensity region of interest and as EDC spectra bearing a prominent secondary electron peak. On the right side The secondary electrons are cut out, only the graphite intensities remain. The image is sliced into regions of 5 slides each, which are plotted as EDC spectra beneath.

From these figures, one can see that the intensity over the slides changes also a lot and has its maxima at the end of the slides. Also it appears difficult to find a single calibration procedure from these data. But in the following thesis we only integrated over central slides ($\pm$ 10 slides from the middle).

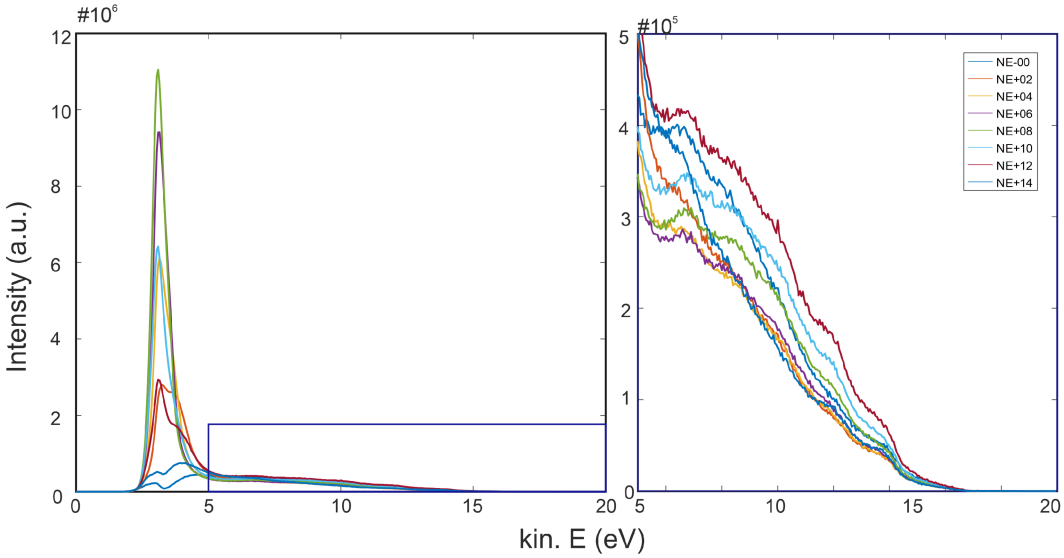

Figure 5.11.: $NE + 7°$ UPS spectrum distracted from the different takeoff angle measurements integrated over three slides

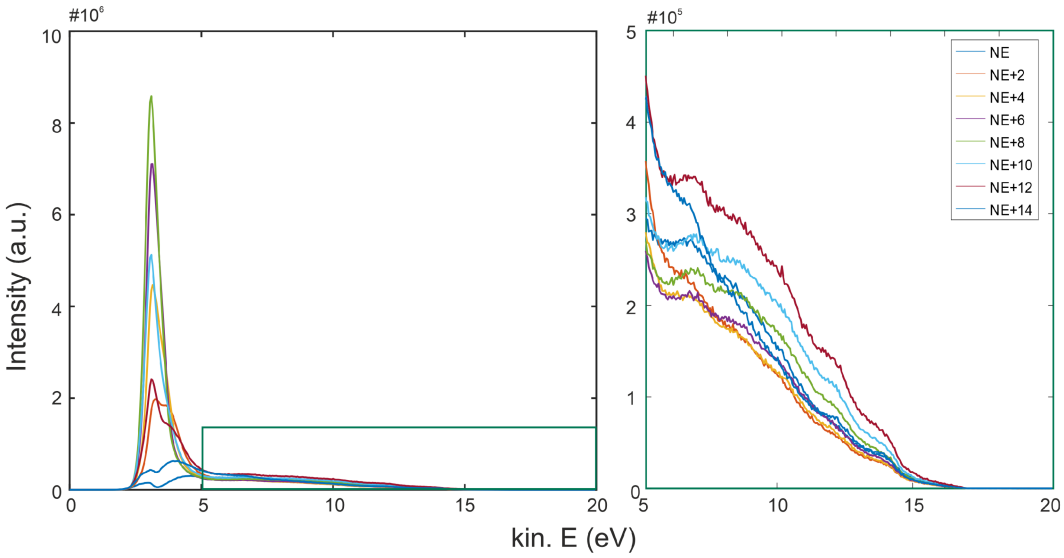

Figure 5.12.: $NE + 7°$ UPS spectrum distracted from the different takeoff angle measurements integrated over three slides with a.o.e normation.

As the detector has an acceptance of $\pm$ 8° it is possible to distract the same angle from different measurement. In figure 5.11 the angle$NE + 7°$ was chosen and been distracted from NE to $NE + 14°$ measurements. So for the NE we integrated over the lower end of the slides and so on up to the higher end for the $NE + 14°$ one. Figure 5.12 show the same take-off angle for different light spots and different spots on the detector. It also show the same result as the figures above for the different slides, the intensity of the spectrum is highest for the ones taken at the higher slides than for the middle ones ($NE + 8°$, green/ $NE + 6°$, violet).

To summarize there are many factors which needed to be taken in account for the calibration of an ARUPS measurement. As we pointed out in this chapter one is the area of the light spot, with the rotation of the sample also the polarisation of the incoming light changes, as well as the reflection and transmission of the sample and of course the detector itself. In this chapter we presented the first steps for the calibration of this measurements.

Find in the appendix further data analysis for other mesurement series from the tables 5.1 to 5.3

6. Conclusion and outlook

The contemplation of picene on 3 different metal fcc surfaces, Ag(100), Ag(110) and Cu(110) showed (delivered) no charge transfer.

6.1. Conclusion

6.1.1. Calibration

In this thesis a first step for a calibration routine of an ARUPS system with a Scienta SES 200 analyser was set.

A simple routine like gauging on the dark counts or the area of excitation is not sufficient, as the data in sec. 5.2 and sec. A reveals.

The differing sensitivity of the detector's channeltrons were identified in sec. 5.2, being an additional source of influence on the measured intensities.

Other factors like the changing of the lights polarisation under sample rotation and the transmission linked to reflectivity of the specific investigated surfaces have been considered, however, simple trigonometric functions seem not approbriate. Further investigations are left open for future studies.

6.1.2. Ag(110)

We investigated the electronic structure of picene on Ag(110) and we find the position of the HOMO, HOMO-1 as well as the HOMO-2 for a multilayer in agreement with the paper by Y. Wang et al., 2011. They further state a growth in multilayer islands which we can fortify by our surveillance of Stranki Krastanov growth mode at room temperature. For a multilayer at LNT conditions during preparation and measurement only HOMO, HOMO-1 and HOMO-2 emissions of the condensed phase emerge. After thawing as well as preparation under room temperature the HOMO and HOMO-1 of the monolayer are visible again in the multilayer island films. The frontier orbitals of the multilayer shifts for 0.4 eV to higher binding energies in comparison their monolayer positions.
No angular dependency was found for the molecular orbitals irrespective of coverages or changes in the polar and azimuthal orientation.
The appearing of molecular features in the NE geometry indicate a tilted molecule assembling which is in common with Y. Wang et al., 2011 proclaiming a standing-up orientation from the start based on RHEED (Reflection high-energy electron diffraction) and Q. Wang et al., 2017 stating a monolayer structure of one tilted beside one flat molecule due to LEED measurements. No charge transfer appeared.

6.1.3. Ag(100)

Our results on the electronic valence band structure agree with Huempfner et al., 2016 PES experiments for a monolayer Picene on Ag(100). A filling of the LUMO was not observed.
Furthermore, we established a Stranski Krastanov growth mode at room temperature in agreement with Kelly et al., 2016 is supported by our experiments showing monolayer emissions shining through the multilayer EDCs.

6.1.4. Cu(110)

We could identify the orbital positions for higher exposures. Again the growth mode is Stransky-Krastanov. For the monolayer the HOMO and HOMO-1 emissions of the EDC spectra being burried in the Cu 3d-band. These results agree with the work of Q. Wang et al., 2017 thefor a picene monolayer.

6.1.5. Cu-p(2x1)O

In contrary to the silver substrates, a monolayer coverage requires a significantly higher molecular dosage, as analysed in the work function evolution. This indicates a different alignment for the first picene layer on the ordered oxidised copper compared to the clean metal substrates. It is suggested that the substrate forced a tilted arrangement of the molecules along the Cu-O rows, whereas on the metal substrates the first olayer presumably adsorbs in planar geometry. The tilted adsorption leads to a higher density within a layer and therefore requires a higher exposure to complete one layer. Such an alignment has been observed for several chainlike molecules before (Koller, Berkebile, et al., 2007, Oehzelt et al., 2007). No charge transfer happened.
In the low coverage regime at half a monolayer it appears that the molecular orbitals are more pronounced at higher polar take off-angles, indicating a preferential alignement. The Fermi-edge and the Cu d-band are visible even at higher coverges suggesting a non completely coverage of the film, again compatible with Stranski Krastanov growth.

6.2. Outlook

6.2.1. Calibraion

For a general calibration routine the inclusion of further impact factors like the changing of the lights polarisation under sample rotation and the

transmission linked to reflectivity of the specific investigated surface have to be considered.

6.2.2. Picene on metal surfaces

In general an extension of the investigations on Ag(110), Ag(100), Cu(110) and Cu-p(2x1)O concerning coverages and measurement geometries are suggested.
Depending on the substrate, only one or three azimuthal adjustments are recorded and they are only in monolayer or even half-monolayer coverage. This is far not enough to make a statement concerning the orientational behaviour of Picene on those metal surfaces. Therefore most important a LEED has to be included in the experimental setup to predominantestablish the azimuthal directions of the substrate.
The dosing series should be extended in more different molecular layer thicknesses at low coverages to get a chance to discover maybe existing submonolayers and their orientations.
The change in configuration due to LNT is also a point worth looking at, even for thin films.
Additionally performed XPS measurements for all Picene layer thicknesses would lead to a better understanding of the temperature dependent coverage evolution.

Appendix A.

Appendix

A.1. Comparing EDC spectra of graphite raw data and the 2 normations in angular vs. spatial mode

A.1.1. HeI angular mode and spatial mode with pass energy 10 eV; $E_{kin} = 0 - 20$ eV

The following pictures present angular and spatial mode recordings side by side for the raw data and the normed one to the area of excitation as well as to the dark counts. Both adjustments share the same further parameters, like the HeI-discharge lamp with 21.22 eV, the pass energy of 10 eV and the kinetic energy range $E_{kin} = 0 - 20$ eV. Especially in the spatial mode the peaks at the localized states are predominant 5.1.3. Both modes shar the same binding energy of 13.65 eV for the secondary electron cutoff.

Appendix A. Appendix

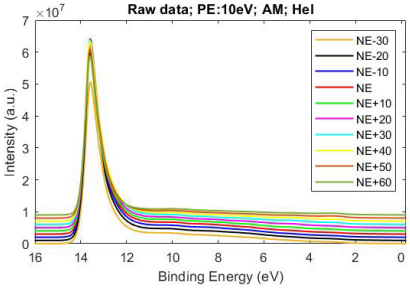

(a) Raw data, angular mode

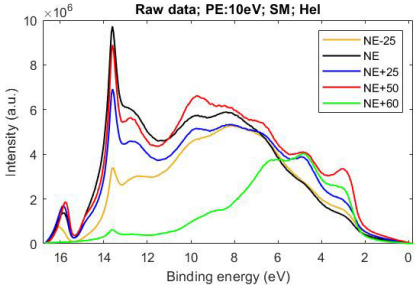

(b) Raw data, spatial mode

Figure A.1.: Graphite raw data HeI photoemission EDC spectra with pass energy 10 eV in two modes.

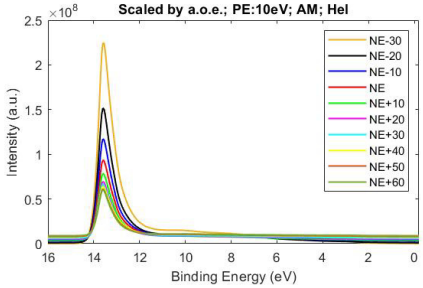

(a) Raw data normed to the area of excitation, angular mode.

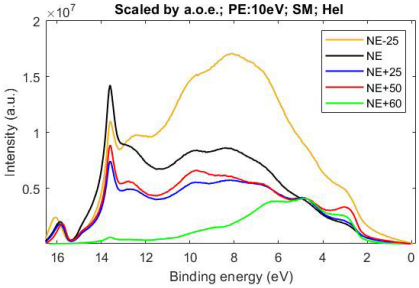

(b) Raw data normed to the area of excitation, spatial mode.

Figure A.2.: Graphite raw data normed to the area of excitation HeI photoemission EDC spectra with pass energy 10 eV in two modes.

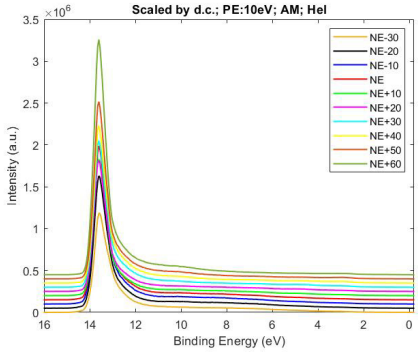

i

(a) Raw data normed to the dark counts, angular mode.

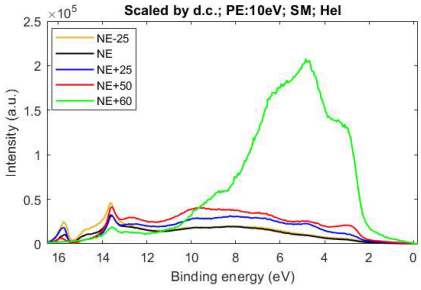

(b) Raw data normedd to the dark counts, spatial mode.

Figure A.3.: Graphite raw data normed to the dark counts HeI photoemission EDC spectra with pass energy 10 eV in two modes.

A.1.2. HeII angular mode and spatial mode with pass energy 20 eV

HeII with 40.82 eV as UPS light source changes the appearance especially of the angular mode, while the shape of the spatial mode nearly stays the same as with HeI. Both measurement series use a pass energy of 20 eV and an energy range of $E_{kin} = 25 - 40$ eV. This time only the localizes states at 2.95 ev and the one at 7.45 eV emerge as the only distinct peaks.

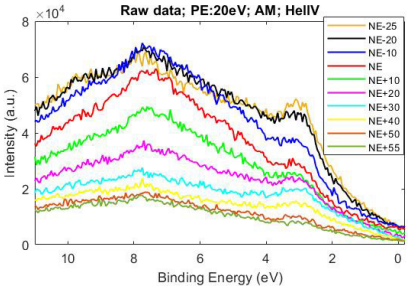

(a) Raw data, angular mode.

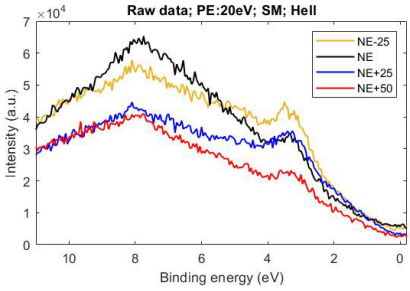

(b) Raw data, spatial mode.

Figure A.4.: Graphite raw data HeII photoemission EDC spectra with pass energy 20 eV in two modes.

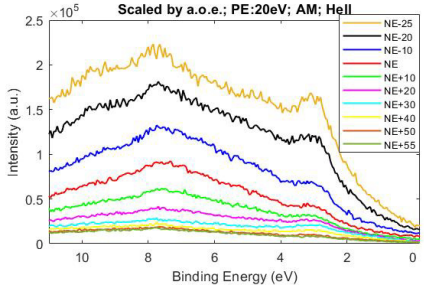

(a) Raw data normalized to the area of excitation, angular mode.

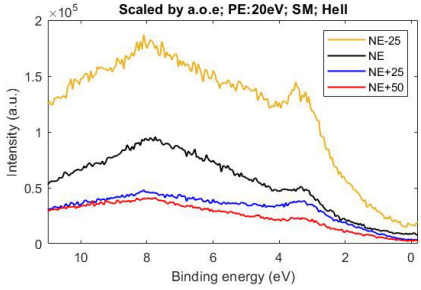

(b) Raw data normalized to the area of excitation, spatial mode.

Figure A.5.: Graphite raw data normed to the area of excitation HeII photoemission EDC spectra with pass energy 20 eV in two modes

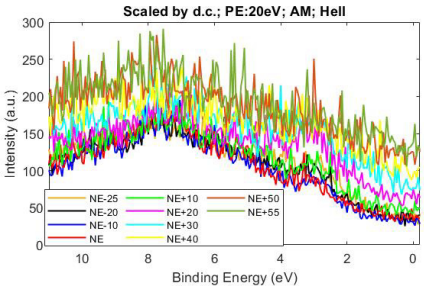

(a) Raw data normalized to the dark count, angular mode.

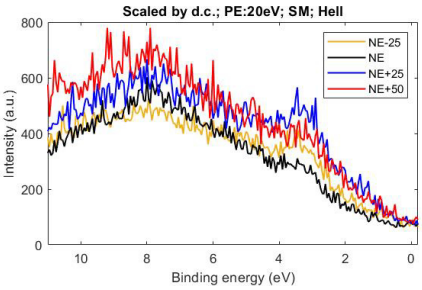

(b) Raw data normalized to the dark count, spatial mode.

Figure A.6.: Graphite raw data normed to the dark counts HeII photoemission EDC spectra with pass energy 20 eV in two modes.

A.1.3. XPS Mg k_α angular mode with PE 10 eV

The raw data and it' normalization to the area of excitation and the dark counts are plotted for XPS Mg k_α.

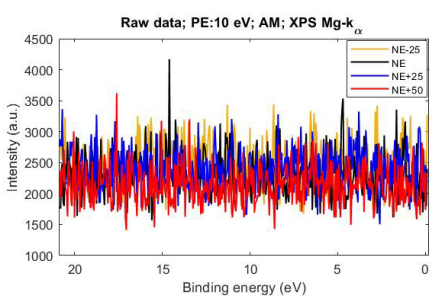

(a) Mg k_α XPS of the graphite raw data.

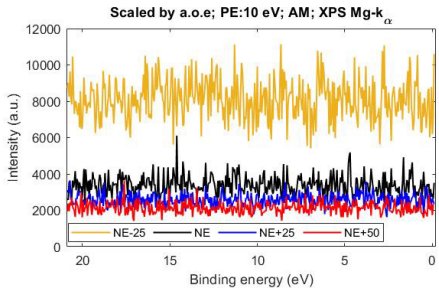

(b) Mg k_α XPS of the graphite raw data normalized to area of excitation.

Figure A.7.: Mg k_α XPS survey for graphite raw data and normed to the area of excitation with pass energy 10 eV.

A.1.4. Angular progress of intensity at chosen binding energies

We chose the measurement series HeI angular mode with pass energy 5 eV 5.2 to demonstrate the angular dependency of the intensity at distinct binding energies in the graphite raw data EDC spectra (fig. A.8. Therefore we chose the binding energies at 1.0 eV, 6.05 eV, 10.05 eV and the two secondary electron peaks at 15.0 eV and 16.65 eV in fig. A.9a to fig. A.10b. The angular versus intensity trend at those energies is plotted in fig. A.11a. In fig. A.11b a smoothing factor of the peaks particular $\sqrt{E_b}$ including the analyser transmission only flattens the curves, but has no major infect on their shapes. Due to the change of a round to a elliptical light cone on the sample with it's incident angle (sec. 5), a trend for the graph like a half ellipse is anticipated. This is not fulfilled neither for the angular nor the spatial mode.

Appendix A. Appendix

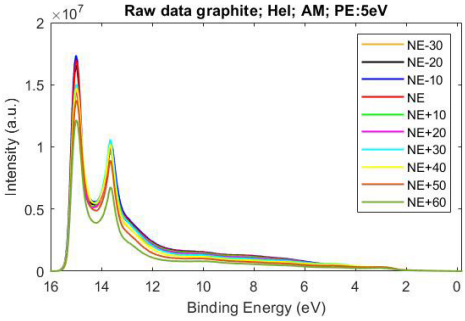

Figure A.8.: Raw data He I photoemission EDC in angular mode with pass energy 5 eV, recorded in a range of $E_{kin} = 0 - 20$ eV.

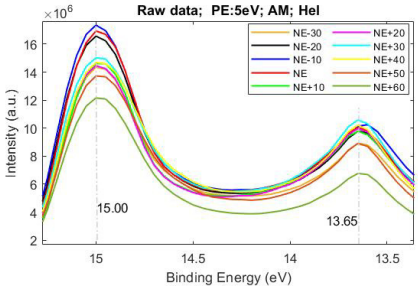

(a) The two secondary electron peaks of the graphite raw data.

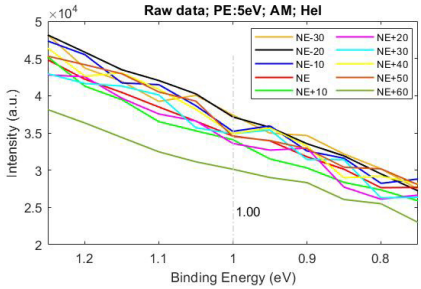

(b) Peak at $E_b = 1.00$ eV in the graphite raw data EDC spectra.

Figure A.9.: Graphite raw data HeI photoemission EDC spectra with pass energy 5 eV at the secondary electron cutoff and an additonal abitray chosen peak.

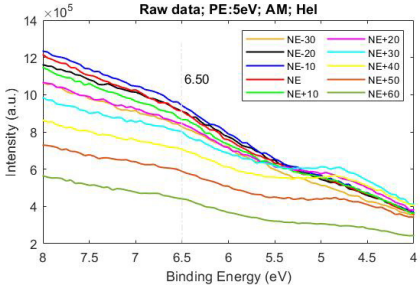

(a) Peak at $E_b = 6.50$ eV eV in the graphite raw data EDC spectra.

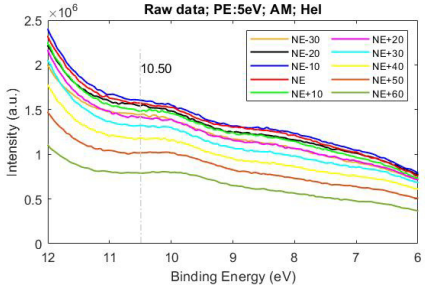

(b) Peak at $E_b = 10.50$ eV in the graphite raw data EDC spectra.

Figure A.10.: Graphite raw data normed to the dark counts HeII photoemission EDC spectra with pass energy 20 eV in two modes.

A.1. Comparing EDC spectra of graphite raw data and the 2 normations in angular vs. spatial mode

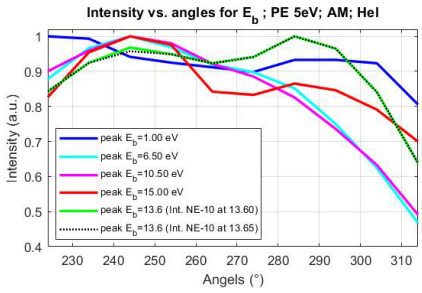

(a) Angular dependency of the intensity progress at the chosen binding energies.

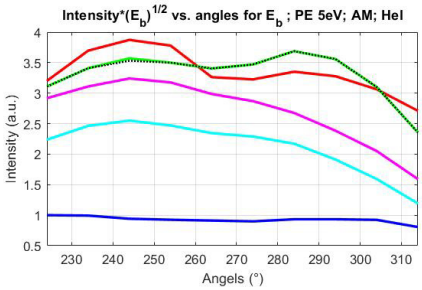

(b) Angular dependency of the intensity progress at the chosen binding energies. This time each intensity is additionally multiplied by the $\sqrt{E_b}$ of the related peak.

Figure A.11.: Angular depedency of the intensities at the chosen peaks in the EDC spectra above.

Bibliography

Elander, J. H. D. (1984). *Photoelectron spectroscopy - An introduction to ultraviolet photoelectron spectroscopy in the gas phase*. 2nd ed. Butterworth. ISBN: 0-408-71057-8 (cit. on p. 4).

Henzler, M., W. Göpel, and Ch. Ziegler (1994). *Oberflächenphysik des Festkörpers*. 2nd ed. B.G.Teubner (cit. on p. 4).

Hölzl, J. and F. K. Schulte (1979). "Work function of metals." In: *Springer Tracts in Modern Physics*. Vol. 85, p. 1. DOI: 10.1007/BFb0048919 (cit. on pp. 17, 36, 51, 58).

Huempfner, T. et al. (Nov. 2016). "Insight into the unit cell: Structure of picene thin films on Ag(100) revealed with complementary methods." In: *J.Chem.Phys.* 145.4 (cit. on pp. 25–29, 58, 96).

Hüfner, Stefan (2003). *Photoelectron Spectroscopy - Principles and Applications*. 3rd ed. Springer (cit. on pp. 4, 7, 10).

Kaner, B. R. and A. G. MacDiarmid (Feb. 1988). "Plastic that conduct electricity." In: *Scientific American* 258.2, pp. 106–111 (cit. on p. 1).

Kelly, S. J. et al. (2016). "Structural and electronic properties of ultrathin picene films on the Ag(100) surface." In: *Surface Science* 652, pp. 67–75 (cit. on pp. 20, 25, 26, 28, 58, 96).

Koller, G. (Jan. 2002). "Controlling the Organic-Inorganic Interface: Organic Molecules on Nanostructured Surfaces." PhD thesis. Institue for Experimental Physics, KFU Graz, Universitätsplatz 5, 8010 Graz, Austria; georg.koller@uni-graz.at (cit. on p. 77).

Koller, G., S. Berkebile, et al. (2007). "Intra- and Intermolecular Band Dispersion in an Organic Crystal." In: *Science.* 317 (5836), pp. 351–355. DOI: 10.1126/science.1143239 (cit. on pp. 67, 97).

Koller, G., R. I. R. Blyth, et al. (Feb. 2000). "Band alignment at the organic-inorganic interface." In: *Applied Physics Letters* 76.7 (cit. on p. 10).

Koller, G., P. Puschnig, et al. (2016). "Photoelekronen-tomographische Bilder von Molekülorbitalen - Elektronenorbitale in 3D." In: *Phys. Unserer Zeit* 47.4, pp. 192–198. DOI: 10.1002/piuz.201601442 (cit. on pp. 4, 9).

Liu, Y. et al. (June 2014). "Impact of molecular orbital distribution on photoelectron intensity for picene films." In: *Journal of Electron Spectroscopy and Related Phenomena* 195, pp. 287–292 (cit. on pp. 2, 21).

Oehzelt, M. et al. (2007). "The Molecular Orientation of para-Sexiphenyl on Cu(110) and Cu(110) p(2×1)O." In: *ChemPhysChem* 8.11, pp. 1707–1712. DOI: 10.1002/cphc.200700357. eprint: https://chemistry-europe.onlinelibrary.wiley.com/doi/pdf/10.1002/cphc.200700357. URL: https://chemistry-europe.onlinelibrary.wiley.com/doi/abs/10.1002/cphc.200700357 (cit. on pp. 67, 97).

Offenbacher, H. et al. (2016). "Photoelekronen-tomographische Bilder von Molekülorbitalen - Elektronenorbitale in 3D." In: *Phys. Unserer Zeit* 47.4, pp. 192–198. DOI: 10.1002/piuz.201601442 (cit. on p. 4).

Otero, R., A. L. Vázquez de Parga, and J. M. Gallego (Mar. 2017). "Electronic, structural and chemical effects o charge-transfer at organic/iorganic interfaces." In: *Surface Science Reports* 72, pp. 105–145 (cit. on p. 11).

Puschnig, P. et al. (2013). "The Structure of Molecular Orbitals Investigated by Angle-Resolved Photoemission. Fundamentals and Applications." In: *Small organic molecules on surfaces* -. Ed. by R. Hull et al. Vol. 173. Springer Series in Material Science. Springer. Chap. 1, pp. 3–23. DOI: 10.1007/978-3-642-33848-9_1 (cit. on pp. 3, 8).

Reinisch, E. M. (2015). "n-Doping of Conjugated Molecules on fcc Metal Surfaces: Investigations employing Photoemission Tomography." PhD thesis. Institue for Experimental Physics, KFU Graz, Universitätsplatz 5, 8010 Graz, Austria (cit. on p. 79).

Roth, F. et al. (Oct. 2010). "electronic properties of molecular solids: the peculiar case of picene." In: *New J. Phys.* 12 (103036). DOI: 10.1088/1367-2630/127107103036 (cit. on p. 20).

Schneuwly, A. et al. (Nov. 1998). "Bondability analysis of bond pads by thermoelectric temperature measurements." In: *Journal of Electronic Materials* 27, pp. 1254–1261. DOI: 10.1007/s11664-998-0079-2.

Standards, National Institute of and Technology (n.d.). *NIST Chemistry WebBook, SRD 69*. URL: https://webbook.nist.gov/cgi/cbook.cgi?ID=213-46-7 (cit. on p. 14).

Wang, Q. et al. (2017). "Picene thin films on metal surfaces: Impact of molecular shape on interfacial coupling." In: *Phys.Status Solidi RRL* 11.5. DOI: 10.1002/pssr.201700012 (cit. on pp. 25, 29, 31, 32, 50, 64, 96, 97).

Wang, Y. et al. (June 2011). "Effect of Oxygen on the Electronic Structure of Highly Crystalline Picene Films." In: *J. Am. Chem. Soc.* 133, pp. 10054–10057 (cit. on pp. 25, 29–31, 50, 96).

Zeppenfeld, P. et al. (Dec. 1997). "Adsorption and growth on nanostructured surfaces." In: *Applied Surface Science*, pp. 484–490.

Zhou, S. J., G. -H. Gweon, and A. Lanzara (Apr. 2006). "Low energy excitations in graphite: The role of dimensionality and lattice defects." In: *Annals of Physics* 321, pp. 1730–1746. DOI: 10.1016/j.aop.2006.04.011 (cit. on p. 81).